ELECTROCHEMICALLY-GROWN SINGLE NANOWIRE ARRAY FOR HIGHLY SENSITIVE AND SELECTIVE CHEMICAL DETECTION

by

Yushi Hu

B.S. in Microelectronics Engineering, Fudan University, China, 2006

M.S. in Electrical Engineering, University of Pittsburgh, 2008

Submitted to the Graduate Faculty of

the Swanson School of Engineering in partial fulfillment

of the requirements for the degree of

Doctor of Philosophy

University of Pittsburgh

2011

UNIVERSITY OF PITTSBURGH

SWANSON SCHOOL OF ENGINEERING

This dissertation was presented

by

Yushi Hu

It was defended on

June 7, 2011

and approved by

Dr. William Stanchina, Professor, Department of Electrical and Computer Engineering

Dr. Joel Falk, Professor, Department of Electrical and Computer Engineering

Dr. Kevin Chen, Associate Professor, Department of Electrical and Computer Engineering

Dr. Sung kwon Cho, Associate Professor, Department of Mechanical Engineering and
Material Science

Dr. Minhee Yun, Associate Professor, Department of Electrical and Computer Engineering

Dissertation Director: Dr. Minhee Yun, Department of Electrical and Computer Engineering

ELECTROCHEMICALLY GROWN SINGLE NANOWIRE ARRAY FOR HIGHLY SENSITIVE AND SELECTIVE CHEMICAL DETECTION

Yushi Hu, PhD

University of Pittsburgh, 2011

One dimensional nanostructures (nanowires) have emerged as important building blocks for micro/nano devices, such as chemical and biomolecular sensors, photovoltaic devices, nonvolatile memories, and nano power generators. In this work, the fabrication and characterization of single metal, conducting polymer and metal oxide nanowires will be discussed. These single nanowires were synthesized site-specifically inside Polymethyl methacrylate (PMMA) channels defined by electron beam lithography (EBL) via electrochemical deposition. The dimensions of these nanowires were predefined by optical lithography and EBL; the widths ranged from 100 nm to 50 nm, and the lengths were from 3 to 7 microns. A gate-assisted electrochemical deposition method that was able to effectively improve the nanowire growth will be discussed. The successful integration of four different single nanowires on a single chip will also be demonstrated.

The applications of these single nanowires will be presented. A highly sensitive hydrogen sensor with a fast response (<20 s) and an extremely low detection limit (2 ppm) was achieved using single Palladium (Pd) nanowire. The structure of the Pd nanowire was found to be closely related to the growth condition, and different sensing mechanisms were discovered for different nanowire structures.

An electronic nose was built on a single chip using a nanowire array consisting of four different single nanowires, including Pd, Polypyrrole (PPy), Polyaniline (PANI), and ZnO nanowires. The sensing performances of this electronic nose for four different target gases,

including carbon monoxide (CO), hydrogen (H_2), nitrogen dioxide (NO_2), and methanol (CH_3OH), were studied in detail. Principal Component Analysis (PCA) was employed to analyze the sensing signals, and each target gas was clearly identified. A blind test was conducted to verify the performance of this e-nose.

TABLE OF CONTENTS

LIST OF TABLES

LIST OF FIGURES

PREFACE

I would like to first thank my advisor, Dr. Minhee Yun, for his relentless support, tremendous patience, insightful advices, and, most importantly, for providing me with a challenging but fruitful five years. His thirst for innovations, enthusiasm for scientific advancements, dedication towards research, and eternal optimism deeply influenced and encouraged me. I am sincerely grateful to Dr. Yun on both professional and personal levels.

I also thank Professor William Stanchina, Professor Joel Falk, Professor Kevin Chen and Professor Sung kwon Cho for joining my committee and giving me significant advice for my dissertation. I further thank my fellow researchers, Dave Perello, Innam Lee, Jiyong Huang, David Sanchez, and Yiwen Xu, for their continuous kindness and help. Working with them during the past five years has been a pleasure and privilege that I will always remember.

Finally, I want to express my gratitude to my parents for encouraging me to come to the United States for an intensive education. I especially want to thank my wife, Ting, for giving me the most needed warmth and comfort during my hardest days.

1.0   INTRODUCTION

1.1   MOTIVATION

One dimensional structures, including nanowires, nanorods and nanotubes, are receiving an enormous amount of attention. The most appealing feature of these structures is the narrow electric path that enables easy tuning or on/off switching of the electrical conduction. This suggests that nanowires (NW) can be used as elemental building blocks for a wide range of electronic devices, including Field Effect Transistors (FET), nonvolatile memories, solar cells, electric generators, chemical/bio-molecular sensors, etc.[1]. Different materials, including metals (Au, Ag, Pd), conducting polymers (Polypyrrole, Polyaniline, poly(3,4-ethylenedioxythiophene)) and semiconductors (Si, ZnO, GaAs) have been successfully utilized to fabricate NW structures. Metallic NWs attract increasing attention because of their special value in studying electron transfer [2-3] and potential in fabricating high-performance devices, such as hydrogen gas sensors [4-5], biosensors [6] and thermocouples [7]. A memory device based on metallic NWs, which was recently reported, broadens metallic NW applications [8]. On the other hand, NWs made of conducting polymer (CP), such as polyaniline (PANI) and polypyrrole (PPy), are showing great potential for use in biosensors because of their unique electronic properties and natural affinity with biomolecules [9].

1

NWs are considered promising candidates for sensor application because they are potentially more sensitive than other materials such as bulk and thin films. The advantages of NWs include:

1)   Higher surface area to volume ratio

The surface area to volume ratio (SVR) is greatly increased when the structure decreases from three dimensions (3D) to 2D or 1D. Suppose we have a block structure with three dimensions a, b, and c respectively. The SVR of this structure can be expressed as:

$$SVR = \frac{2(ab + bc + ac)}{abc} = 2\left(\frac{1}{c} + \frac{1}{b} + \frac{1}{a}\right) \quad (1.1)$$

In a 3D structure (e.g. bulk materials) a, b and c are relatively large, which makes the SVR a relatively small value. In a 2D structure (e.g. thin films), however, one of the dimension values is small so that the sum of reciprocal items is large. A 1D structure (e.g. NWs) possesses the largest SVR since two of the three reciprocals in Equation 1.1 are large. The SVR is an important factor in sensing because most sensors are functioning based on surface changes due to physical absorption or chemical reaction. A higher SVR means that a larger portion of the structure is exposed to targets, and therefore surface changes can result in a larger overall impact.

2)   Small size

By definition, a NW is a solid, cylindrical wire with a diameter less than 100 nm. This small lateral size of NWs enables a dense positioning of parallel nano-sized devices, such as FETs and memories based on semiconducting NWs. Small device size is also critical in biomedical applications. Currently, in-vitro biomedical sensors for detection of bio-molecules, such as proteins and tumor cells, have been successfully demonstrated with the use of thin film materials [10]. The development of next generation biosensors would require a direct implantation of the device into human body or a specific organism to realize an in-vivo test in real time. A smaller

device not only facilitates easier implantation process, but also introduces less perturbation thus arousing less immunization reactions from human body. Compared with thin films, NW is advantageous due to its potential in further minimizing the device size because of its 1D structure.

From the sensing perspective, a smaller size could help increase sensitivity and shorten response time. For sensors based on conductance change due to the presence of external surface charge, Debye screen length is a key factor. Take semiconductor for example, this length determines how deep the structure can be depleted ("screened") or accumulated by the addition of surface charge. For a NW structure with a diameter less than 100 nm, Debye length becomes comparable to the size of the structure itself [11]. The addition of surface charge can result in a ch arge depletion (or accumulation) in a majority portion of the NW, producing a large conductance change. In other words, the sensitivity increases when the structure size decreases.

Response time of a sensor is usually defined as the time is the sensor takes to complete 90% of signal change. For a se nsor based on physical or chemical adsorption of targets, this time is highly dependent on how long the system takes to reach the adsorption/desorption equilibrium. For a NW, the time for targets to diffuse into the body of the structure is much lower when compared with bulk structure or thin films. This shortened diffusion time guarantees a faster interaction between targets and NW so that equilibrium can be reached in a shorter time. Thus the sensor response time can be reduced with NW implementation.

Despite its appealing features, the development of NW based devices has been hindered because of the lack of a r eliable, controllable and economical synthesis technique. The fabrication methods for metal/conducting polymer (CP) NW are the subject of intense research because of the wide range of potential applications for these NWs. A controlled fabrication of

well-aligned, uniform metal/CP/semiconducting single NW or NW arrays not only improves the scalability of NW based devices, but also furthers the development of industry friendly processes, such as the layer-by-layer fabrication method used in the semiconductor industry. Chemical vapor deposition, the most commonly utilized process in semiconducting NW (Si and GeAs) fabrication, is less attractive in either metal or polymer NW synthesis because of the high temperatures (over 300°C) involved. Many other processes have been proposed, including nano-imprint lithography (NIL) [12-13], dip-pen [14-15], shadow mask [16] and template-based electrochemical deposition [17]. NIL is capable of fabricating NW arrays with less than 100 nm diameters and comparatively good uniformity [13]. However, this technique requires a m old which could degrade after each use. The usage of a mold also brings in undesirable contamination. Moreover, the detachment of the NW arrays from the mold is very difficult. Although Dip-pen technology is favored for its unprecedented freedom of NW shape patterning, it is less appealing for mass production because of its wire-by-wire process. The shadow mask technique is able to fabricate metal (Au/Ag) NWs with a predefined shape, but its maximum length is quite limited (~ 3 microns) and it can only synthesize a number of materials.

The electrochemical deposition process is perhaps the most frequently used technique in fabricating metal/CP nanowires. The minimal equipment requirements, operation at ambient temperature, fast process and scalability make it e conomically and technically attractive. Moreover, this technique has seen great improvement in recent years and it is no longer limited to conducting materials. Reports on e lectrochemically deposited silicon and zinc oxide nanowires extend the application of electrochemical deposition to semiconductors [18-19]. Previous attempts at controlled growth through electrochemical deposition were primarily based on different templates, such as highly ordered pyrolytic graphite (HOPG), anodic aluminum

oxide (AAO) or stainless steel [20-22]. These techniques were refined to NW bundles or arrays, and the NW properties were heavily dependent on the properties of the templates. More importantly, NW device integration through these techniques was complicated by tedious post-processing such as NW selection, alignment, and electrode deposition. A method that could enable single NW synthesis, easy device integration and uniform growth, as well as effective growth control, is highly necessary for further development of NW based electronic/biomolecular devices.

Compared with NW bundles, single NWs have unique advantages. A device based on NW bundles relies on the overall performance of a collection of NWs, which severely undermines the one dimensionality a NW structure possesses. Furthermore, the performance degradation from one NW would impact the overall performance of the NW device. For example, the effectiveness of an FET device built on a semiconducting NW bundle would be greatly reduced even if only one of the NWs is metallic because of the alternative current path this failed NW would provide. Single NW devices, on the other hand, are based on the property of an individual NW and make use of the size advantage of the 1D structure. For instance, hydrogen gas sensors based on NW arrays [23] or bundles [24] have been presented by multiple groups. Other gas sensors based on conducting polymer nanowires and metal oxide nanowires have also been demonstrated [25-26]. These sensors not only present shorter response times, but they also provide better sensitivities compared with conventional non-FET sensors. As a result, single NW gas sensors are preferable because of their potential in providing higher sensitivity.

This work demonstrates a synthesis method capable of fabricating both single metal (Pd) and CP (PPy and PANI) NW with sub-50 nm diameters via electrochemical deposition. By employing an innovative two-step fabrication method, ZnO NW can also be obtained. A

hydrogen sensor with ultrahigh sensitivity and short response time based on single Pd NW is demonstrated, illustrating the effectiveness of using single nanowire as a sensor element. Also demonstrated is the integration of four single NWs (Pd, PANI, PPy and ZnO NWs) into an array on a same chip. This sensor array device was used for the detection of four target gases, including hydrogen (H_2), methyl alcohol (methanol), carbon monoxide (CO) and nitrogen dioxide (NO_2). Different NW materials were found to show different sensing behaviors toward these targets. In order to identify each target gas, sensing signals from the NW array were collected and processed using Principal Component Analysis (PCA). Specific signature area ("smell print") was found for each of the four gases on the 2D and 3D PCA plot. Lastly, a biomolecular sensor for detection of both proteins and biomarkers based on single aptamer entrapped PPy nanowire was demonstrated with a low detection limit and fast response.

1.2   DISSERTATION ORGANIZATION

Chapter 1 (this chapter) introduces the background of this work and outlines the frame and organization of this dissertation. While Chapter 2 also introduces the background information of this dissertation, it further presents the general properties and sensing mechanisms of each component NW. It addresses and covers the motivation of using principal component analysis (PCA) will be addressed and the fundamental knowledge of PCA will also be covered.

Chapter 3 describes the experimental details of this work, including the complete template fabrication process, the electrochemical deposition of the NW on a probe station, the sensor device preparation and integration into the gas sensing system, and finally the set-up of

the gas sensing control and data acquisition system. Chapter 4 deals with the results and data from experiments along with detailed analysis and discussion. This chapter has the following five parts: 1) the morphology, composition and electrical property of each NW; 2) discussion and analysis of improved NW growth via gate assisted electrochemical deposition; 3) a highly sensitive hydrogen sensor based on Pd single nanowires; 4) integration of nanowire sensor array; and 5) sensing performances, mechanisms and data analysis through principal component analysis. This chapter concludes with the results of this work and demonstrates the feasibility of an e-nose system based on the aforementioned single nanowire array synthesized via electrochemical deposition. Finally, chapter 5 summarizes the achievements and related publications of this work.

2.0   BACKGROUND

2.1   PALLADIUM NANOWIRE AND ITS SENSING BEHAVIORS

Palladium (Pd) is perhaps the most commonly used material in today's hydrogen-related applications (i.e. hydrogen sensors and hydrogen storage) due to its properties and unique interactions with hydrogen. In the field of nanotechnology, palladium thin films, mesowires and nanowires have been reported as effective hydrogen sensors or switches [23, 27]. In addition to its high sensitivity to hydrogen, Pd is chosen as one component in this work for its good selectivity. Only hydrogen, among all the target gases in this work, can considerably change its resistivity.

2.1.1   General Properties of Palladium

Palladium is a soft silver-white metal that resembles platinum. Along with platinum, rhodium, ruthenium, iridium, and osmium, palladium belongs to a group of elements referred to as the platinum group metals (PGMs). It is the least dense in PGMs and has the lowest melting point. Table 1 lists its basic properties. Among all the properties of Pd, the most appealing one is its ability to absorb hydrogen. Palladium can absorb hydrogen up to 900 times its own volume at

room temperatures; this property, unique to hydrogen, makes Pd the perfect material for both hydrogen sensing and hydrogen storage applications. The sensing properties of Pd are carefully studied in this dissertation.

2.1.2 Sensing mechanisms of Palladium

As mentioned above, Pd is well known for its high sensitivity to hydrogen. However, it is not very sensitive to most other gases. In this section, the physical and chemical interactions between Pd and hydrogen will be discussed. Different mechanisms are also included for other gases.

Table 1 General properties of Palladium

Name/Symbol/Number	Palladium/Pd/46
Group/Period/Block	10/5/d
Appearance	Silvery white metallic
Standard Atomic Weight	106.42 g·mol^{-1}
Phase	Solid
Density (Room Temperature)	12.023 g·cm^{-3}
Crystal Structure	Cubic face centered
Melting Point	1828.05 K
Boiling Point	3236 K
Electrical Resistivity	105.4 nΩ·m (20°C)

It is common knowledge that upon exposure to hydrogen, Pd will undergo a phase change that leads to a chemical and physical property change of its structure. Specifically, the chemical state of Pd switches from one hydride phase (alpha (α) phase) to another hydride phase (beta (β) phase) when hydrogen presents. At room temperature or higher temperatures, α phase Pd hydride has a very low atomic ratio of H/Pd (<0.1), while β phase Pd hydride has a much higher atomic ratio (H/Pd$\approx$0.7) [28]. These two phases can coexist in the same structure when the atomic ratio is in the middle range. It has been reported that the composition of Pd changes in accordance with the hydrogen partial pressure [28]. When the partial pressure of hydrogen increases, the atomic ratio of H/Pd increases accordingly. Under constant pressure and temperature, the higher hydrogen concentration in a gas mixture, the higher hydrogen partial pressure. Thus the phase of Pd hydrides formed is directly dependent on the actual concentration of hydrogen. With lower hydrogen concentration (or partial pressure) the hydride would be predominantly α phase, while β phase hydride would dominate with higher hydrogen concentration. It has also been found that the transition from α phase to β phase is reversible when the hydrogen concentration changes. A detailed study on the relationship between the Pd hydride composition and hydrogen pressure under different temperature suggests that based on this relationship the sensor working temperature can be selected [29].

In accordance with the transition of the Pd hydride from α phase to β phase, two detectable changes occur. First, a resistance increase occurs when the hydride shifts from α phase to β phase [30]. The resistance change could be as high as 1.8 times at room temperature when the Pd hydride transforms from α phase (H/Pd$\approx$0) to β phase (H/Pd$\approx$0.7). The second detectable change is a structural lattice change. As mentioned earlier, Pd has an FCC structure with a lattice parameter of 0.3890 nm (298K). Upon hydrogen absorption, the lattice undergoes an isotropic

expansion while keeping its FCC structure. In α phase (298 K), the lattice parameter of PdH_x is around 0.3894 nm, which reflects its small component ratio of H/Pd ($x \sim 0.015$). However, in β phase the lattice parameter of PdH_x is around 0.4025 nm where the component ratio H/Pd is much higher ($x \sim 0.7$) [23, 28]. The volume expansion resulted from α phase to β phase lattice change is around 10.4% [23, 28-29]. This 10.4% volume expansion could be a dominant effect when it comes to a nanosized structure. Different from the resistivity increase, the volume expansion could cause a reduced resistance of the nanowire, as reported by Penner *et al* [23]. These two coexisting yet competing effects form a basis of understanding the mechanism of Pd based hydrogen sensors.

Compared with the Pd-hydrogen interaction, the interaction between Pd and methyl alcohol (methanol, CH_3OH) has a very small impact on Pd itself. Pd particles have been reported as an effective catalyst for methanol decomposition at a relatively high temperature (over 400K). The methanol would undergo the following reaction on the surface of Pd [31].

$$CH_3OH \leftrightarrow CO + 2H_2 \tag{2.1}$$

As indicated in reaction 2.1, H_2 would be present as a product of the direct interaction between Pd and methanol. Although methanol itself does not change Pd properties, the H_2 produced in this process is able to change the resistance of Pd. However, this resistance change caused by generated H_2 is trivial compared to the results from direct exposure to H_2 gas because a very limited portion of methanol undergoes decomposition under room temperature [31].

Similar to methanol, NO_2 is mostly adsorbed onto the Pd surface and undergoes the following atomic dissociation:

$$NO_2 \leftrightarrow NO(a) + O(a) \tag{2.2}$$

In this reaction, "a" indicates atomic level. This dissociation process happens when the temperature is over 180K. NO_2 adsorption onto Pd is irreversible when the coverage of NO_2 is small and it becomes reversible when the coverage is large. The product NO can also be adsorbed onto the nanowire surface and result in further decomposition which produces N_2, O_2 and N_2O. This study shows that N_2O is not adsorbed onto Pd. The lack of direct reaction between Pd and NO_2 guarantees that Pd only undergoes minimal changes when exposed to NO_2 as it mainly functions as a catalyst for NO_2 decomposition.

Similar to NO_2, CO has little effect on Pd. Pd can act as a catalyst for CO oxidation, as reported in [32], with the presence of O_2. The following reaction occurs:

$$2CO + O_2 \leftrightarrow 2CO_2 \quad\quad\quad\quad (2.3)$$

The conversion rate of CO to CO_2 is found to be directly related to the concentration ratio of O_2/CO [32]. In our experiment pure N_2 is used as a carrier gas. Thus the concentration of O_2 is very small. Correspondingly, the oxidation of CO is minimal and the interaction between CO and Pd is negligible. As a result, no obvious change is expected when Pd is exposed to CO.

2.2   CONDUCTING POLYMER (POLYPYRROLE AND POLYANILINE) NANOWIRES AND THEIR SENSING BEHAVIORS

Conducting polymers, including polypyrrole (PPy), polyaniline (PANI), poly(3,4-ethylenedioxythiophene) (PEDOT), etc. have shown great potential in chemical and biomolecular sensing areas and are easily fabricated. The unique properties possessed by these materials include: high conductivity, high electron mobility, and good bio-affinity. Among this group, PPy and PANI are the most frequently used materials because of the ease of fabrication

via electro-polymerization, their ability to withstand a wide range of pH values, the ease of doping by incorporating various ions and molecules into the polymer matrix from aqueous solutions. More importantly, both PPy and PANI will undergo structural changes upon exposure to either oxidation or reduction agents. The structural changes due to reduction/oxidation (redox) will lead to changes of electrical conductivity, which makes PPy and PANI extremely suitable for application in conductometric sensors. In addition, PPy and PANI have natural affinity with biomolecules, due to the existence of amine groups ($-NH_2$ or $-NH-$) in the polymer chain. This feature enables easy immobilization of bio-receptors on the surface and presents a big advantage in both bio-molecular sensing and drug delivery.

2.2.1   General Properties of Pyrrole and Polypyrrole

A polypyrrole (PPy) is a chemical compound formed from a number of connected pyrrole ring structures. Polypyrrole can also be called pyrrole black or polypyrrole black due to its normal black color. The PPy, a derivative of polyacetylene,belongs to the rigid-rod polymer host family. The monomer (pyrrole) that forms the PPy is a heterocyclic aromatic organic compound, which has a five-membered ring with four carbon atoms and one nitrogen atom completing the ring. The chemical structures of pyrrole and polypyrrole are shown below:

Pyrrole   Polypyrrole
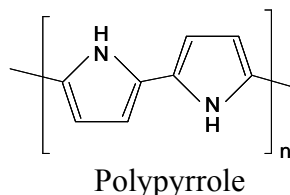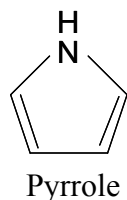
Pyrrole has a molecular weight of 67.09 g/mol, a density of 0.967 g/cm^3, a melting point of around -23°C and a boiling point of 129~131°C. Thus at room temperature pyrrole is in liquid

phase. PPy is either synthesized via a chemical method or an electrochemical method. Chemical synthesis, which usually involves mixing the monomer solution with a strong oxidizing agent (typically $FeCl_3$), is used when a l arge quantity of material is needed. On the other hand, electrochemical synthesis is preferred for the production of small quantities (e.g. scientific research). The electrochemical synthesis method enables a better control over material thickness, geometry and location, good film quality, and the ability to dope the material during synthesis process with a wide range of available dopants. The typical electro-polymerization process of monomers under the help of the anion Cl^- is illustrated by the following steps: [33]

Step 1: Single electron oxidation of monomer (pyrrole):
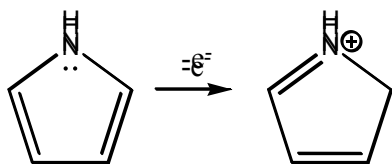
Step 2: Incorporation of counterion into monomer structure:
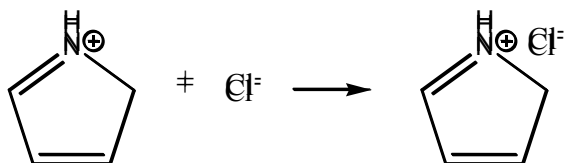
Step 3: Formation of a dimer:
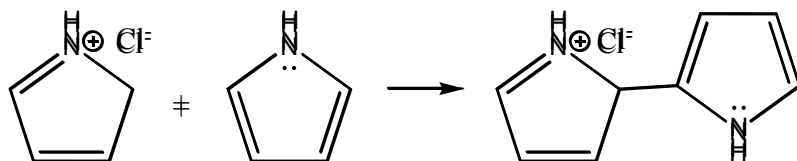
Step 4: Formation of long polymer:
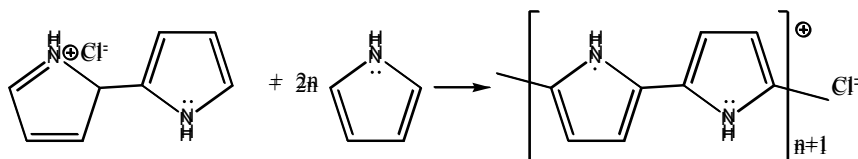
It is apparent that the polymer chain has incorporated a certain amount of positive charge (or H^+) which requires additional anions to balance and maintain the neutrality of the structure. In different oxidation states of polypyrrole, the number "n" can vary in a wide range with the most common cases being one anion (Cl^-) being shared by four rings. The conductivity of PPy stems from its ability to transfer electrons along the conjugated π-molecular orbital backbone. This charge transfer is closely linked to the motion of charge carriers in the material. In the above mentioned case, the number of the charge carrier (either H^+ or Cl^-) is critical for the current conduction along the backbone. The more charge carriers in polymer chains, the higher conductance the chain will possess. One thing to be noted is that the anion concentration is identical to that of H^+ because of its electrical neutrality. Final conductivity depends on several factors, including the charge transfer inside the individual polymer chain as well as the charge transfer between different polymer chains. Thus any change of the environment that could bring a change in charge carrier concentration in the polymer chain, such as a pH change in solution or the presence of oxidizing/reducing gas, will lead to a noticeable change in the polymer conductance. This conductance change upon reduction or oxidation is the underlying principle for many PPy based sensors.

2.2.2   General Properties of Aniline and Polyaniline

Polyaniline (PANI) is a conducting polymer that belongs to the semi-flexible rod polymer family. Although PANI was actually discovered over 150 years ago, it did not capture too much attention of the scientific community until 1980s when its high electrical conductivity was rediscovered. PANI is unique in the conducting polymers due to its easy synthesis, good environmental stability, and simple doping/dedoping chemistry. Although the fabrication

methods of producing PANI are quite simple, the polymerization mechanism and the exact nature of its oxidation are quite complex. Due to its rich chemistry, PANI has been one of the most studied conducting polymers during the past 50 years.

The chemical structures of aniline and polyaniline are shown below:
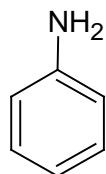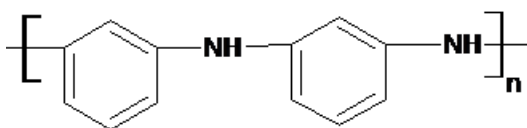
Aniline   Polyaniline

Aniline has a molecular weight of 93.13 g/mol, a density of 1.022 g/cm^3, a melting point of around -6.3°C and a boiling point of 184.13°C. Therefore, at room temperature aniline is in liquid phase. PANI is either synthesized via a chemical method or an electrochemical method. The polymerization of PANI is usually carried out in an acidic environment. A typical electrochemical polymerization process for PANI with the help of chloride ion can be shown in the following steps: [34]

Step 1:
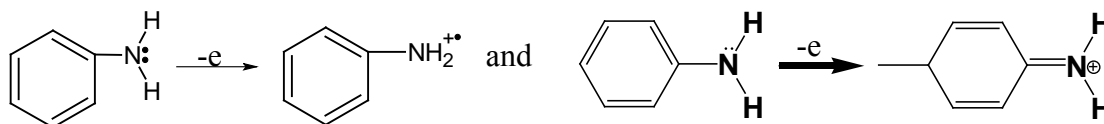
Step 2: Formation of Di-mer
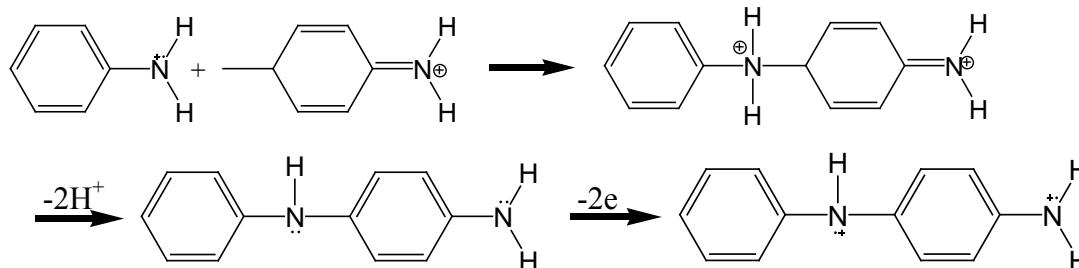
Step 3: Formation of Tri-mer:

16

$-2H^+$ →
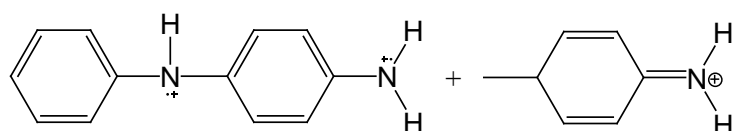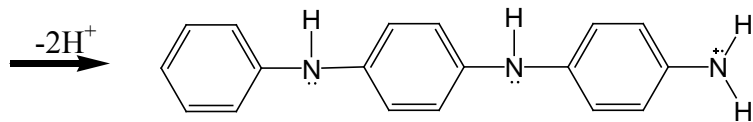
Step 4: Formation of longer polymer:

$-2H^+$
$-e$ →

Longer polymer
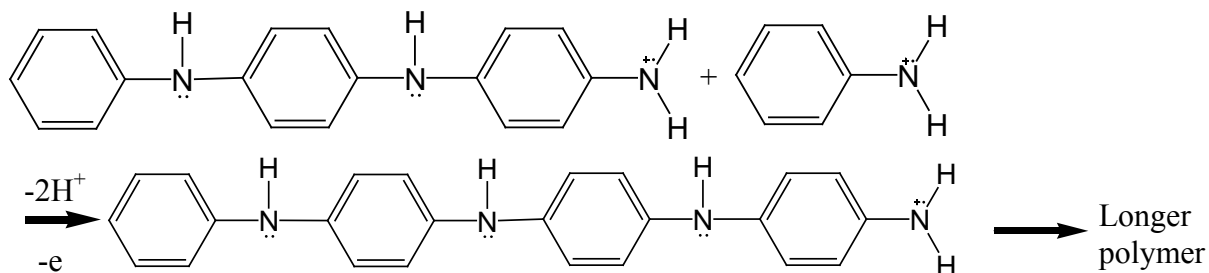
The oxidation states of PANI not only affect PANI's appearance but also directly affect its conductivity. The different states range from the fully reduced leucoemeraldine via protoemeraldine, emeraldine and nigraniline to the fully oxidized pernigraniline. The chemical structures of leucoemeraldine, emeraldine and pernigraniline PANI are illustrated in the following part: [35]
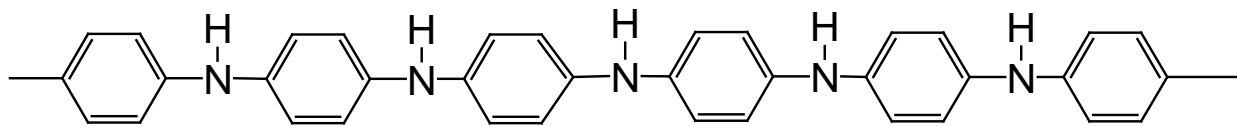
Leucoemeraldine (Fully reduced)
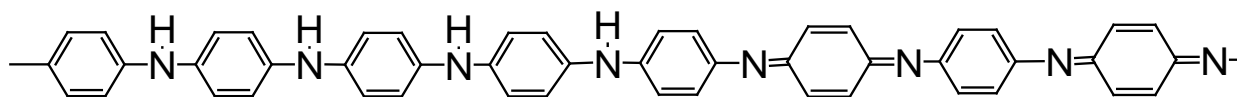
Emeraldine (Partially reduced/oxidized)
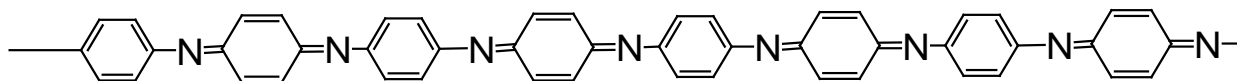
Pernigraniline (Fully oxidized)

Unlike in most other polyaromatics, the fully oxidized state in polyaniline is not conducting. Actually, none of the above mentioned states are conducting. PANI only becomes

conducting when protonation, which can generate charge carrier, happens in the partially oxidized states, such as the emeraldine base. This protonic acid doping process is very unique; no electrons have to be added to or removed from the insulating material to make it conducting. The different oxidation states of PANI can also be generated by doping with oxidants such as iodine, but the resulting conductivity is lower than that obtained via protonic acid doping. This is why we chose a protonic acid (hydrochloric acid or HCl) for electrochemical polymerization to obtain highly conductive PANI.

2.2.3 Sensing mechanisms of Polypyrrole and Polyaniline

The conductance of PPy and PANI depends on the concentration of charge carriers in the backbone structure, which can be changed by a number of environmental stimulations, including the addition of external redox agents or ionic solutions that contain H^+/OH^- ions. The chemical processes involving PPy and PANI can be generally divided to the following groups:[36]

1. Acid/base involved protonation/deprotonation of the polymer chains. This case is especially important for the PANI group, but also significant for PPy and its derivatives;

2. Oxidation/reduction by some redox components present in the surrounding medium, primarily oxidative species such as oxygen or other metal ions (Fe^{3+});

3. Interaction with solution components such as nucleophilic agents (e.g., OH^- ions, H_2O molecules) which could lead to polymer degradation;

4. Complexation or incorporation of metal ions from the medium (ionic solution for example) through the bonding effect generated by certain groups or ligands that present in the polymer structure;

5. Incorporation of components from the medium into the polymer structure due to ion exchange or adsorption (absorption). In the ion exchange case, certain types of spontaneous replacement occur between the doping ions in the polymer structure and ions from the solution. This results in the release of doping ions (such as Cl^-) from the polymer into the solution and the incorporation of the solution ions into the polymer. This is the working principle for PPy and PANI based biomedical drug delivery. On the other hand, adsorption refers to the incorporation of surfactant molecules or ions that are accumulated on the polymer surface. Under certain circumstances the above processes can happen in parallel when the surfactant anions spontaneously replace the doping ions.

Among the above five reactions, cases 1, 2, 3 and 4 are most important for liquid-based sensing applications, such as biomedical sensing and pH sensing. For gas sensing which happens mostly in a dry environment, case 1 and case 2 play important roles. Case 1 happens when target gases are highly acidic or basic, such as HCl and NH_3. Case 3 occurs when strong reducing gases such as H_2 or strong oxidizing gases such as NO_2 exist. Since PPy and PANI are considered p-type with holes as the majority charge carrier, strong reducing gases act as electron donors and reduce the carrier concentration in conducting polymer backbone. Strong oxidizing gases, on the other hand, act as electron extractors that increase the carrier concentrations on the backbone. Case 5 is extremely important in drug delivery applications. In addition to the five cases described above, molecule adsorption into polymer structure can also happen when the gas molecule has a relatively small size (for example, H_2, CO and small VOCs). These small molecules can penetrate into the polymer body or near the polymer surface at high concentrations and change the polymer conductivity.

2.3 ZINC OXIDE NANOWIRE AND ITS SENSING BEHAVIORS

2.3.1 General Properties of Zinc Oxide

Zinc oxide is an inorganic compound with a molecular formula of ZnO. It has a white solid powder appearance, and it is almost insoluble in water. Conventionally, ZnO powder is widely used as an additive into a variety of materials, such as plastics, glass, cement, lubricants, tire rubbers, etc. Most commercially available ZnO is produced synthetically. ZnO has a relatively large direct band gap of around 3.3 eV at room temperature, which brings it many advantages, including higher breakdown voltages, the ability to sustain large electric fields, lower electronic noise, and high-temperature and high-power operation. Table 2 shows a list of general properties of ZnO.

2.3.2 Synthesis of Zinc Oxide Nanostructure

Zinc oxide can be obtained through many different methods. Industrial synthesis of ZnO can be divided into two categories, indirect process and direct process. Indirect process refers to the process which oxidizes metallic zinc into ZnO. In this process, metallic Zn is first melted in a graphite crucible which is then heated to above 907 °C. At this temperature, Zn is vaporized and zinc vapor instantaneously reacts with the oxygen in the air to give ZnO. The products of this reaction are usually ZnO particles with an average size of 0.1 to a few micrometers. The ZnO particles are then transported into a cooling duct and collected in a bag house. By weight, most of ZnO in the world is manufactured in this way. Direct process, on the other hand, utilizes source materials from contaminated zinc composites such as zinc ore or smelter by-products.

Table 2 General properties of Zinc Oxide

Name/Symbol	Zinc Oxide/ZnO
Appearance	White Solid
Molecular Mass	81.41 g·mol^{-1}
Odor	Odorless
Density (Room Temperature)	5.606 g·cm^{-3}
Crystal Structure	Wurtzite/Zincblend/Rocksalt
Melting Point	2248 K
Boiling Point	2633 K
Bandgap	3.3 eV (direct)
Refractive index (n_D)	2.004

These materials are then reduced by carbon additives to produce zinc vapor, which is later oxidized into ZnO, as described in indirect process. The ZnO product manufactured in this way is low in purity and quality due to the low purity of source materials. In scientific research, high quality ZnO (especially nanostructured ZnO) is usually obtained through a vapor phase or liquid

phase chemical process. Three most common synthesis methods are used: chemical vapor deposition (CVD), hydrothermal process, and electrochemical deposition.

Chemical vapor deposition has been widely used to fabricate nanostructures, especially nanowires, made of semiconductor or metal oxide materials, such as Si, SiO_2, SnO_2, V_2O_5, etc. ZnO nanostructures can usually be grown with the help of certain catalysts, such as Au and NiO, via the vapor-liquid-solid (VLS) method. However, most recent research reports demonstrated catalyst-free growth of ZnO nanostructures with a relatively low temperature (~500°C) on different substrates, such as sapphire [37] and fused silica [38]. The precursors for ZnO growth are usually zinc acetylacetonate hydrate $[Zn(C_5H_7O_2)_2 \cdot xH_2O]$ or diethyl zinc (DEZn) $[Zn(C_2H_5)_2]$ with oxygen gas and nitrogen gas as carrier gases. The advantage of using CVD or MOCVD in ZnO growth is the high crystalline quality of the structure, which can be extremely important to applications such as solar cells in which optical or electrical properties of ZnO are critical. The disadvantage of using CVD is its high growth temperature that could greatly reduce the thermal budget for device integration and limit the range of application.

Liquid phase chemical process has natural advantages of low temperature growth and low instrument requirement over the CVD process. Electrochemical deposition can be done in temperatures from room temperature to elevated temperature (70°C), while most hydrothermal processes are done in aqueous solution at a temperature ranging from less than 100°C to 200°C. This advantage in lower growth temperature gives a lot more possibilities in fabricating different devices, such as flexible devices on plastic substrates that usually have low melting points.

Electrochemical deposition is usually done with electrolyte solutions containing zinc nitrate $[Zn(OH)_2 \cdot 6H_2O]$ and hexamethylenetetramine (HTMA) $[C_6H_{12}N_4]$ [39]. Previous reports demonstrated the growth of aligned ZnO nanorods and nanowires via the usage of templates

made of anodic alumina oxide (AAO) [40]. A template-free process has also been reported in fabricating ZnO nanostructures [39]. DC mode electrochemical deposition is usually used and the reaction normally happens at elevated temperatures realized via water bath.

Hydrothermal process for synthesizing ZnO nanostructures is usually done at a higher temperature than electrochemical deposition. This process relies on the thermal decomposition of zinc nitrate and precipitation of $Zn(OH)_2$, which finally gives ZnO, at higher temperatures. The basic solution used for hydrothermal process usually contains zinc nitrate and alkali, such as NaOH. By adding certain surfactants such as ethylenediamine (EDA) $[C_2H_4(NH_2)_2]$, the structure of grown ZnO can be carefully tuned. For example, EDA is believed to act as adsorbing (chelating) ligands to the Zn^{2+} cations (primarily on the six prismatic side planes), inhibiting the radial enlargement of the rods and generating ZnO nanorods with small diameter and high aspect ratio [41]. Although a seed layer is not necessary during hydrothermal growth of ZnO nanostructure, the aligned growth of ZnO nanowires or nanorods usually involves a selective patterning of a ZnO seed layer on which the ZnO nanorods are subsequently grown [42-43]. The hydrothermal growth temperature can be controlled under 100°C so that the growth process does not involve high temperature process required by the CVD process.

2.3.3 Sensing mechanism of Zinc Oxide

ZnO, especially in the form of thin film, nanorod and nanowire, is widely used as sensor element, due to its broad range of sensible targets, such as CO, NO_2, H_2, NH_3, HCl, and Volatile Organic Compounds (VOCs) [44]. Since most hydrothermally grown ZnO is believed to be n-type semiconductor under ambient condition, the commonly accepted sensing mechanism for ZnO related gas sensing is the charge accumulation and depletion on the surface of n-type ZnO

due to electron trapping on adsorbed oxygen species [25, 44]. The as-grown ZnO nanostructure is rich in ionizable oxygen vacancies: V_O, and/or ionized O^- species, which renders ZnO an n-type semiconductor: [25]

$$O_{(s)}^{2-} \rightarrow \tfrac{1}{2} O_{2(g)} + V_o; \qquad V_o \rightarrow V_o^+ + e^-;$$

$$V_o^+ \rightarrow V_o^{++} + e^-; \qquad O_{(s)}^- \rightarrow \tfrac{1}{2} O_{2(g)} + e^-;$$
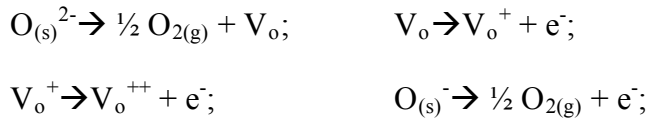
Exposure of ZnO to reducing gases, such as H_2 and CO, results in an increase of electron concentration on the ZnO surface, consequently an increase of conductance. On the other hand, the introduction of oxidizing gases, such as NO_2 and O_2, results in a decrease of electron concentration and conductance of the ZnO surface. Possible reactions related to the increase and decrease of the electron concentration when CO and NO_2 are introduced are shown below:

$CO + O_{(s)}^- \rightarrow CO_{2(g)} + e^-$: increase electron concentration; and

$NO_2 + e^- \rightarrow NO + O_{(s)}^-$: decrease electron concentration;
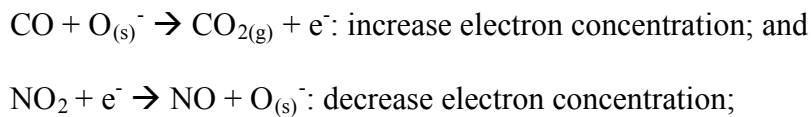
In a word, the conductance change of ZnO is directly related to the concentration of charge carrier density on ZnO surface (in this case the charge carrier is electron). Any oxidation (reduction) gas that can generate (consume) oxygen species on ZnO surface can decrease (increase) the electron concentration, thus decreasing (increasing) the ZnO conductance.

2.4 NANOWIRE SENSOR ARRAY AND PRINCIPLE COMPONENT ANALYSIS

2.4.1 Why a Sensor Array?

Individual sensors refer to those devices that are sensitive to certain kind of targets, such as combustive gases, poisonous gases, specific ions, bio-molecules, or humidity (water vapor).

Upon exposure to these targets, the devices can generate a signal, e.g. electrical/optical signal, which could be detected and collected by data acquisition units. Ideally, sensors are expected to uniquely and specifically respond to one kind of analyte with high selectivity. For example, palladium nanowire sensors respond to hydrogen gas and show minimal response to other gases. However, in real situations many constraints would dramatically undermine the applications of such "lock-key" sensors. First of all, the material on which a sensor is built can be sensitive to multiple analytes. The existence of different analytes makes it impossible for the sensor to tell which analyte causes the signal. Second, different materials from a closely related group, such as volatile organic compounds, have very similar properties. It is extremely hard to find a material that specifically responds to only one target. Lastly, the future development of sensor devices is no longer limited to the detectection of one specific target at a time, but instead requires a real time monitoring of various targets. For instance, dairy, wine, and tobacco industries need sensors to detect multiple organic elements from their products to determine the product's quality. In spacecrafts, a timely monitoring of gas composition is critical for both safety of the spaceship and the health of the astronauts. As a result, sensors based on one single material have great difficulty satisfying the sensing requirements of multiple targets. A sensor unit composed of more than one element is necessary to realize multi-target sensing with high sensitivity and selectivity.

2.4.2 Mechanisms of Single-Element Sensor and Multiple-Element Sensor

A conductometric sensor is one that presents a conductance/resistance change when exposed to specific sensing targets. As mentioned above, all the materials including Pd, PPy, PANI and ZnO experience conductance change in the presence of H_2, CH_3OH, CO and NO_2, even though each

exhibits a different behavior. In order to normalize the signal for different sensors, a fractional difference of resistance $\Delta R/R$ is commonly used. For a single element sensor A, the electrical signal $(\Delta R/R)_A$ resulting from exposure to a particular concentration of target gas represents the relative response (RS) of A to this gas at that concentration. For this single element sensor we expect the ratio $(\Delta R/R)_A$ to be large enough so that a) it should be able to rule out interruptions from external noise and b) it should achieve a low detection limit. However, this sensing mechanism is greatly undermined if the selectivity of A is not good enough. Suppose that there are three different gases (x, y, z) with three different concentrations including 200ppm, 400ppm and 1000ppm. Gas z is the target gas for sensor A while x, y are gases that could also result in conductance change in A. Assume the sensing behavior of this sensor can be presented by a randomly picked sensing data shown in Figure 2.1(a). It is clear that at any given concentration sensor A has the largest response signal toward gas z, confirming that gas z is the intentional target. However, gas x and gas y also produce nontrivial responses in A, which makes it difficult to differentiate gas z from gas x and gas y. As shown in Figure 2.1(b), the sensing responses from the three gases overlap due to the poor selectivity of sensor A. For example, 200 ppm of gas z has a similar sensing signal with 400 ppm of gas y and 1000 ppm of gas x. Thus it would be impossible to identify gas z by merely inspecting the sensing signal from sensor A.

Under this situation, two options are available to eliminate overlapping. First, change the sensor element A with another sensor element that has absolutely no overlapping sensing properties toward these three targets. However, this can prove difficult, especially when the targets are chemically similar to each other. Second, this problem can also be tackled by introducing more sensor elements or, in other words, by building a sensor array which contains more than one sensor element.

Suppose that a sensor element B with a sensing behavior different from that of element A is incorporated in the sensor array. Figure 2.2(a) show element B's sensing properties. Similar to sensor A, sensor B also has an overlapped sensing performance and cannot discriminate these three targets alone. Now we can construct a 2D sensing plot based on sensing signals from both elements, e.g. x axis for sensor A and y axis for sensor B. The magnitude represents the saturated RS value during each gas detection. The combined sensing plot is shown in Figure 2.2(b). It is clearly seen that, even though neither sensor A nor sensor B can differentiate gas z from gas x or gas y along, the combined sensing signals from sensor A and B can effectively discriminate gas x, y and z.

2.4.3   Principal Component Analysis

Although sensors A and B mentioned above are able to discriminate between three gases x, y and z based on a 2D sensing plot, this case is over-simplified. First, this case only has three gases in this case; in reality, many more targets exist. Second, the targets in this case are remotely different so that two sensors are sufficient to differentiate them. In real application, however, targets are often similar to each other (such as different VOCs), making it extremely difficult to effectively discriminate among them by using two elements. As a result, a sensor array with 3 or even more elements is required to realize multi-target sensing. For a three element sensor array, we could construct a 3D sensing space in which the RS value from each sensor element represents one axis. However, this formation of sensing plots/spaces by simply combining data sets from different sensing element has several limitations: 1) if more than 3 sensor elements are included in the array, a maximum of three dimensions can be displayed in the plot and up to three components can be chosen to contribute to the plot. Consequently, the information from
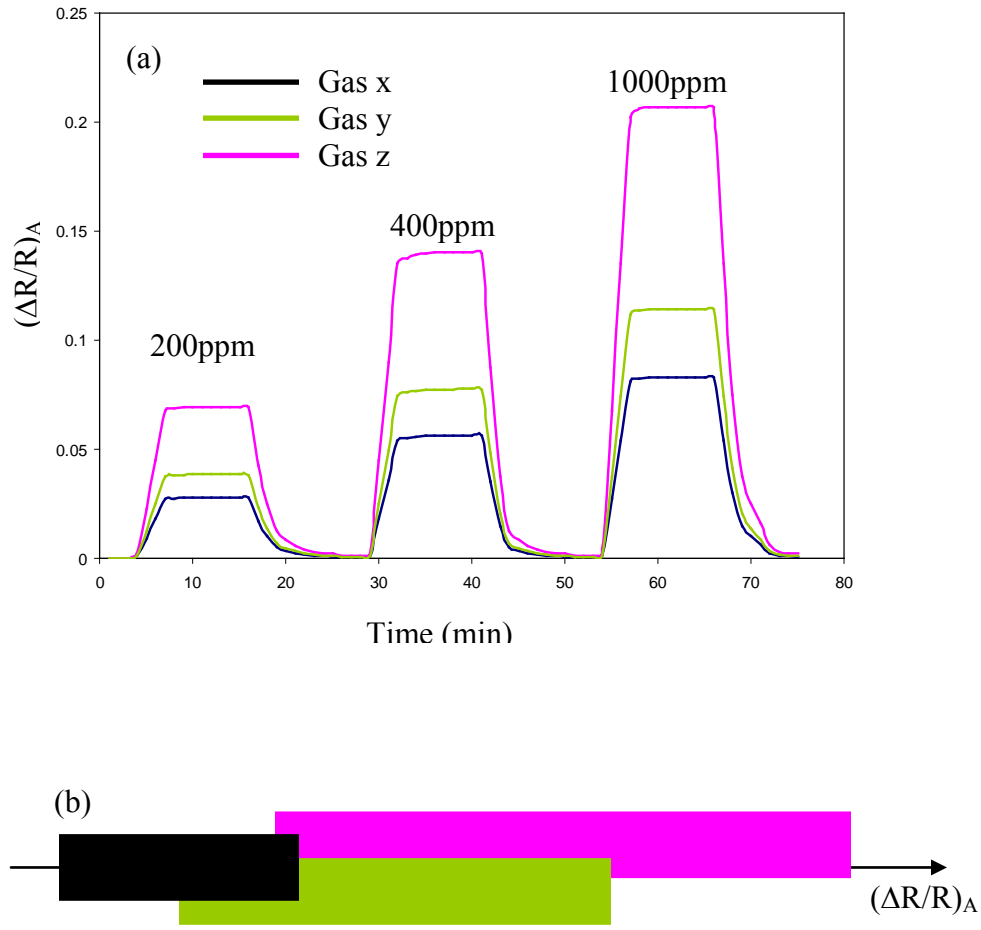
Figure 2.1 (a) A sample sensing signal for sensor A towards three different gases x, y and z. (b) The sensing responses for three gases in a one-dimensional manner.

28

the rest of the elements has to be abandoned. The advantage of adding more than three elements is thus greatly undermined; 2) The three dimensional plot formed simply by selecting three signal sets and arranging them in an orthogonal manner might not be able to effectively demonstrate the variance among the sensor signal sets, due to the possible chemical similarity or correlation among the elements.

As a result, a data processing method is needed to simplify the data sets, remove the redundant information among similar elements, and shrink the data sets obtained from all the sensor elements into a three dimensional data set without losing a great deal of information. If we were able to choose the 2 most significant data sets, then we could also construct a 2D sensing plot to represent the sensor array behavior to a maximum extent. This is why Principle Component Analysis (PCA) was introduced.

PCA has been widely used in electronic nose applications [45]. It is a way of identifying the relationships between data sets, and expressing the data so as to highlight their differences. PCA offers an effective tool to compress the data by reducing the number of dimensions and eliminating the redundant information without losing much information. It is especially powerful for dealing with high dimensional (dimension>3) data when direct visualization is impossible. The basic transformation steps for PCA are described as follows:

1) Extract all the RS data from all the sensor elements toward every target gas. The RS values extracted are the saturated values during each target injection. The data sets form a matrix so that data from each sensor element (a, b, c, d, …) represent a column and each gas injection (1, 2, 3, etc. represents different target gases at different concentrations) forms a row:

(a)

$(\Delta R/R)_B$

(b)

B

Gas x
Gas y
Gas z

A
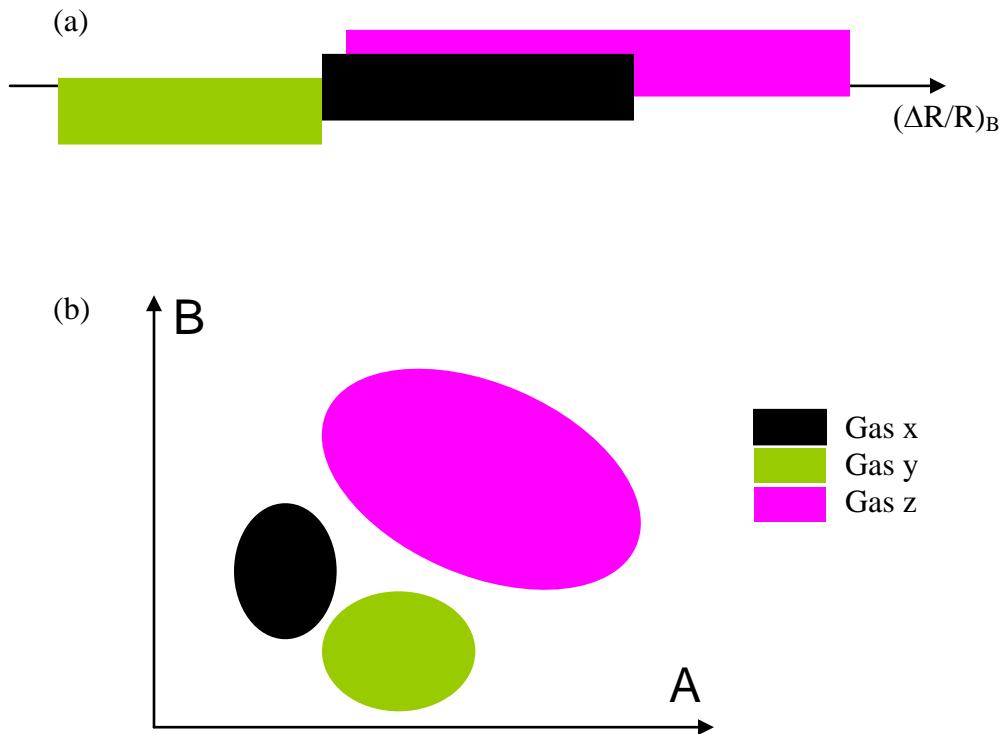
Figure 2.2 (a) A sample sensing signal for sensor B towards three different gases x, y and z. (b) The combined sensing responses for three gases from sensors A and B in a two-dimensional manner.

$$
\begin{bmatrix}
a_1 & b_1 & c_1 & \dots \\
a_2 & b_2 & c_2 & \\
a_3 & b_3 & c_3 & \\
a_4 & b_4 & c_4 & \\
\dots & \dots & \dots & \dots
\end{bmatrix}
\qquad
(1, 2, \dots m) : \text{different gas injections; } (a, b, c \dots): \text{sensor elements.}
$$

2) The original data sets with n dimensions are converted to mean-adjusted data sets so that the mean values of each data set from the original matrix will not affect the accuracy of the PCA process:

$$\begin{bmatrix} a_1 & b_1 & c_1 & ... \\ a_2 & b_2 & c_2 & \\ a_3 & b_3 & c_3 & \\ a_4 & b_4 & c_4 & \\ ... & ... & ... & ... \end{bmatrix} - \begin{bmatrix} \bar{a} & \bar{b} & \bar{c} & ... \\ \bar{a} & \bar{b} & \bar{c} & \\ \bar{a} & \bar{b} & \bar{c} & \\ \bar{a} & \bar{b} & \bar{c} & \\ ... & ... & ... & ... \end{bmatrix} = \begin{bmatrix} a_1^{'} & b_1^{'} & c_1^{'} & ... \\ a_2^{'} & b_2^{'} & c_2^{'} & \\ a_3^{'} & b_3^{'} & c_3^{'} & \\ a_4^{'} & b_4^{'} & c_4^{'} & \\ ... & ... & ... & ... \end{bmatrix} = A \text{ , where a, b, c ... r epresent}$$

different data sets from different sensor elements and a_1, b_1, c_1 represent the RS value extracted from different sensor during a gas injection event (i.e. a injection of certain target gas at certain gas concentration). If there are four nanowire sensors, for example, then the number of columns n will be 4. If there are four target gases and each is tested under four different concentrations, there will be m = 4×4 =16 rows in total. $\bar{a}$, $\bar{b}$, $\bar{c}$ represents the mean value of each column. The reason for using the mean-subtracted data sets instead of the original data set is to remove the effect from the mean value of each column. Otherwise, the first principal component will be heavily biased by t he mean value of each column and results in an inaccurate demonstration of the data.

3) A covariance matrix with a dimension of n i s constructed for the mean-adjusted data matrix A:

$$cov(A) = \begin{bmatrix} cov_{aa} & cov_{ab} & cov_{ac} & ... \\ cov_{ba} & cov_{bb} & cov_{bc} & ... \\ cov_{ca} & cov_{cb} & cov_{cc} & ... \\ ... & ... & ... & ... \end{bmatrix} \qquad \text{(n} \times \text{n matrix)}$$

4) The eigenvalues and eigenvectors are then found for matrix cov(A):

$Eigenvalues = [\lambda_1, \lambda_2, \lambda_3, ... \lambda_n]$, and $Eigenvectors = \{q_1, q_2, q_3, ... q_n\}$.

5) Sort the eigenvalues from largest to smallest in terms of the absolute value, and then select the first few eigenvectors corresponding to the largest eigenvalues as the principal components. The matrix containing the eigenvectors is called a feature vector:

Featurevector $= \{q_n, q_m, q_l, ...\}$. The purpose of this process is to find out the most significant PCs. The number of the PCs chosen decides the dimension of the PCA plot.

6) The final transformed data are then obtained by multiplying the transposed feature vector and the transposed mean-adjusted data sets. These data are usually called the *scores*. The dimension of these data sets equals the number of the eigenvectors (n) in the feature vector matrix.

$$
\text{Final data sets: } B = \{q_n, q_m, q_l, ...\}^T \times
\begin{bmatrix}
a_1' & b_1' & c_1' & ... \\
a_2' & b_2' & c_2' & \\
a_3' & b_3' & c_3' & \\
a_4' & b_4' & c_4' & \\
... & ... & ... & ...
\end{bmatrix}^T
=
\begin{bmatrix}
n_1 & n_2 & n_3 & ... \\
m_1 & m_2 & m_3 & ... \\
l_1 & l_2 & l_3 & ... \\
... & ... & ... & ...
\end{bmatrix}
$$

After completing the above 5 steps, the original data sets with n di mensions can be transformed to a data set with a chosen dimension. The transformed data set with a dimension less than n can be plotted using a new axis whose directions are equivalent to those of the chosen eigenvectors. By doing this, the original data sets are linearly transformed and compressed to new data sets with a lower dimension and largest convariances, containing most of the information in the original data sets.

3.0   EXPERIMENT

3.1   TEMPLATE PREPARATION AND NANOCHANNEL FORMATION

The key issue in our experiment is to discover how to fabricate thin and uniform nanowires for different materials. In order to fabricate nanowires with diameters less than 100 nm, we used electrochemical deposition to deposit Pd/PPy/PANI/ZnO on a substrate with 100 nm wide channels that crossed pre-patterned gold electrodes. These electrodes function as working electrodes through which an electric field could be applied. This template was prepared using conventional microelectronic processes, including photolithography, e-beam evaporation, lift-off and e-beam lithography steps. Figure 3.1.1 illustrates the complete process [5]. In order to further limit the nanowire growth inside the PMMA channels with an even smaller diameter, we introduced another electric field directly beneath the nanochannel, which is similar to a back gate electric field. In this part, the fabrication processes for both non-gate and gate-incorporated templates are presented. The formation of PMMA nanochannel following the template fabrication is also included.

3.1.1   Non-gate Template Fabrication

We choose a (100) p-type Si wafer as the substrate. In step A, a certain thickness of SiO_2 is thermally grown to work as an insulation layer. Two different thicknesses have been used: 100
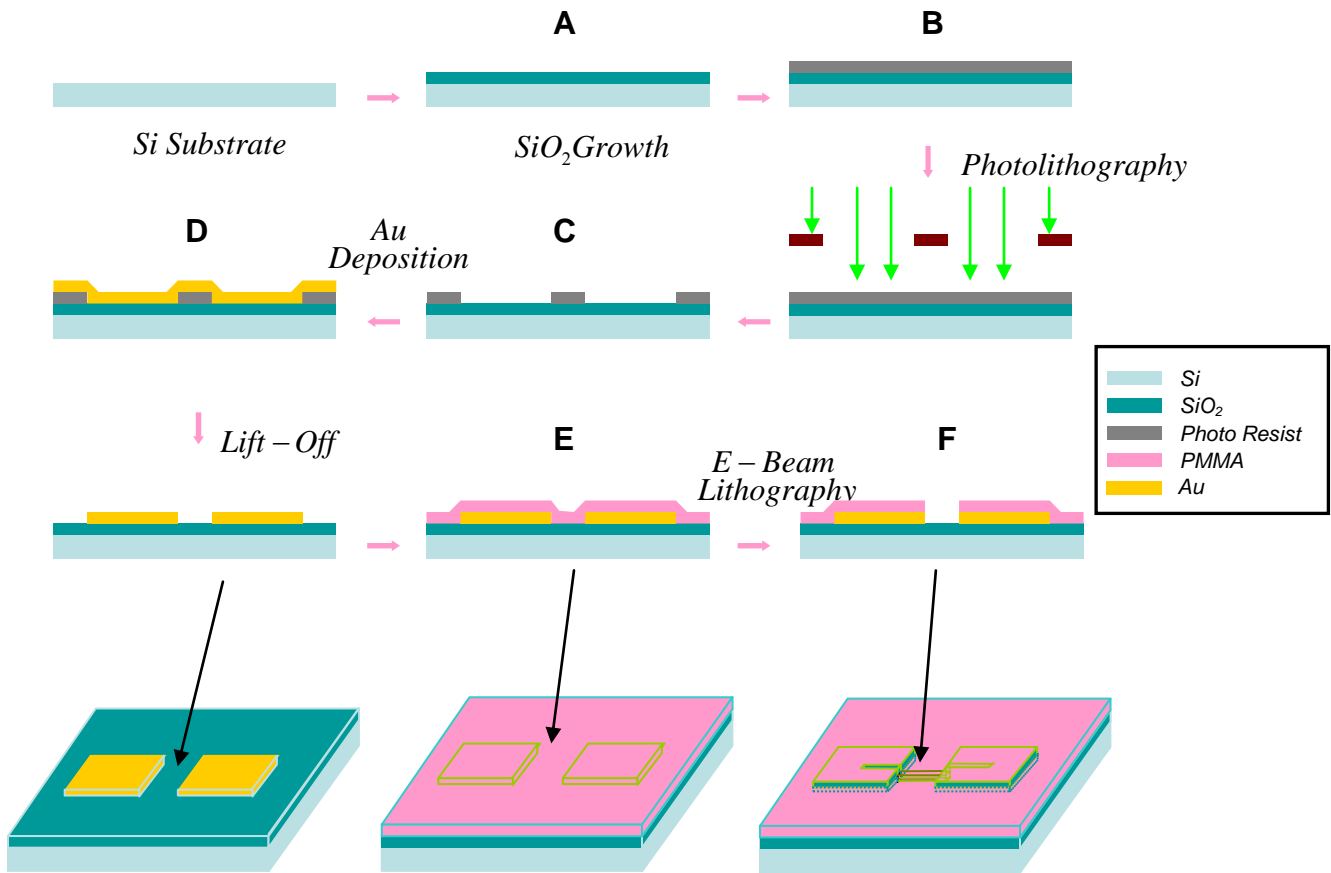
Figure 3.1.1 Fabrication process of template for 100 nm PMMA channels. A: 100 nm thick SiO2 growth; B: Photoresist spin-coating; C: Development of photoresist; D: E-beam evaporation of 5nm thick Ti layer as adhesion layer followed by 95nm thick gold layer as electrode. E: PMMA spin-coating; F: E-beam lithography and development of PMMA to pattern 100 nm wide nanochannels [5].

nm and 150 nm. In steps B and C, the pattern of Au/Ti electrodes is transformed using optical lithography. In step D, an adhesion layer of Ti with 5 nm thickness is deposited before the deposition of 95nm thick Au layer by e-beam evaporation. Then, the patterned photoresist is removed using warm acetone and Au/Ti electrodes are formed after lift-off. These electrodes will work as both the working electrodes during electrochemical deposition and the wire bonding pads. The formation of nanochannel for nanowire growth is done through steps E and F. In step E, a layer of 100 nm to 150 nm thick PMMA is spun on the substrate. After the e-beam lithography steps, nanochannels with desired width (e.g. 100nm or less) are formed in step F. A detailed recipe for e-beam lithography (EBL) can be found in [5]. The distance between electrode pads varies from 3 µm to 5 µm. These channels have a length of 15 µm or 20 µm across the gap between the electrode pads. Finally, a channel with two ends connected to Au/Ti electrodes and the upper side opened to air is formed. Figures 3.1.2 (A) and (B) present the AFM images of the nanochannel between electrodes. The 100 nm PMMA cover on top of the surfaces of both Au electrodes and SiO_2 provide a relatively flat surface. The edges of both electrodes are smooth, and Au spikes on the edges are carefully removed during the lift-off process. The nanochannel crosses both electrodes with good uniformity. Although the measured channel size is 150 nm wide, the actual size is expected to be smaller due to the AFM tip sharpness. The smallest width of the nanochannel can be made down to 30 nm, and the results will be discussed in the following sections.

3.1.2   Gate-incorporated Template Fabrication

The fabrication process for a template with gate structure is slightly different from that with a non-gate structure. The complete process can be shown in Figure 3.1.3 [46]. The addition of a
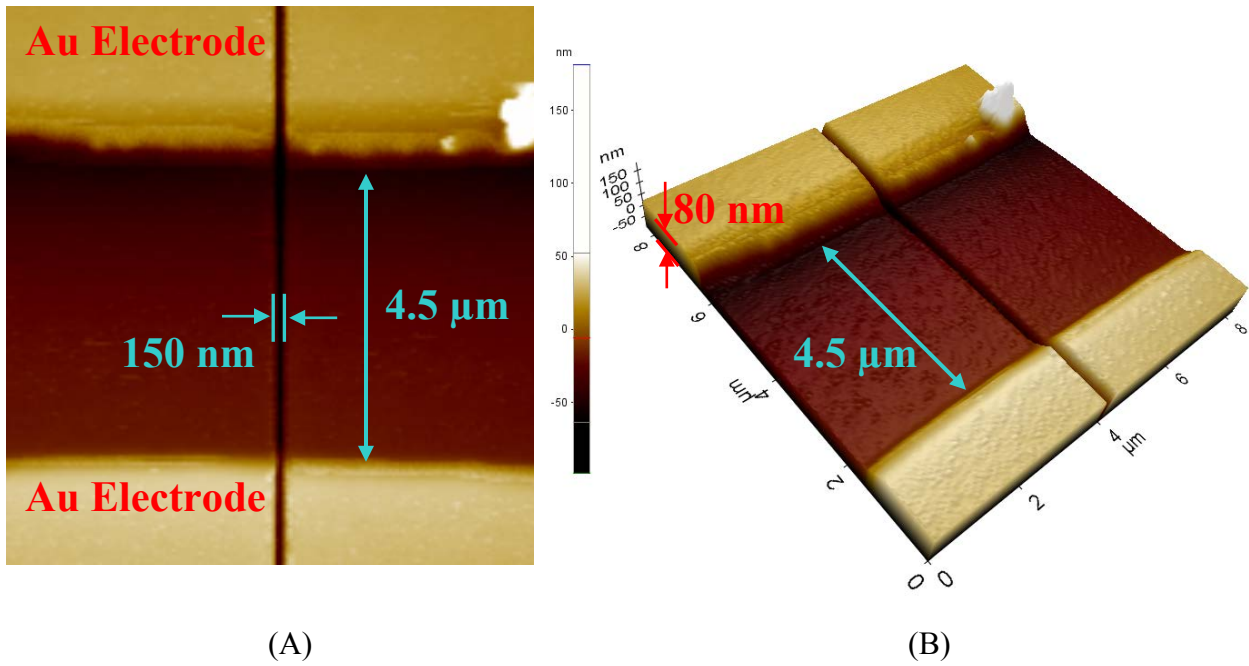
Figure 3.1.2 (A) An AFM image of nanochannel together with electrodes on both sides. The size of the image is 8×8 µm² and the channel length is 4.5 µm. (B) The 3-D view of the channel and electrodes. The height of the electrode is 100 nm and the depth of the channel is 100 nm.

gate electrode directly connected to the Si substrate is the main modification. Step (a) and (b) are the same as mentioned previously, while step (c) not only patterns the working electrodes but also opens a gate electrode area. In this step, the gate electrode area is first patterned with optical lithography followed by an etching step. The SiO_2 layer under the gate area is completely removed using buffered oxide etchant (BOE) to ensure the direct contact between the gate electrode and the Si Substrate. Another step of photolithography is then taken to pattern both the working electrodes and the gate electrodes. In step (d), the Ti/Au eletrodes are deposited by e-beam evaporation; a lift-off process completes the formation of both working and gate electrodes. Steps (e) and (f) are the same as the non-gate processes, except that a smaller channel diameter (e.g. 30~50 nm) can be applied in EBL in order to achieve the growth of nanowires with smaller diameters. A successfully fabricated 4 inch Si wafer with 69 1cm × 1cm chips is shown in Figure 3.1.4.

3.2 SINGLE NANOWIRE FABRICATION VIA ELECTROCHEMICAL DEPOSITION

Once the fabrication process of the template wafer is finished, the wafer is cut into small slices. The next step is electrochemical deposition of nanowires.

3.2.1 Preparation of Electrolyte Solution

The process of nanowire deposition is completed by placing a drop of electrolyte solution on top of the nanochannel and applying a constant DC current through it. The electrolyte solution for Pd

nanowire growth contains $Pd(NH_2)_2(NO_2)_2$ (Diamminepalladium Nitrite) and $NH_4SO_3NH_2$ (Ammonia Sulfamate) with concentrations of 10g/L and 100g/L, respectively [47]. In the solution, the two components would go through the following dissolution processes:

$$(3.1)$$

$$NH_4SO_3NH_2 \leftrightarrow NH_4^+ + NH_2SO_3^- \qquad (3.2)$$

Thus, this solution contains Pd^{2+} ions which work as the Pd source and will be reduced at the cathode side. During the electrochemical deposition process, the pH value of this solution is kept at around 7 by adding H_3NSO_3 (sulfamic acid) and NaOH (sodium hydroxide) to avoid reactions between the electrolyte solution and Au electrodes or PMMA.

The electrolyte solution for PPy nanowire deposition contains NaCl (sodium chloride) and pyrrole monomer (98%) with concentrations of 0.2 mol/L and 0.1 mol/L, respectively. Because the pH value of the pyrrole electrolyte is 6.5, no additional chemical is needed for neutralization. The electro polymerization of PPy undergoes exactly the same process covered in part 2.2.1 in this dissertation. The electrolyte solution for PANI nanowire fabrication contains 0.1 mol/L HCl (hydrogen chloride) and 0.01 mol/L aniline monomer, and the pH value is around 1. The acidic environment during electrochemical deposition is beneficial for the synthesis of highly conductive PANI, as section 2.2.2 describes. The fabrication of ZnO, which is more complex, will be discussed in detail in a later section. The electrolyte solution used for Zn nanowire fabrication is 5 mmol/L $ZnCl_2$ (zinc chloride) and 15 mmol/L NaCl, and the hydrothermal solution for ZnO fabrication is 50 mmol/L $Zn(OH)_2 \cdot 6H_2O$ and 50 mmol/L $C_6H_{12}N_4$ (HTMA). All the chemicals mentioned above were purchased from Sigma Aldrich.
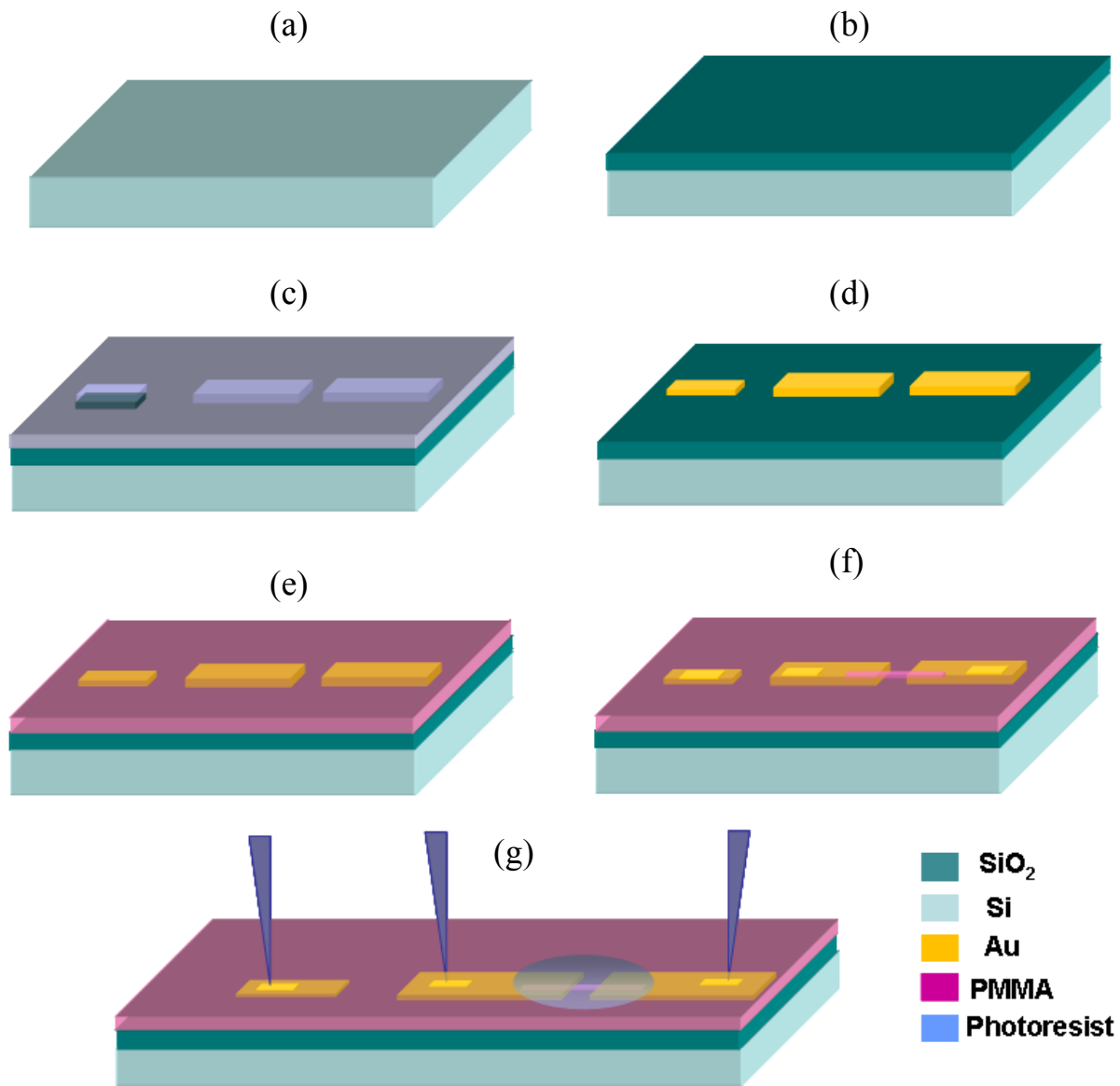
Figure 3.1.3. Schematic illustrations of template fabrication processes. (a) A p-type (100) silicon wafer is chosen. (b) A layer of SiO2 with 100 nm thickness is grown. (c) Photoresist is patterned for gold electrode deposition. The SiO2 layer under the gate area is etched through using BHF solution. (d) 100 nm thick Ti/Au is e-beam evaporated on the surface and patterned by a lift-off procedure using warm acetone. (e) A 100 nm thick layer of PMMA is spin-coated on top of the template. (f) PMMA channels of 30–100 nm wide are written across two electrodes by EBL. Open areas for electrode–probe contact are also formed. (g) Final set-up for nanowire growth. [46]

3.2.2 Nanowire Growth

The electrochemical deposition of the nanowire is finished on a probe station, which has of four separate probes with 1 μm diameter tips. The probes are connected via coaxial cables to a semiconductor analyzer (Agilent B1500A) which both supplies and collects electrical signals. For the non-gate growth, we use two probes and connect them to the two working electrodes on both sides of the channel. Then, we placed a drop of electrolyte solution (~0.5 μL) using a micropipette on the channel. After that, a constant current (10 nA~500 nA) is applied through the two probes; the voltage signals across the two electrodes are monitored by the semiconductor analyzer at the same time. Since the nanowire grows from cathode to anode and the resistance of the solution is much higher than the nanowire itself (Pd is metallic and PPy is highly conductive), we can always see a large voltage drop across the channel when the nanowire reached the anode; in other words, the voltage drop indicated the completion of the nanowire growth. The usual voltage between two working electrodes without a nanowire falls in the range from 3 V to 5 V. Once the nanowire is grown, this voltage dramatically drops to less than 1 mV. The growth current is stopped manually once the voltage drop happens to avoid further axial growth of the nanowire.

For the gate-assisted growth, an additional gate electric field was applied on the gate electrode through a third probe in addition to the current signal running between the two working electrodes. The polarity of the applied voltage is dependent on the charge of the ions in the solution. Since the Pd^{2+} ions in the Pd solution are positively charged, this voltage should be negative so that an attractive force pulls down the ions to inside the channel. Detailed information will be covered in later parts. An image showing the gate-assisted growth set-up is presented in Figure 3.2.1.
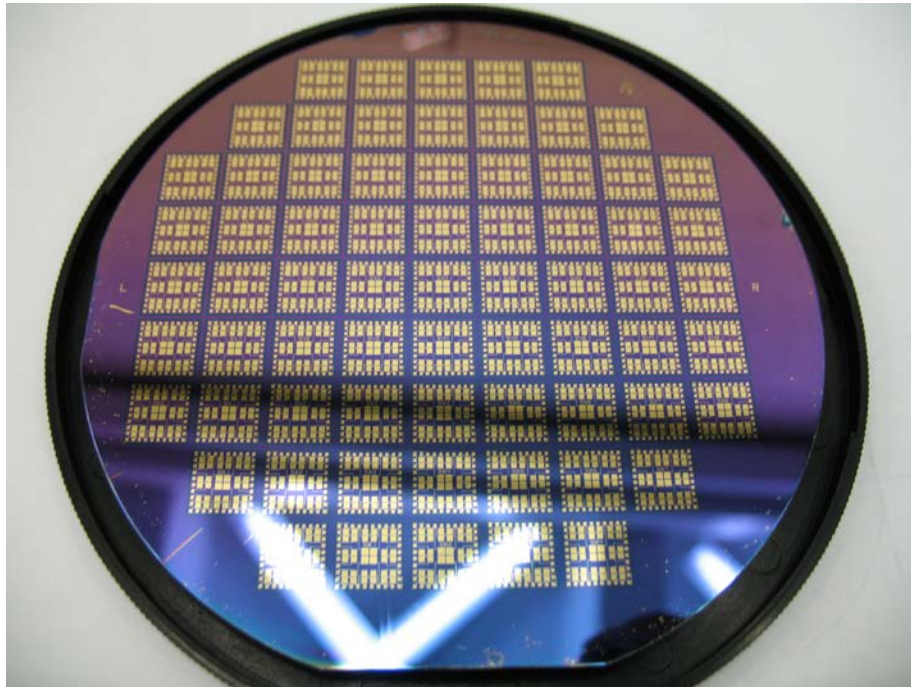
Figure 3.1.4 A 4 inch wafer with 69 1cm × 1cm chips.
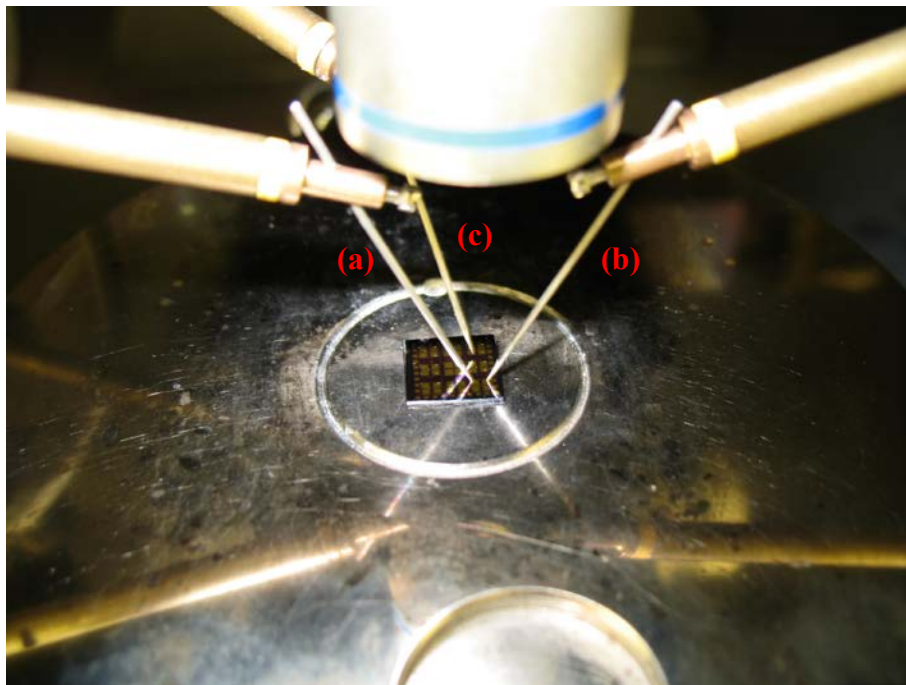
Figure 3.2.1 Probe station set-up for gate-assisted growth. Probes (a) and (b) are connected to two working

electrodes, and probe (c) connects with the gate electrode.

3.3   INTEGRATION OF SENSOR DEVICES

In order to use the nanowires in gas sensing, we have to integrate single nanowires into devices by adding external circuits. First, the individual chip on which nanowires are grown is attached to a 44-pin chip carrier. A wirebonding process is then done to connect the bonding pads (400 μm × 400 μm size) with the pins on the chip holder. The wirebonder is a manual wedge wirebonder provided by Kulicke & Soffa INC. After that, the chip carrier with the nanowire chip is plugged into a PLCC 44 socket, which has 44 output pins that can be used for electrical connections. A complete sensor device is shown in Figure 3.3.1.

3.4   GAS SENSING SYSTEM SET-UP

To detect different gases under different concentrations requires a gas sensing system which is able to not only turn on/off the gas flow from different gas sources but also control the gas concentration. Our test includes four different source gases: H_2 (10% and 0.1%), NO_2 (10 ppm), CO (2000 ppm) and CH_3OH (liquid phase in room temperature). We also use pure N_2 not only as the dilution and carrier gas, but also as the purging gas at the end of each gas injection cycle to reset the sensing environment. In order to ensure a short response time, a plastic gas sensing chamber with very small inner volume (29.4 ml) was fabricated. The sensing chip with nanowires is placed inside the box with the connection wires coming out. To make sure the source gases are well mixed with dilution gas (99.999% N_2), a mixing chamber with inner size of 12.6 mL is used, with inlets connecting to the source gas and the dilution gas and one outlet connecting to the sensing chamber. These two chambers are shown in Fig. 3.4.1. It is important
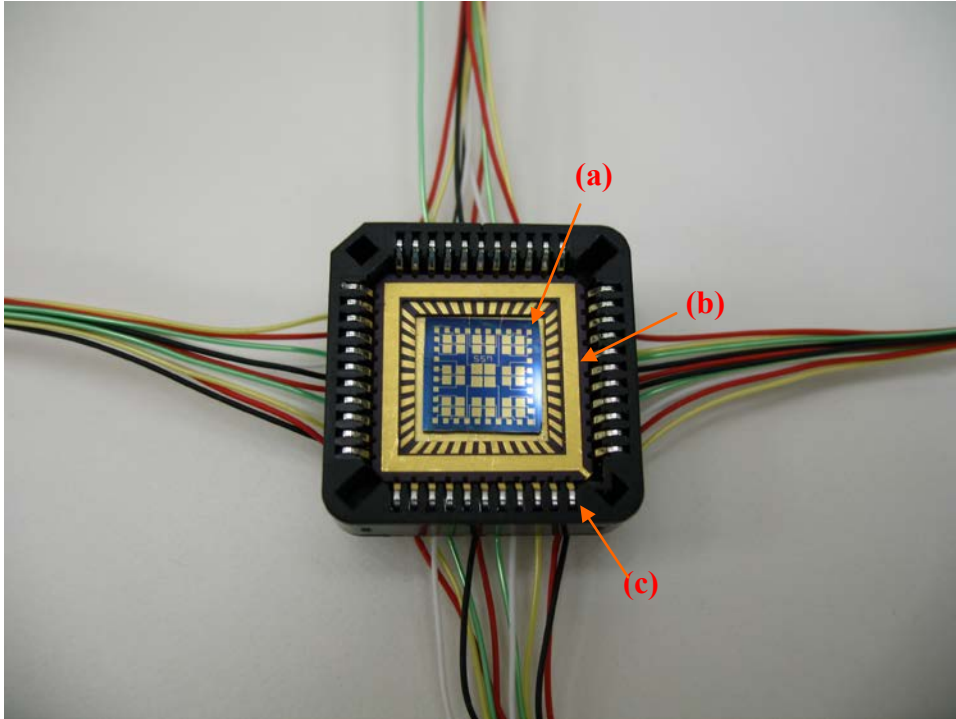
Figure 3.3.1 A sensor device with (a) nanowire chip, (b) 44-pin chip holder and (c) PLCC 44 socket. The output pins from the socket are connected to external electrical circuits for detection.
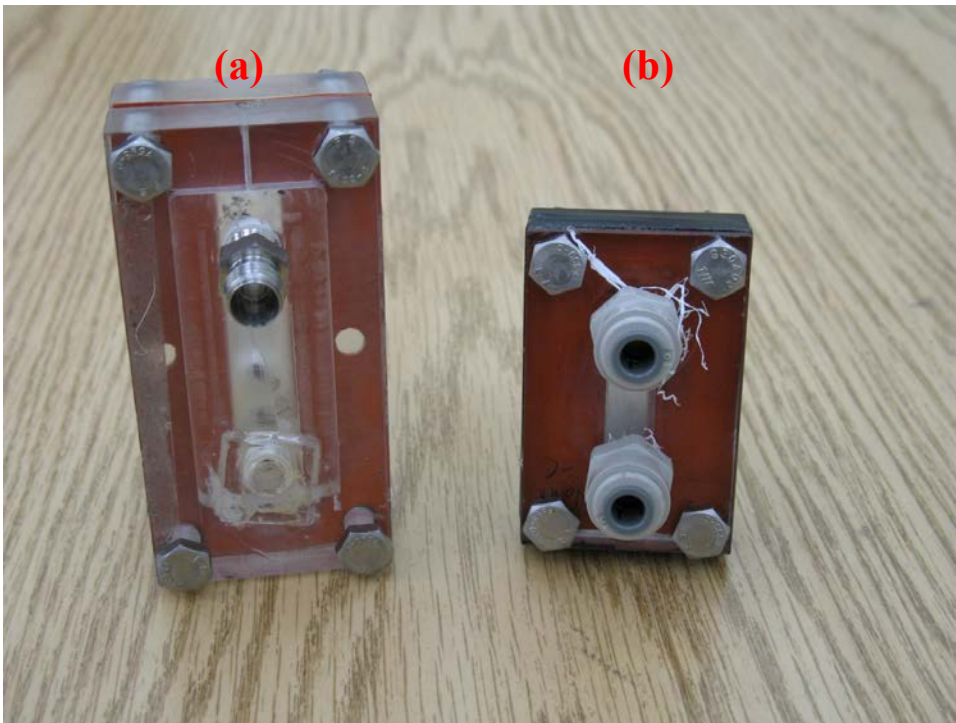
Figure 3.4.1 (a) Gas sensing chamber, and (b) gas mixing chamber.

to note that methanol is liquid in room temperature so a bubbler is necessary for the generation

of a CH_3OH gas mixture (99.999% N_2 as carrier gas). Finally, a control system is built to create

an interface between human and gas flow control. In this work, the control system consists of a

mass flow controller, four gas valves, and a computer software system.

The complete gas sensing system used in this work is illustrated in Fig. 3.4.2. A

LABVIEW (National Instrument Inc., USA) program is built to control the flow rate of all the

gas lines, including the target gas lines and the carrier and purging gas lines. In order to control

the gas flow rates, four different flow meter valves (MKS 1721 Mass Flow Meter) are connected

to a MKS flow control system (MKS Multi Gas Controller 647C, MKS Instruments Inc., USA)

which is directly controlled by the LABVIEW program. For any target gas, the desired

concentration is obtained by mixing the source gas with the dilution gas at certain flow rate ratio.

The actual mixed gas concentration can be calculated using the following equation:

$$C_m = \frac{C_1 F_1 + C_2 F_2}{F_1 + F_2}$$
(3.1)

in which C_m, C_1, and C_2 represent the target gas concentration of mixed gas, gas 1 (source gas),

and gas 2 (dilution gas), respectively. F_1 and F_2 represent the flow rate of gas 1 and gas 2,

respectively. Take hydrogen sensing for example: If gas 1 consists of 10% hydrogen and gas 2 is

pure nitrogen carrier gas, then C_1 and C_2 are 10% and 0, r espectively. Because of the

specifications of the gas valves, F_1 can reach a minimum value of 1 sccm, while F_2 can reach a

maximum value of 500 sccm. Therefore, C_m can reach any value from 10% to 0.02% (200 ppm)

based on Eq. 3.1. By setting a proper flow rate ratio between source gas and dilution gas, any

desired concentration of target gas is obtainable as long as it is within the limit of the system.
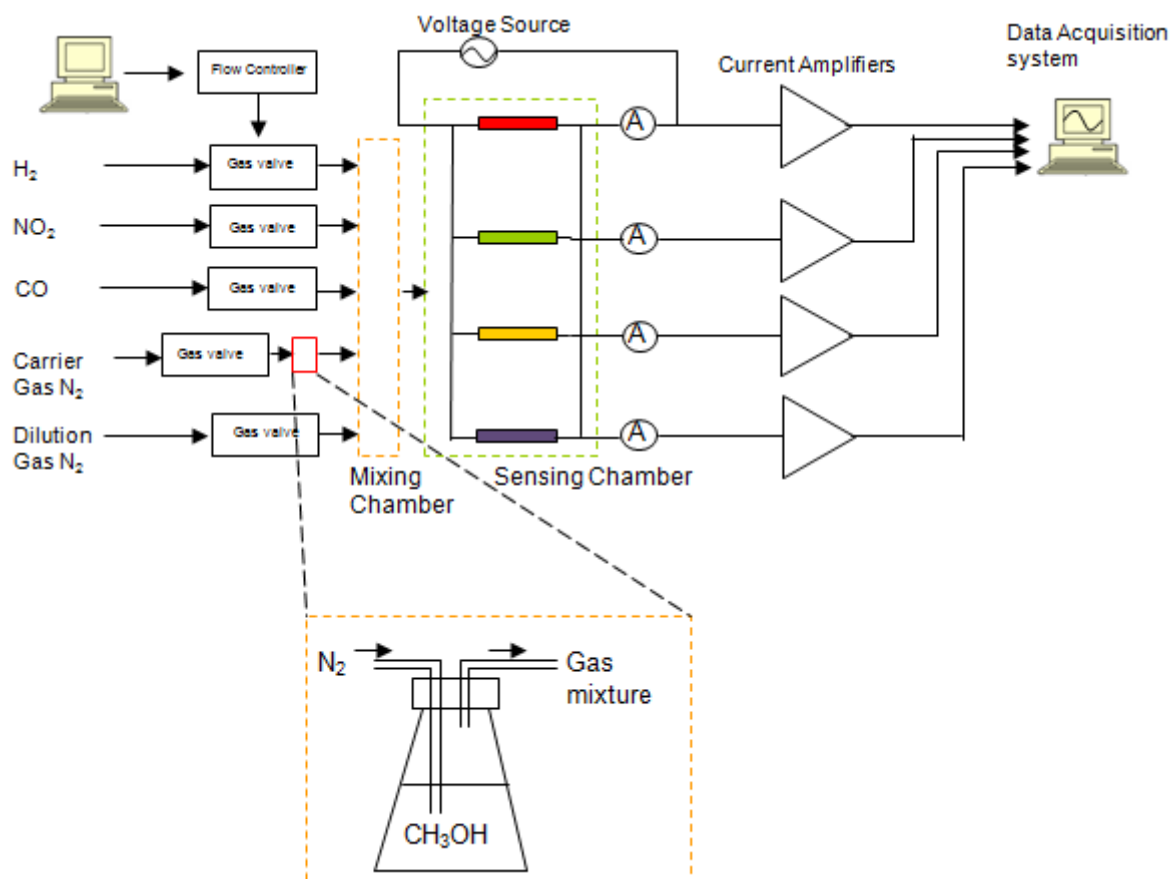
Figure 3.4.2 Complete sensing system for multiple gas sensing.

3.5 SIGNAL COLLECTION AND PROCESSING

In order to detect the resistance change of nanowires during the gas sensing, a constant DC voltage (~17 mV) is applied to individual nanowire via a current amplifier (Keithley 428 Current Amplifier). This instrument not only acts as a stable voltage supplier, but also collects the current signal from each nanowire and converts it to an amplified voltage value. The amplification

ranges from 10^3 to 10^{10} V/A. A data acquisition system (Keithley 2701) collects this output voltage signal and a LABVIEW program records it. The final sensing chart based on the collected data can be analyzed and plotted using Excel and Sigma Plot 10.

4.0   RESULTS AND DISCUSSION

4.1   NANOWIRE GROWTH AND PROPERTIES

By using electrochemical deposition, we were able to successfully and constantly fabricate Pd, PPy and PANI single nanowires with diameters less than 100 nm. In order to study the surface, electrical, and structural properties of nanowires, we used a Semiconductor Analyzer, Optical and Scanning Electron Microscopy (SEM), and Atomic Force Microscopy (AFM) to carry out the characterizations.

After a nanowire is grown on the wafer slice, it is cleaned by gently rinsing it in deionized (DI) water and then dried by using pure dry nitrogen gas. An image of the nanochannel and nanowire is taken using optical microscope (Carl Zeiss AG Reflected-Light Microscope) to verify the growth. Optical microscopic images of a nanochannel before and after a Pd nanowire growth with a magnification of 150×10 times are shown in Figures 4.1.1(a) and (b). It is clear in Figure 4.1.1 (a) that a PMMA nanochannel (thin dark line) is formed after e-beam lithography and it bridges both electrodes. After the nanowire is grown, we can see dark deposits on one of the electrodes (cathode) and a tiny dark line inside the nanochannel. Since the maximum magnification is 1500 times, the diameter (~100 nm) of the nanowire is too small for the nanowire to be clearly observed.
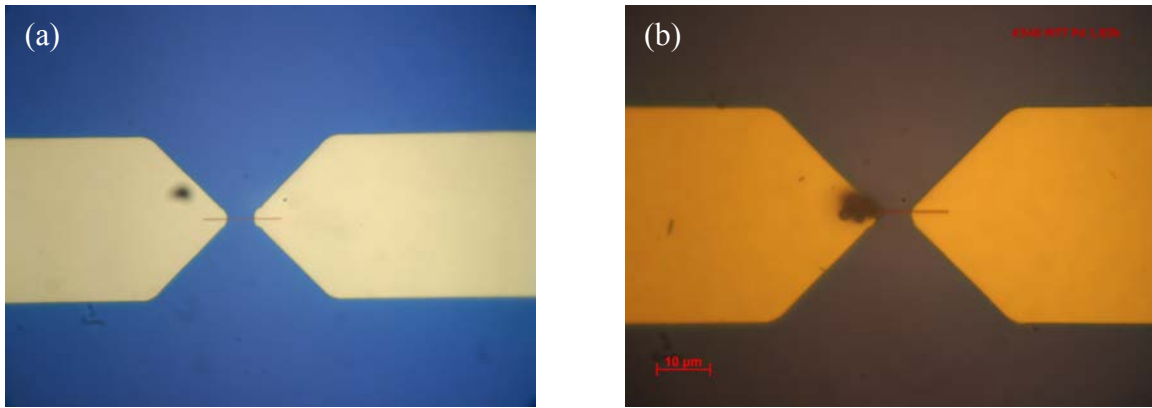
Figure 4.1.1 Optical images under 1500 time magnification of (a) the nanochannel and (b) a Pd nanowire.
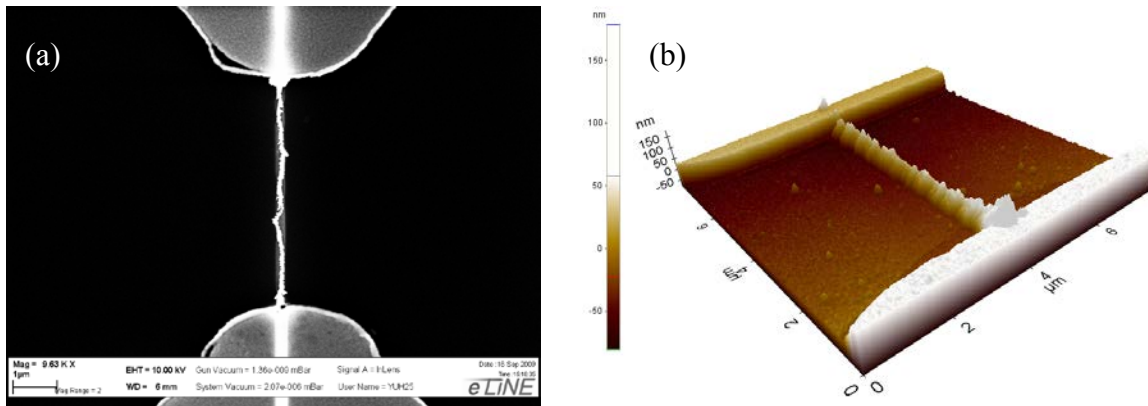
Figure 4.1.2 (a) An SEM image of a Pd nanowire with 100 nm diameter and 7.02 kΩ resistance. (b) An

AFM image of another Pd nanowire with 100 nm diameter and 5 μm length.

In order to further study the surface properties, SEM system (Raith e-line) and AFM system are used to take clearer images of the nanowire. An SEM image of a Pd nanowire is presented in Figure 4.1.2 (a) and an AFM image of another Pd nanwire is presented in Figure

4.1.2 (b). In the SEM image, it is clear that the axial growth of nanowire is constrained by the nanochannel, confirming our idea of using a PMMA channel to limit the nanowire growth. Since the nanowire is grown inside the 100 nm thick PMMA channel, the AFM image can only be taken after removing the PMMA layer by soaking in warm (45°C) acetone for 5~10 min. Figure 4.1.2 (b) shows that the morphology of the nanowire is quite uniform across the electrode gap with an average height of 74 nm, which is very close to the height of PMMA layer thickness (100 nm). The difference between these two may be caused by two reasons: First, the nanowire is not a perfect cylinder but wider in its diameter and shorter in its height, which was also reported in other studies [48]; Second, there might be very tiny amount of PMMA residual on the substrate, which effectively reduces the measured height of the nanowire.

4.2   PALLADIUM NANOWIRE STRUCTURE AND GROWTH CONTROL

As seen in Figure 4.1.2 (a), even though the nanowire is constricted inside the nanochannel, it is not a perfect cylinder structure, but a complex structure consisting of many tiny grains. Nanowires can have different structures depending on the size of these grains and the way they connect with each other. In this work, three different kinds of structures have been found for Pd nanowire: (1) plain structure, (2) grainy structure, and (3) hairy structure. SEM images of these structures are shown in Figure 4.2.1 (a) to (f) [5]. Plain structure nanowires, as shown in Figure 4.2.1 (a) and (b), are composed of very tightly packed particles that are well connected to each other with no gaps. The diameter of this kind of nanowire is relatively uniform along the channel, and the surface is relatively flat. The grainy structure nanowires consist of small nano-sized grains, each barely connected to the others via a very small neck, as shown in Figures 4.2.1 C
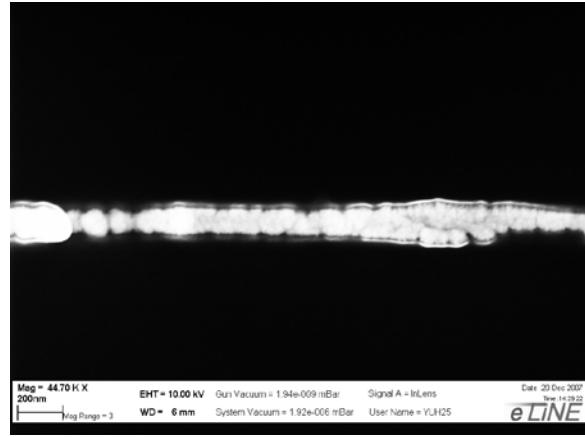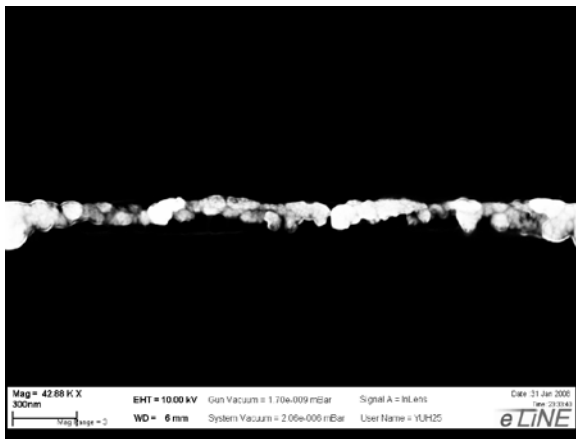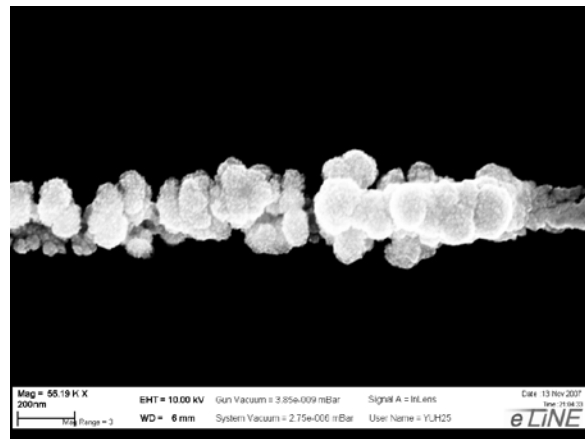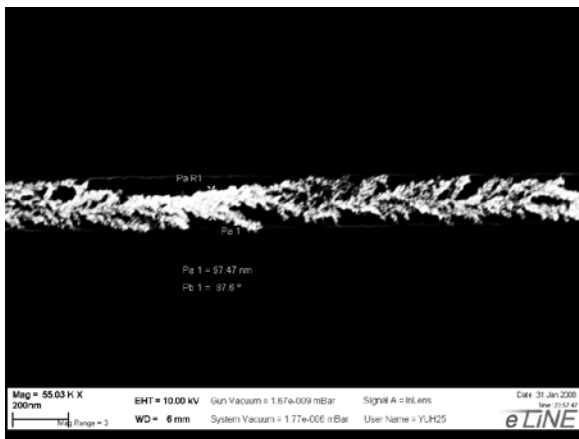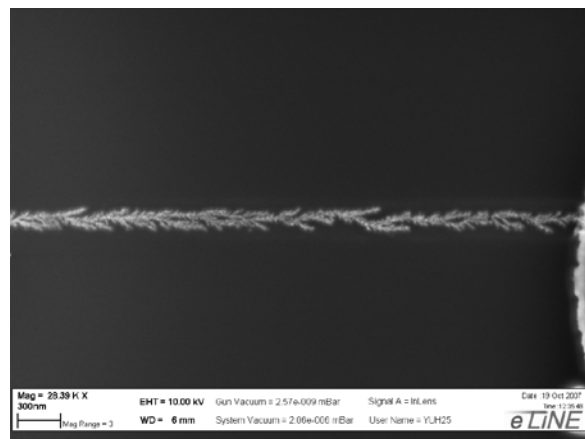
Figure 4.2.1. SEM images for three different nanowires structures: (a) and (b): Plain structure nanowires with 85 nm diameter; (c) and (d): Grain structure nanowires with diameter ranging from 100 nm to 150 nm; (e) and (f): Hairy structure nanowires with ~100 nm diameter [5].

and D. The diameter of this kind of nanowire varies along the channel; the grains are approximately 50~100 nm in diameter while the neck part can be as small as 10 nm or 20 nm. Hairy structure nanowires, shown in Figures 4.2.1 (e) and (f), have a trunk in the center and many dendrite-like branches reaching outward. The length of the dendrites is limited by the width of the channel. Through extensive experiments, we found that the structure of the nanowire is closely related to the growth current during electrochemical deposition. Figures 4.2.2 (a) to (c) show three SEM images with three different growth currents of 500 nA (a), 100 nA (b), and 50 nA (c). These images indicate a clear relationship between current and nanowire structure. These tests use the same 6 μm long and 100 nm wide nanochannels. With a higher current, the nanowire tends to grow faster and produce more dendrites, as shown in Figure 4.2.2 (a). With a lower current the growth is comparatively slower and produces a grainy structure shown in Figure 4.2.2 (c). Interestingly, with an intermediate current, the nanowire could show grainy structure on the cathode (left) side and hairy structure on the anode (right) side, as shown in Fig. 4.2.2 (b). Thus setting a different growth current can control the actual structure of the nanowire.

A possible explanation for the above mentioned phenomenon could be reached by considering the deposition as a combined process of grain growth and electric field driven aggregation. During electrochemical deposition, the grains already deposited are growing, while metal ions are driven by the electric field and attaching to the tip of grown nanowire. The applied current is the key factor that decides the growth speed while the electric field strength decides the directional aggregation. The competition between the grain growth (axial growth) and the electric field driven aggregation (lateral growth) determines the final structure of the nanowire. A higher current (higher electric field in the channel) would boost the aggregation of metal ions along the channel so that the electric field driven aggregation is much faster than the growth of
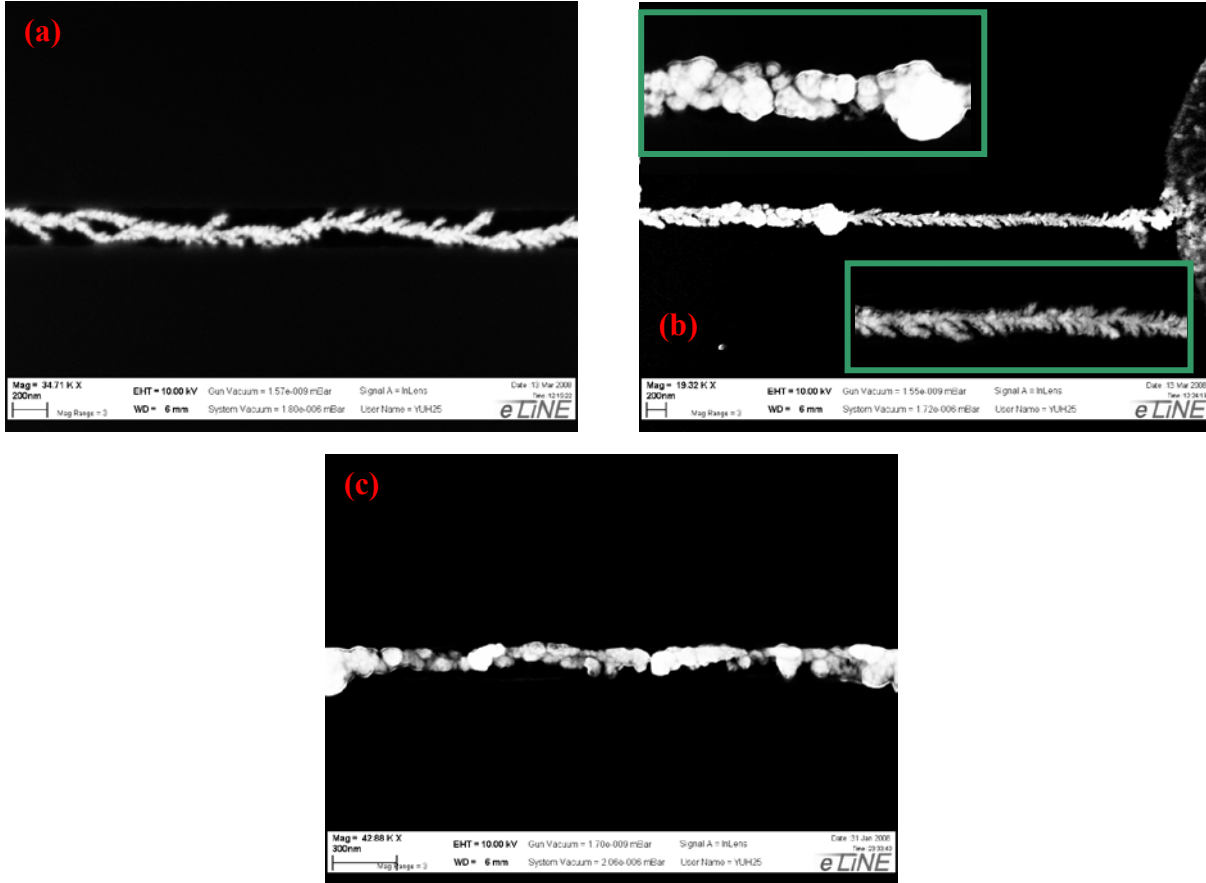
Figure 4.2.2 SEM images for nanowires grown using three different currents: (a) 500nA growth current; (b) 100nA growth current. The upper left inset is a magnification of the left side, and the bottom right inset is a right side magnification; and (c) 50nA growth current [5].

the grains. In this case, the shape of the nanowire resembles that of diffusion limited aggregation [49] and the grains are notably smaller. A smaller current (smaller electric field), on the other hand, would favor the grain growth as the nanowire grows slowly in the lateral direction. Thus a nanowire with the grainy structure forms. Both scenarios can happen in an intermediate current

since the electric field inside the channel is small in the early stage of the nanowire growth (nanowire tip far from the anode), which favors the growth of grains, but gets larger in the late stage (nanowire tip close to the anode), which results in a hairy structure.

4.3   PALLADIUM NANOWIRE BASED ULTRASENSITIVE HYDROGEN SENSOR

In this work, a highly sensitive hydrogen sensor is fabricated based on single Pd nanowires. This sensor is superior in its low detection limit (~2 ppm), which proves that a Pd single nanowire structure is highly sensitive towards hydrogen. The performance of this sensor is characterized by the following factors: detection limit, repeatability, and response time.

(1)   Detection limit

The detection limit of our devices is superior with a lowest value of 2-5 ppm. This value is the best ever achieved using pure palladium and much better than similar hydrogen sensors made by Pd nanowire arrays [23] and Pd nanowire bundles [24], although similar result was recently reported by [50]. Figure 4.3.1 shows a real time sensing signal with a 2~5ppm detection limit. During the test, different hydrogen concentrations were introduced into the chamber, following a 1000 ppm – 100 ppm – 50 ppm – 20 ppm – 10 ppm – 5 ppm – 2 ppm – 1000 ppm – 100 ppm – 10 ppm – 5 ppm – 2 ppm manner. This sensor is not only able to detect hydrogen with concentrations ranging from 10,000 ppm (1%) to 5 ppm (0.0005%) consistently and repeatedly, but it can also discriminate different concentrations with different signal amplitudes.
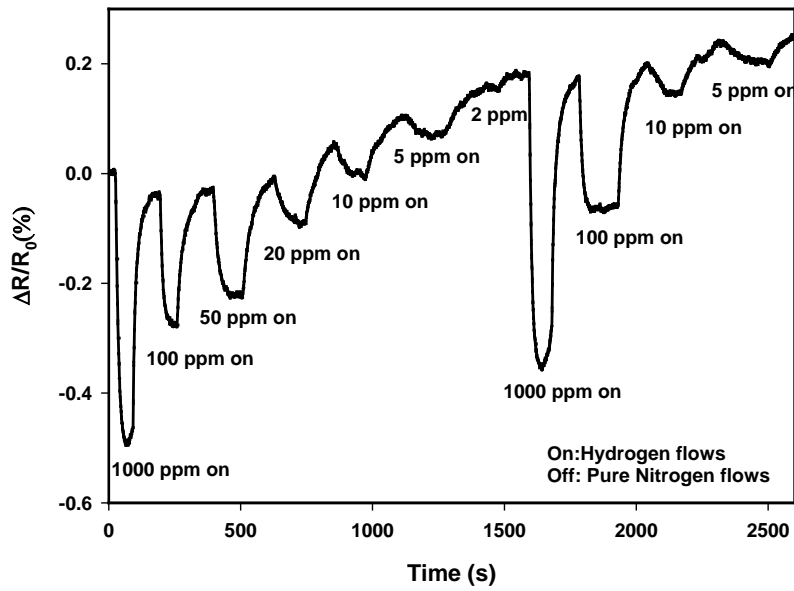
Figure 4.3.1. A sensing result of ultra high sensitivity with a 1000 ppm – 100 ppm – 50 ppm – 20 ppm – 10 ppm – 5 ppm – 2 ppm – 1000 ppm – 100 ppm – 10 ppm – 5 ppm – 2 ppm sensing order. It is a positive signal [5].
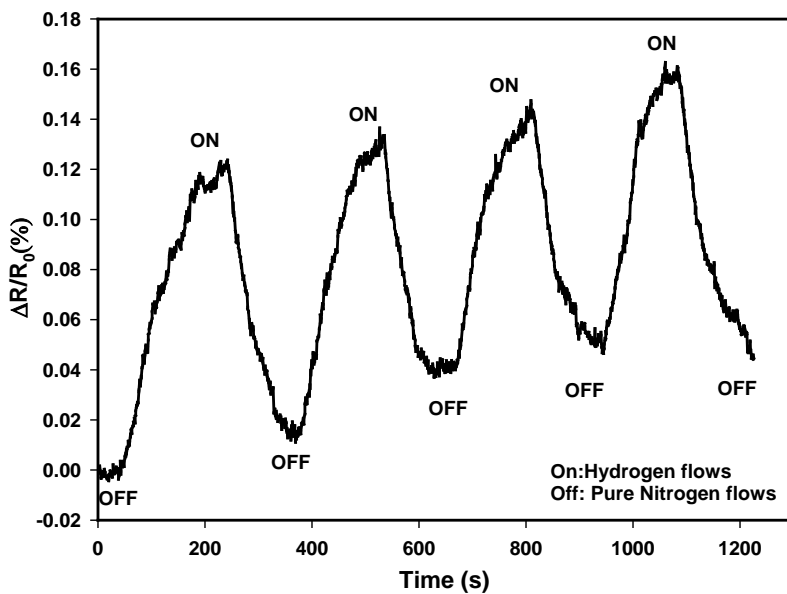
Figure 4.3.2. A sensing result of 5000 ppm hydrogen gas with negative signals [5].
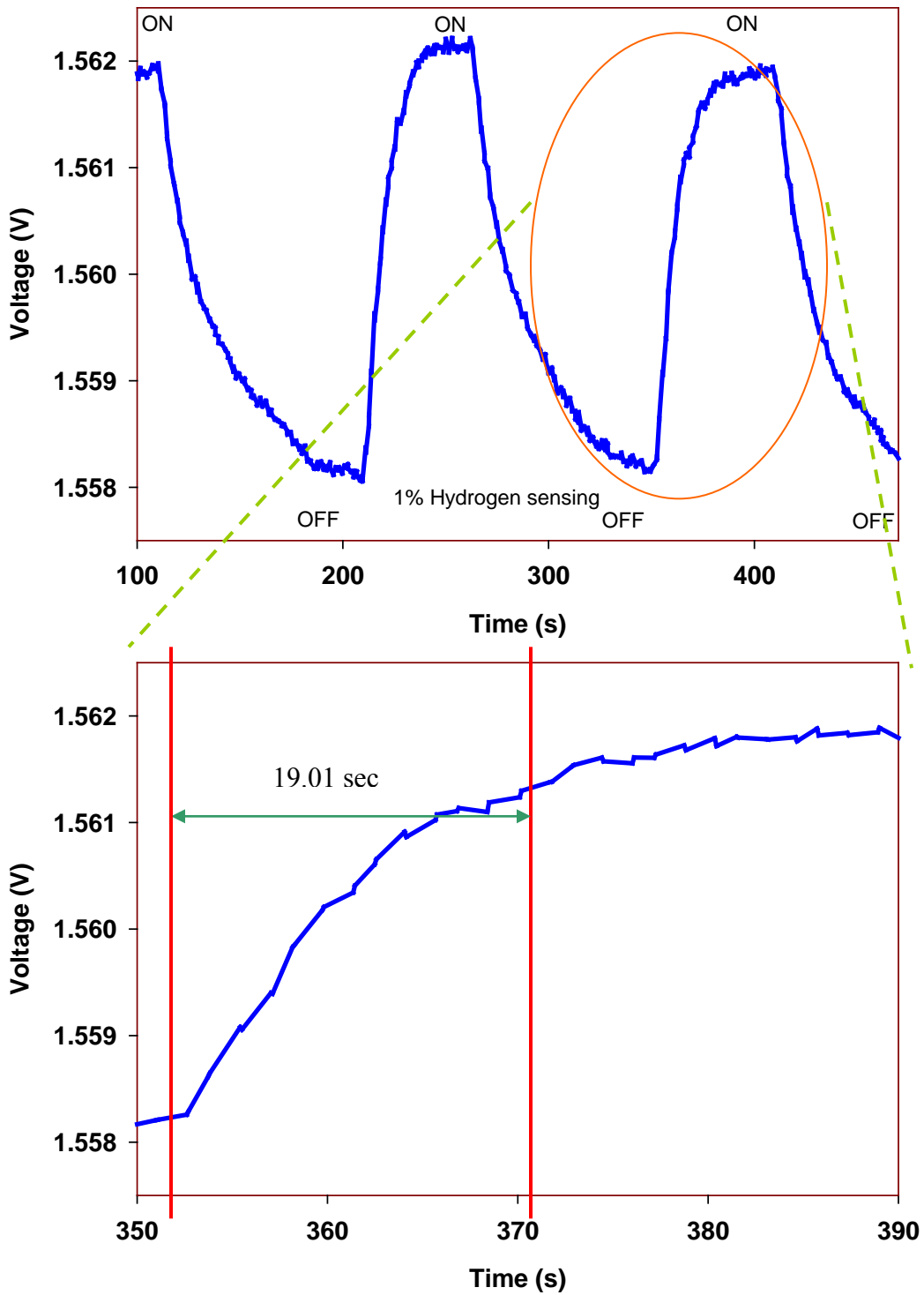
Figure 4.3.3. A sensing result of 1% hydrogen with positive signal. The rise time is around 19 seconds.

(2)   Repeatability

The sensor devices showed a very good repeatability during hydrogen detection. In Figure 4.3.2, a sensing result with a constant hydrogen concentration (5000 ppm) is presented. It is obvious that the sensing signal is reproducible and maintains a fairly constant signal amplitude.

 (3)   Response time

According to a common definition, the response time of a sensor is the time required for the sensor output to change from its initial state (10% value change) to a final value (90% value change). Fast response is critical in hydrogen detection, especially in aircrafts and spaceships where hydrogen leakage is quick and fatal. The sensor devices in this work showed a short response time ranging from 9 seconds to a few tens of seconds. The real response time is expected to be shorter considering the gas diffusion time inside the gas lines from the tank to the sensing chamber. As Figure 4.3.3 illustrates, a 1% hydrogen sensing signal shows a response time of roughly 19.01 seconds and proves the fast response of single nanowire sensors.

In summary, the hydrogen sensor based on a single Pd nanowire showed a great detection limit, good repeatability, and a short response time, all of which conform that our attempt of using single nanowire structure in gas detection is successful and promising. More importantly, the results show the potential of using several single nanowires in an array for the detection of more target gases.

In addition to the basic studies of hydrogen sensors, an unexpected phenomenon was discovered during the tests. By taking a closer look at Figures 4.3.1 and 4.3.2, we can see that the resistance changes of these nanowires upon exposure to hydrogen differ. In Figure 4.3.1, the nanowire experienced a resistance decrease when hydrogen was introduced. However, the nanowire in Figure 4.3.2 s howed an increased resistance when exposed to hydrogen. This

phenomenon indicates that, even fabricated in the same way through electrochemical deposition, a different Pd could show diverse sensing behaviors. In order to understand the underlying reason for this phenomenon, we conducted an extensive study and found that the sensing mechanism of a Pd nanowire is directly related to its actual structure.

As demonstrated in previous sections, the Pd nanowire can have three structures when a different growth current was applied. Therefore, detailed research based on these three different structures has been done to study the relationship between the sensing mechanism and the nanowire structure. In part 2.1.2 we mentioned that two effects could happen to Pd nanowires when exposed to hydrogen: resistivity increase and volume expansion. Because volume expansion often results in an increase of contact area between grains, a decrease of resistance occurs when volume expansion is dominant. For easier discussion, we call the resistance decrease ($\Delta R/R < 0$) during hydrogen exposure a positive signal, since the conductance goes up. The resistance increase or conductance decrease ($\Delta R/R > 0$) is called a negative signal since the conductance goes down. The two opposite effects compete with each other while the final direction of resistance change depends on the dominant effect.

For the plain structure nanowires, measurements showed mostly negative signals when the nanowires were exposed to hydrogen. An SEM image of a plain structure nanowire is shown in Figure 4.3.4; the corresponding hydrogen (5000 ppm) sensing response from the same nanowire appears in Figure 4.3.2. The response, which illustrates that this nanowire presents a negative signal when exposed to hydrogen,. can be explained by considering the two effects together. The resistivity change that resulted from the transition from α phase to β phase could increases the resistance of the nanowire a maximum of 180%. The size expansion (3.36% lattice

57
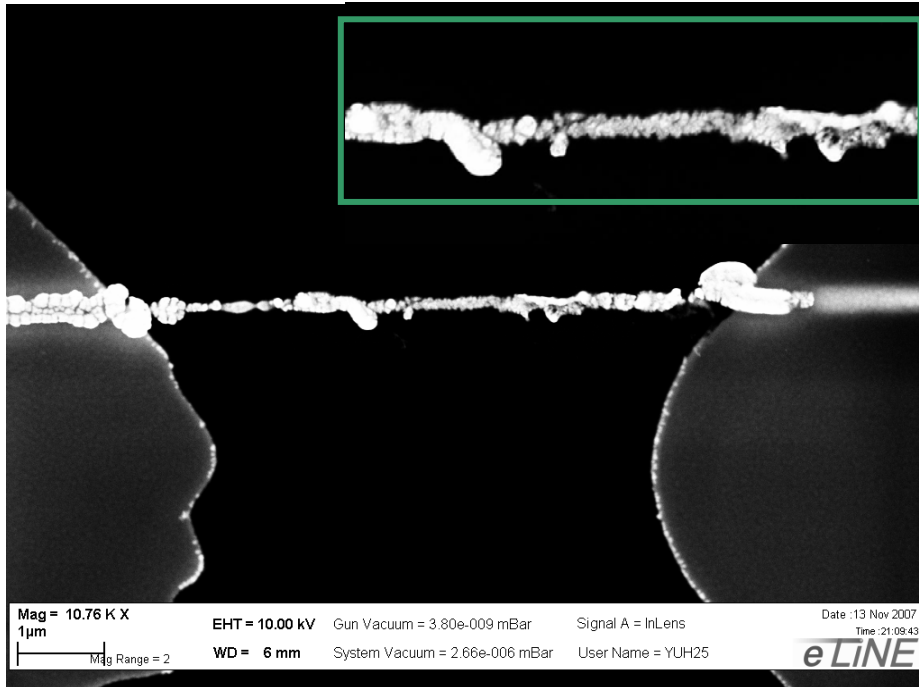
Figure 4.3.4 SEM image of a plain structure nanowire with a negative signal. This nanowire has a diameter of 100 nm and length of 6.5µm [5].
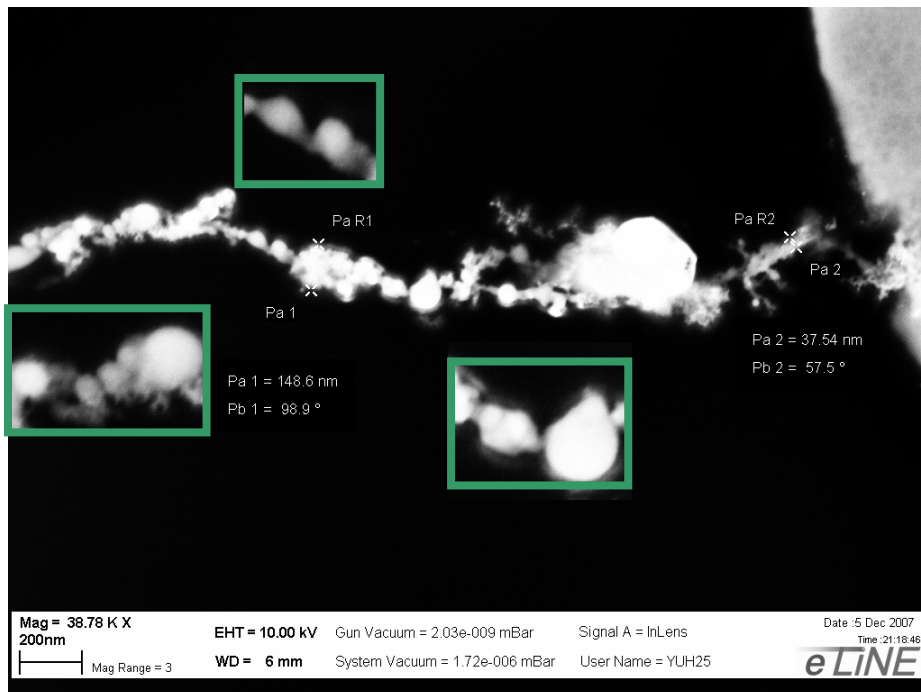
Figure 4.3.5 SEM image of a grain structure nanowire with a positive sensing signal. This nanowire has a diameter from around 150 nm to less than 30 nm; its sensitivity is 5 ppm [5].

constant expansion), however, would only result in a contact area increase of 6.8% and would decrease the resistance of the nanowire by 6.8% at the most. It is obvious that resistivity change is dominant and the final trend is a resistance increase, thereby causing a negative signal to appear.

For the grainy structure nanowires, positive signals were mostly seen in the sensing tests. The grainy structure nanowire shown in Figure 4.3.5 presents a positive sensing signal toward hydrogen, as illustrated in Figure 4.3.1. Because of its grainy structure, the volume expansion effect becomes more important than the resistivity change. While resistivity change still results in a 180% increase of resistance, the volume expansion results in a significantly more resistance decrease due to a dramatic increase of contact area. Consider a pair of grains together with a tiny neck between them. The contact area in the neck could increase in two possible ways: a) a 6.8% area increase because of its own 3.36% lattice expansion; and b) a much bigger area increase because of the compression from neighboring grains due to the volume expansion. Since the sizes of the grains range from 50 nm to 100 nm and the size of the neck is typically 20 nm to 30 nm, the expansion of the neighboring grains could introduce a strong compression force on the neck and greatly increases the contact area. In extreme cases this effect could result in a connection/disconnection between the grains and electrical switches were realized based on this phenomenon [23]. In this case the conductance increase caused by the contact area increase can override the conductance decrease caused by resistivity change and produce a positive signal.

The hairy structure has a much more complicated sensing mechanism than the mechanisms of the plain structure and grainy structure. Interestingly, both positive and negative sensing signals can happen in this structure. The sensing behavior is a combination of two effects

(resistance increase due to the resistivity change and resistance decrease due to the volume and contact area increase) and the final signal change depends on the actual nanowire structure [5].

Therefore, the sensing behavior of Pd single nanowires depends on the actual nanowire structure. Two different sensing signals have been found, and possible mechanisms have been proposed for the three different nanowire structures. In order to fully understand the structural and electrical change of the Pd nanowire upon exposure to hydrogen, more detailed studies, such as high magnification lattice characterization using TEM, are required.

4.4   GATE-ASSISTED NANOWIRE GROWTH

Pd single nanowires with a 100 nm diameter or less have been successfully and repeatedly fabricated using the non-gate electrochemical deposition method. However, this method still suffers from a low success rate and a limitation of minimal nanowire diameter (around 100 nm), due to the fact that nanowire tends to easily grow outside the channel. By introducing the gate-assisted growth method, the nanowire growth can be better confined, especially in the vertical direction, in the channel. The minimal nanowire diameter can be reduced to sub-50 nm; an improved nanowire structure was also observed.

The comparison between non-gate method and gate-assisted method is illustrated in Figure 4.4.1 [46]. 3D and cross-sectional illustrations of the substrate and nanochannel without (Figures 4.4.1 (a) and (c)) and with (Figures 4.4.1 (b) and (d)) the gate electric field show distinct differences: compared to Figure 4.4.1 (a), an additional electric field is applied via probe C in Figure 4.4.1 (b), while a constant current is applied through probes A and B. The real set-up in a probe station has been shown in Figure 3.1.5. Without applying the gate electric field (Figure

4.4.1 (c)), the ionic particles (Pd^{2+} ions) would distribute rather randomly inside the solution, and the concentration of the ions would be both laterally and vertically uniform. Once the growth current is applied, the growth starts immediately and ions aggregate to the cathode from every direction. Because this process presents a lack of control in the vertical direction, an easy overgrow of the nanowire, especially in the cathode side, happens. By applying the additional electric field through the Si back gate, an additional force is exerted on ionic particles to cause a
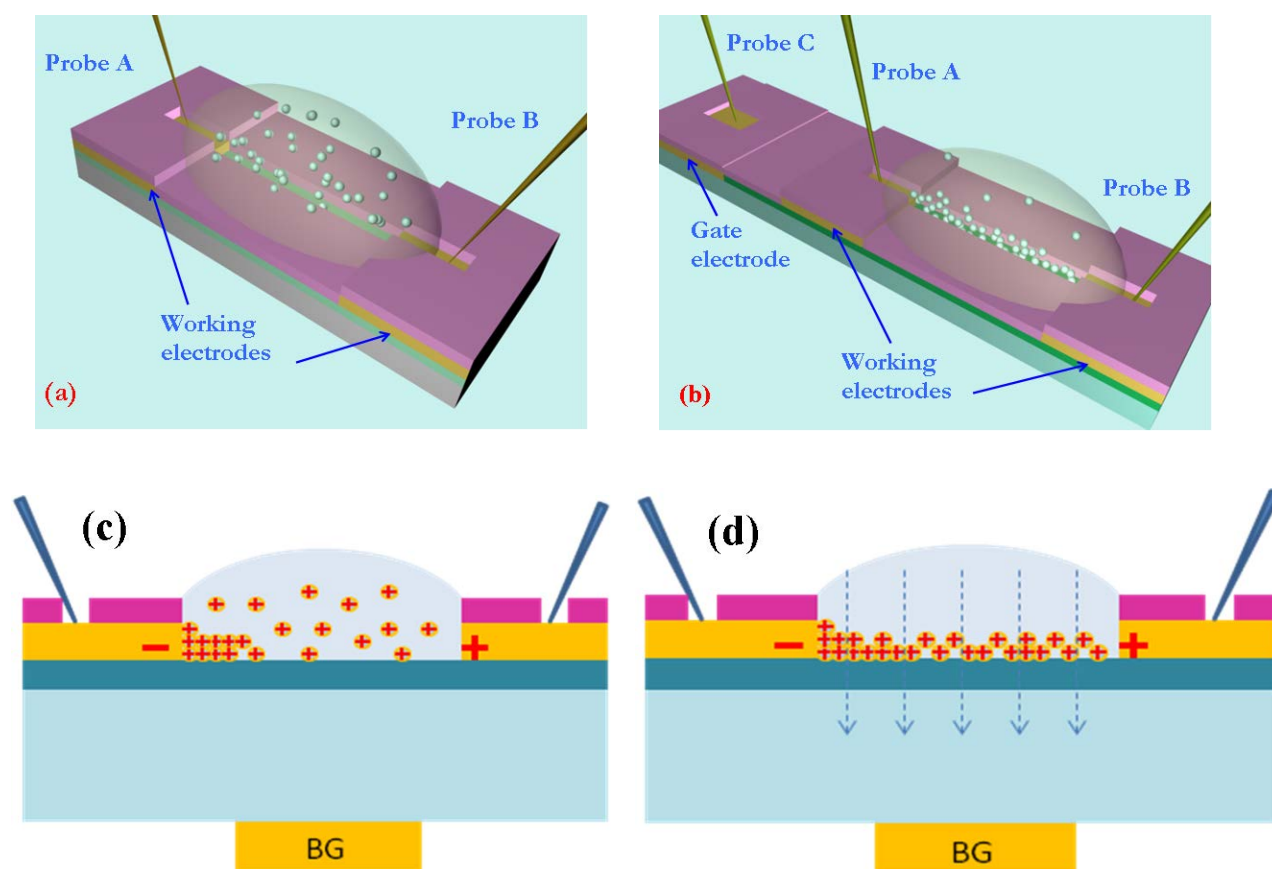
Figure 4.4.1 Illustrations of deposition set-up with and without a gate electric field, respectively. (a) 3D view of non-gate configuration and (b) 3D view of gate-assisted configuration. (c) Ion distribution of (a). (d) Ion distribution of (b). [46]

redistribution of the Pd ions in the electrolyte solution. As a result, the ion concentration is higher along the bottom of the channel (Figure 4.4.1 (d)). In this case, the growth will be better confined along the bottom of the channel and the out-growth of the nanowire will be contained.

Experiments have been conducted to study the effect of a gate electric field on single nanowire growth. Figures 4.4.2 (a)–(d) present four SEM images of Pd nanowires grown inside 100 nm wide by 6.5 μm long PMMA channels using gate voltages of +10 V, 0 V, −5 V and −10 V, respectively [46]. In all four cases the nanowires were grown under the same lateral growth current of 50 nA. As shown in the SEM images, nanowire growth is largely dependent on gate voltage. In Figures 4.4.2 (a) and (b), the nanowires were grown under a positive gate voltage and zero gate voltage, respectively, and the growth of nanowires was not uniform, with major parts growing outside the channel. On the cathode side, the nanowire tends to have a larger diameter, which could be due to 2 reasons: 1) the ions got attracted to the cathode from every angle when the nanowire growth started, especially in the vertical direction; and 2) the longer growth time in the cathode side allowed more axial growth in the cathode side than other parts of the nanowire. Comparing Figures 4.4.2 (a) and (b), we see that positive gate voltages degrade the growth, possibly due to the fact that Pd^{2+} ions carry a positive charge which causes an expelling force by the positive gate electric field resulting in a difficult Pd nucleation and growth inside the nanochannel. In contrast, a negative gate voltage is demonstrated to improve the nanowire growth in the nanochannel, as shown in Figures 4.4.2 (c) and (d). In Figure 4.4.2 (c), a −5 V gate voltage is applied and the nanowire is much better confined in the nanochannel and the out-growth of the material is greatly reduced. The negative gate voltage attracts the positively charged Pd^{2+} ions to the nanochannel during the deposition, reducing the ion concentration outside the channel and limiting the growth of nanowire in unwanted areas. By increasing the

negative gate voltage magnitude to −10 V, the nanowire growth is further restricted inside the nanochannel, as shown in Figure 4.4.2 (d). Under this condition, the redistribution of Pd^{2+} ions is able to limit most of Pd distribute inside the channel and the growth of nanowire is extremely confined by the gate electric field. The nanowire becomes very uniform with a diameter less than 100 nm (91 nm), indicating a complete growth confinement of nanowire by the nanochannel and gate voltage. By comparing results in Figures 4.4.2 (a)–(d), it is clear that applying a negative gate voltage greatly improves nanowire growth, with a −10 V successfully limiting the nanowire growth to within the nanochannel.

A statistical study further proves the effect of gate-assisted growth, in which nanowire growth with 0 and −10 V gate voltages under five different growth conditions has been compared. As shown in Figure 4.4.3, three kinds of channels with the same width (100 nm) but different lengths (6.5, 4 and 3.5 μm) are used under three different growth currents (50, 30 and 10 nA) [46]. In all five cases the diameter of the nanowire is reduced and the growth time is shortened by applying a −10 V gate voltage. These results show that the nanowire size reduction matches the effect of negative gate voltage as observed in previous experiments. The time shrinkage indicates a faster deposition process due to the higher Pd^{2+} ion concentration along the bottom of the channel resulting from the gate electric field.

Gate-assisted growth offers a simple way to achieve sub-50 nm growth of both metal and conducting polymer nanowires via electrochemical deposition in a controlled manner. As shown in Figures 4.4.4 (a) and (b), two SEM images demonstrate successful Pd nanowire growth with a less than 50 nm diameter [46]. The first nanowire (figure 4.4.4 (a)) is grown under a 40 nA growth current and −10 V gate voltage within a 6 μm long and 50 nm wide nanochannel. This nanowire has a diameter ranging from 49 to 44 nm and a measured resistance of 8.93 kΩ. The
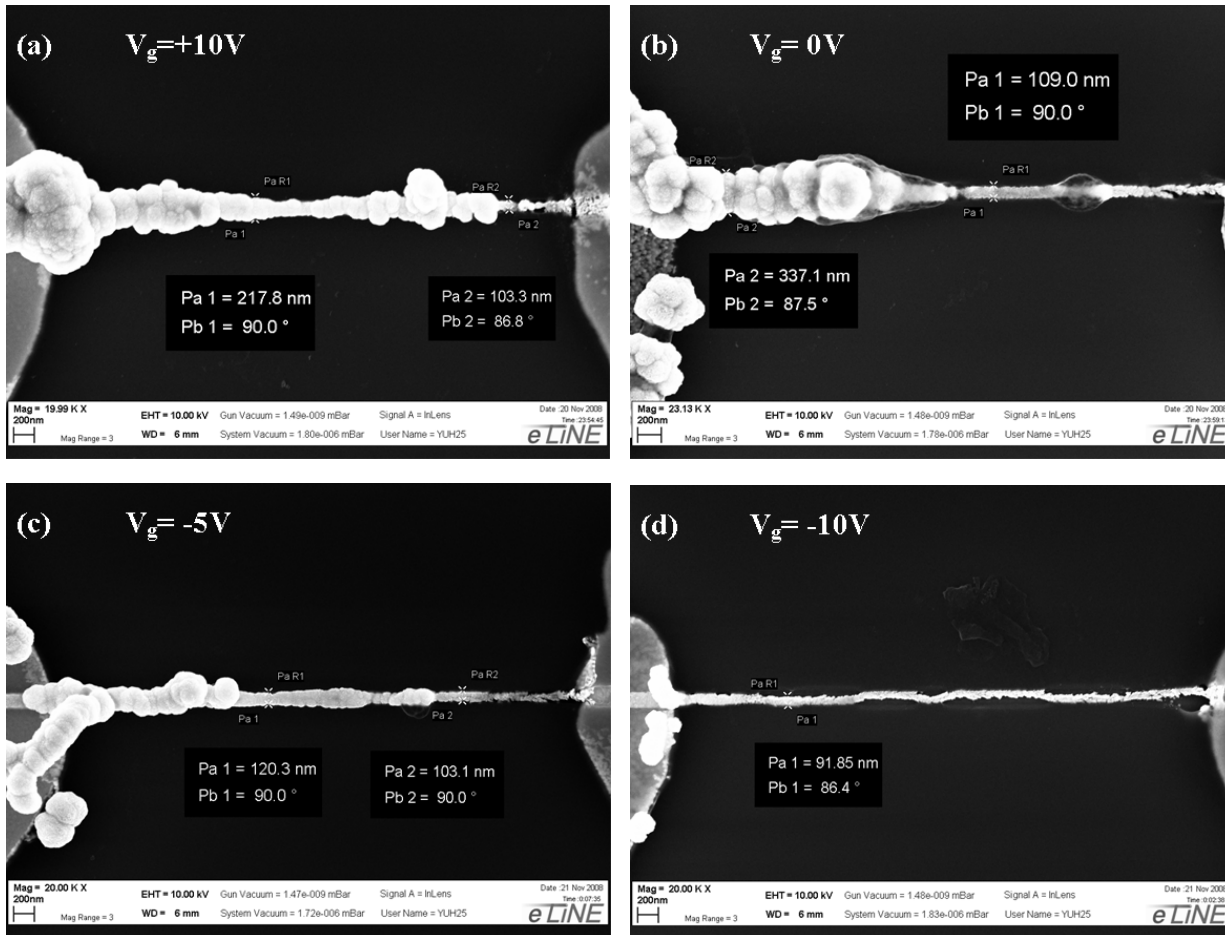
Figure 4.4.2 SEM images of Pd nanowires grown using gate voltages of (a) 10 V, (b) 0 V, (c) −5 V and (d) −10 V during electrochemical deposition under 50 nA growth current inside 6.5 μm long and 100 nm wide nanochannels. [46]
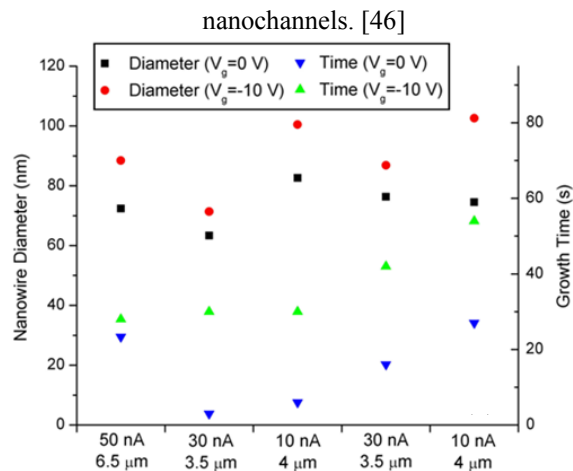
Figure 4.4.3 Statistical comparison between Pd nanowire non-gate growth and gate-assisted growth with −10 V gate voltage under five different growth conditions. Two parameters were compared: nanowire diameter and growth time. [46]
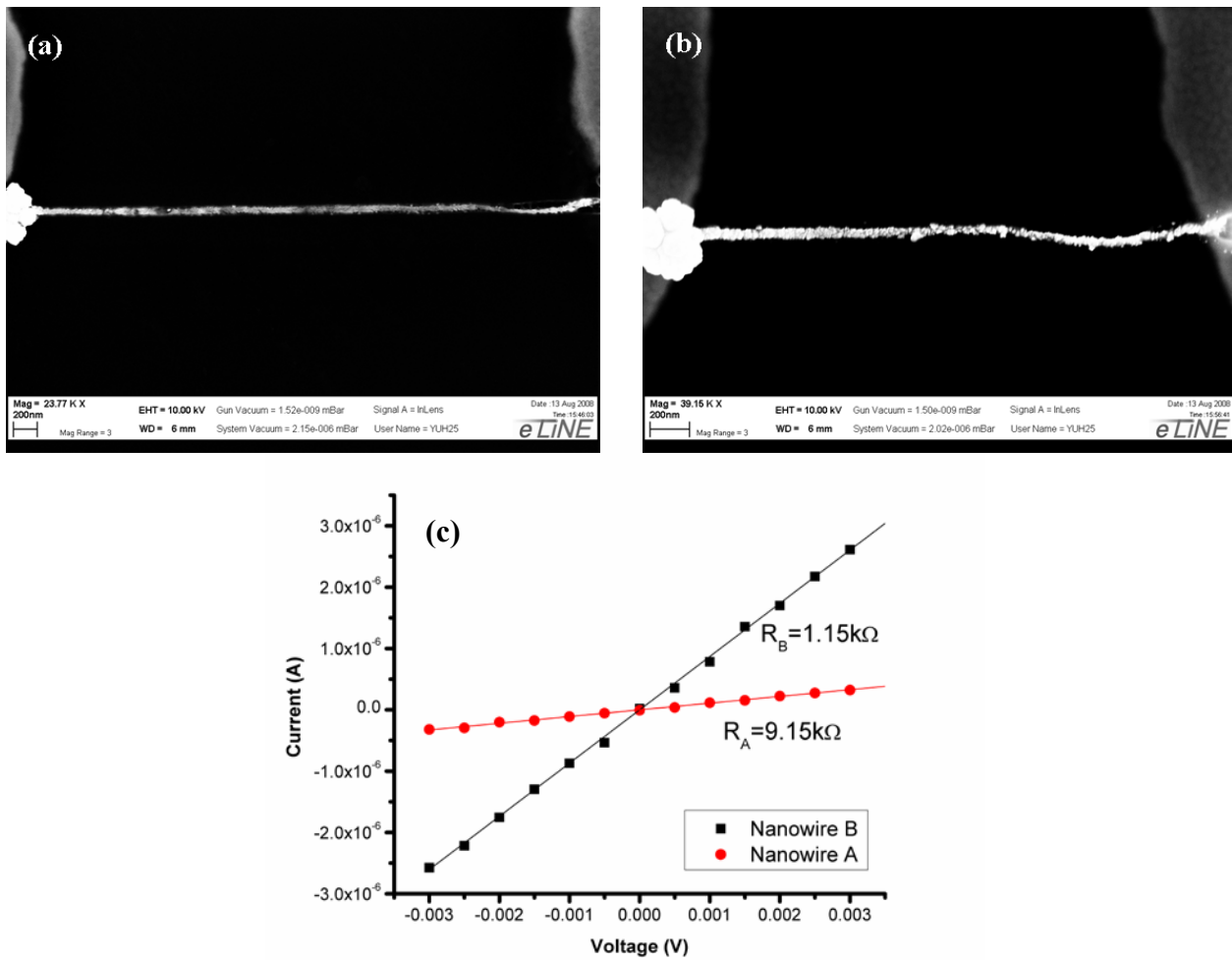
Figure 4.4.4 SEM images of Pd nanowires grown inside a 50 nm channel with (a) 49–44 nm and (b) 50–42

nm diameters. (c) *I–V* curves for the nanowires of (a) and (b). [46]

second nanowire (Figure 4.4.4 (b)) is grown under 10 nA growth current and −10 V gate voltage within a 3 μm long and 50 nm wide nanochannel with a diameter ranging from 50 to 42 nm. This nanowire has a measured resistance of 1.15 kΩ. For both cases, the nanowire growth is very well confined within 50 nm wide channels with very uniform structures, which serves as a solid proof of the effectiveness of gate-assisted growth in fabricating nanowires in the sub-50 nm range. As shown in figure 4.4.4 (c), the linear I −V curves of the previously mentioned nanowires indicate ohmic contact between the nanowire and gold electrodes, increasing their potential use as electronic devices.

In order to demonstrate the feasibility of super-thin single polymer nanowires for the nanowires' potential use in biosensors, we also applied our gate-assisted electrochemical deposition method to PPy nanowire growth [46]. Figures 4.4.5 (a) and (b) present two SEM images of PPy single nanowires that are grown inside 50 nm PMMA channels. The first nanowire (Figure 4.4.5 (a)) has a length of 3 μm and a diameter of 53–51 nm with a measured resistance as 471 Ω (Figure 4.4.5 (c)) by a two-probe measurement. The second nanowire (Figure 4.4.5 (b)) is 1.6 μm long and 46~47 nm wide with a resistance measured as 562 Ω (Figure 4.4.5 (c)). Both nanowires show good uniformity in structure and are very well confined inside the nanochannel. Similar to Pd nanowires, the PPy nanowires have a good ohmic contact with gold electrodes, which can be proved by their linear I −V curves. Gate-assisted growth thus enables an effective synthesis in CP single nanowires with sub-50 nm diameters.
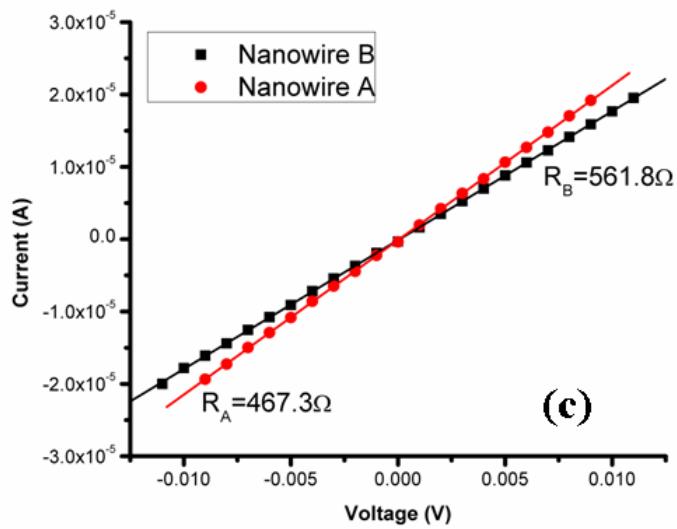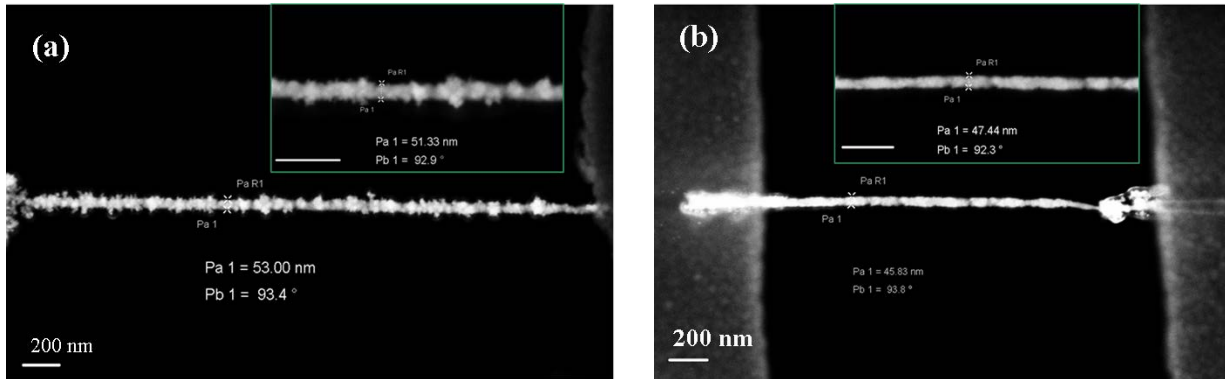
Figure 4.4.5 SEM images of single PPy nanowires grown within a 50 nm PMMA channel with (a) 51–53

nm and (b) 46–47 nm diameters. The scale bars represent 200 nm. The insets are magnified images of the same

nanowire. (c) *I–V* curves for the nanowires of (a) and (b). [46]

4.5 ELECTRONIC NOSE USING PD/PANI/PPY/ZNO SENSOR ARRAY

4.5.1 Introduction and motivation

As previously demonstrated, Pd and PPy nanowire are successfully fabricated via gate-assisted growth with less than 100 nm diameters and good uni formity. A Pd single nanowire based hydrogen sensor has also been approved. These findings open the possibility of applying single nanowires made of different materials to form a nanowire array. This sensor array is expected to detect and identify multiple target gases. A sensor device used in this way is also called an "electronic nose".

An electronic nose (e-nose), a device that mimics the olfaction system in mammals, is expected to paly a role in a wide range of areas, such as d isease diagnosis, food quality inspection, gas chromatography, and spacecraft atmospheric monitoring [51-54]. These applications require that the e-nose not only detects an individual target at extremely low concentration (down to ppm or lower), but that it also identifies the exact chemicals of the target with high selectivity. In order to improve sensitivity, previous studies employed nanomaterials, such as nanowires and nanoparticles, as e-nose building blocks because of their high surface area to volume ratio and superior sensitivity for detecting volatile organic compounds (VOCs) and toxic industrial gases (e.g., NO_2 and CO) [55-56]. Target identification, on the other hand, was mainly realized by including an array of different sensor elements in the e-nose device [57-58].

Despite previous success in gas detection, the reported e-noses suffer from several drawbacks that seriously limit their applications. First, the active materials in the sensor elements are usually limited to one type of material, such as metal oxides and conducting polymers [56-58]. This limitation restricts the variety of sensible target molecules of the e-nose, thus rendering

it a device only applicable to specific targets. In addition, the similar chemical properties among the active sensing materials in the array can result in a less than optimal selectivity. For example, a reported e-nose based on only conducting polymer nanowires failed to clearly identify two of the target VOCs [59]. Second, the previous nano e-nose studies were satisfied with distinguishable smell prints but did not attempt to verify the sensor performance in real situations or explore the possibility of concentration estimation. For advanced cases, such as spacecraft monitoring, where both the compositions and the concentrations of targets need to be identified, the ability of the e-nose to estimate the target concentration becomes extremely important.

This section presents the incorporation of an array of different single nanowires on a single chip. The array includes four different materials: palladium (Pd), polypyrrole (PPy), polyaniline (PANI), and zinc oxide (ZnO). These four materials were chosen because they represent distinct material types: metal, conducting polymer, and metal oxide. An e-nose with three different material types is demonstrated for the first time. This e-nose is used to detect four target gases with distinct properties, including carbon monoxide (CO, a very common household toxic gas), hydrogen (H_2, an important potential energy source), methanol (CH_3OH, a representative VOC), and nitrogen oxide (NO_2, a common oxidizing gas and a common industrial toxic gas). Well-separated smell prints are built up with the help of principal component analysis (PCA) for all targets, even at extremely low (sub-ppm) concentrations. Finally, a blind experiment where the e-nose is exposed to four gas injections with unknown compositions and concentrations is conducted to verify the identification ability. It is demonstrated that by comparing each injected target with the original smell prints the target composition can be successfully identified and, moreover, approximated with the accuracy determined by calibration (data collected to build up smell prints) PCA data point density.

Therefore, the sensor array synthesis and systematic analysis performed here not only provide a feasible way of incorporating nanowires from different material types on a single chip, but also point out a way for target concentration estimation through PCA.

4.5.2 Device fabrication

As mentioned previously in Chapter 2, t he fabrication of each single nanowire is done via electrochemical deposition. In section 4.1, the successful growth of single Pd and PPy nanowires was demonstrated. In order to incorporate four single nanowires on the same chip, we need to achieve the following objectives:

1. The selective growth of different nanowire material in certain area on t he chip has to be realized. This can be done by pl acing a drop of different electrolyte solutions for different nanowire materials on the specific channel. Once the nanowire growth is complete, the nanowire is only grown inside the designated nanochannel. The electrolyte solutions for these four nanowires are:

Palladium: $Pd(NH_2)_2(NO_2)_2$ (diaminepalladium nitrite) (10 g/L) and $NH_4SO_3NH_2$ (ammonia sulfamate) (100 g/L);

Polypyrrole: NaCl (0.2 mol/L) and pyrrole (98%, 0.1 mol/L);

Polyaniline: HCl (0.1 mol/L) and aniline (98%, 0.01 mol/L);

Zinc Oxide: $ZnCl_2$ (0.005 mol/L) and NaCl (0.015 mol/L) for Zinc nanowire, and $Zn(NO_3)_2 \cdot 6H_2O$ (0.05 mol/L) and HTMA (0.05 mol/L) for hydrothermal process;

2. The growth of one nanowire should not affect the growth of other nanowires. This is especially important when the nanowire growth temperatures are very different. Polymer nanowires, such as PPy and PANI, cannot withstand high temperature because they have

70

relatively low melting points (160~166°C for PPy and 160~170°C for PANI). Thus the highest growth temperature should not exceed 160°C. The growth of Pd, PANI and PPy are all done under room temperature, and the hydrothermal process for ZnO is done at a temperature less than 100°C. These guarantee that the growth of the four nanowire materials can be done on the same chip.
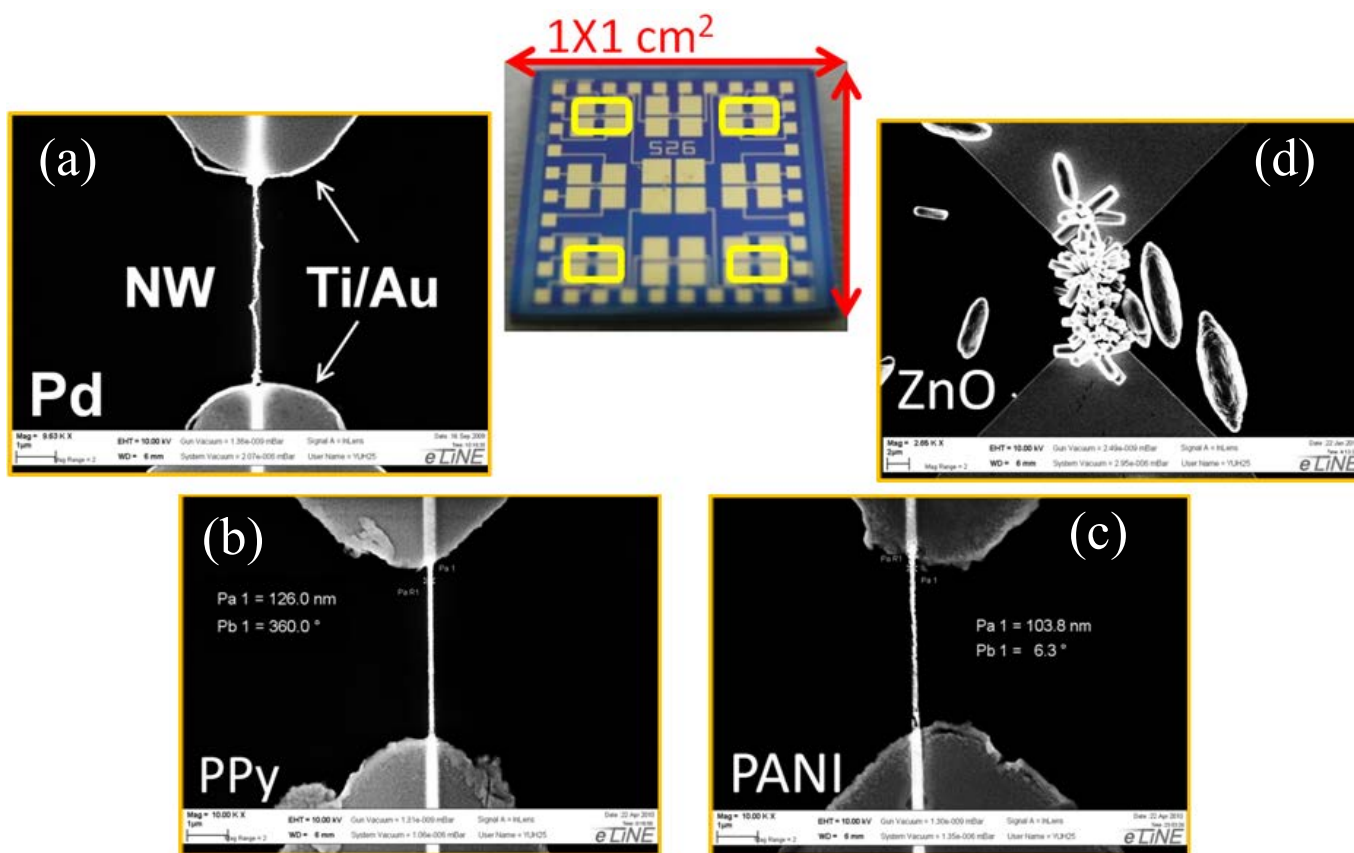
Figure 4.5.1 A Pd/PPy/PANI/ZnO nanowire array fabricated on a same chip (center) with a size of 1 by 1 cm^2. SEM images of (a) Pd, (b) PPy, (c) PANI, and (d) ZnO are also shown.

3. The different nanowires on a chip have to be incorporated into a device so that they can simultaneously function as a sensor array. This can be done by using wirebonder to connect all the nanowires to an external electrical system. This system includes a power supply that can provide constant voltage onto each nanowire, and a data collection system equipped with a multiplexer that can collect multi-channel signals at the same time.

As a result, a device containing four different single nanowires on a same chip is shown in Figure 4.5.1. The chip has an overall size of 1 cm by 1 cm; there is a total of 16 pairs of working electrode pairs and 4 gate electrodes. Each nanochannel has a diameter of 100 nm and a length of 5 μm. Four nanowires are grown one after another on top of the channel one after another. The SEM images of different nanowires, including Pd, PANI, PPy and ZnO are also shown in Figure 4.5.1 (a) to (d). We can clearly see that, the shape of Pd, PANI and PPy nanowires are very similar. These nanowires are very well confined in the nanochannel and the diameters for Pd, PPy and PANI are 128 nm, 126 nm and 104 nm, respectively, which demonstrates the effectiveness of electrochemical deposition in fabricating these nanowires in an array. However, the shape of the ZnO nanostructure is more complicated. It is shown in Figure 4.5.1 (d) that the nanostructure is not a single nanowire, but rather a bundle of many small nanorods, and each nanorod has a diameter of around 500 nm. This is due to the hydrothermal process we used for ZnO nanowire.

The growth of ZnO is quite different from those of Pd, PPy and PANI, mainly because of the fact that ZnO growth is much less affected by the electric field than the crystalline structure of the substrate or seed layer. In order to achieve both fast growth and good contact between the ZnO nanostructure and the electrodes, a novel two-step process was invented to fabricate the ZnO nanostructure. First, a Zn nanowire is grown inside the nanochannel using the

electrochemical deposition method. This is easily done because the conductivity of Zn is much larger than that of ZnO. The growth direction is much more easily controlled by the electric field similar to the cases of Pd and conducting polymers. Then, this as-grown Zn nanowire is placed inside a hydrothermal solution containing $Zn(NO_3)_2 \cdot 6H_2O$ (0.05 mol/L) and HTMA (0.05 mol/L). After the solution is heated up to 90°C, the Zn grown inside the nanochannel will start to oxidize and act as the seed for ZnO nanostructure growth. After a 30 minute hydrothermal process, a nanostructure shown in Figure 4.5.1 (d) can be achieved with a good contact with both electrodes.

4.5.3 Nanowire Characterization

In order to characterize the fabricated nanowires on the chip we conducted both electrical measurements and material characterizations. To prove that the nanowires have good contacts with the electrodes, we did I-V measurements for each of the four nanowires using semiconductor analyzer.

Representative electrical measurements for Pd, PPy and PANI nanowires are shown in Figure 4.5.2. The I-V measurement data shown in Figure 4.5.2 (a) present that all these three single nanowires have linear I-V curves, demonstrating a good ohmic contact with Au electrode for each of the single nanowires. Figure 4.5.2 (b) presents the resistance distribution for the three single nanowires. Each resistance distribution is obtained from more than 20 nanowires and the error bar represents the standard deviation from these nanowires. The average resistances for Pd, PPy and PANI are 1.04 kΩ, 1.35 kΩ and 1.38 kΩ, respectively. It is clearly shown that the resistances fall into the narrow range of over 700 Ω to about 1.8 kΩ for all three nanowires, which demonstrates that the electrical properties of these nanowires are very stable.
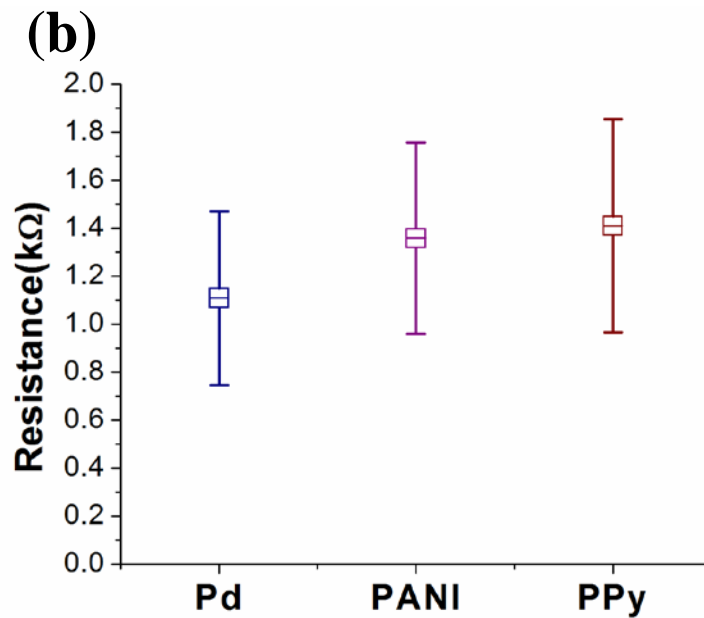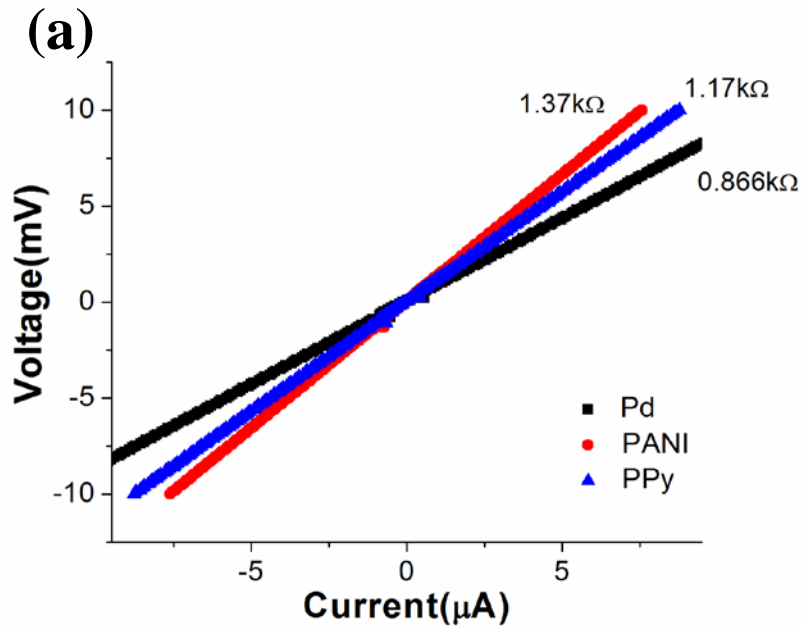
Figure 4.5.2 Electrical measurements for Pd, PPy and PANI nanowires. (a) A representative I-V sweeping measurement for Pd, PPy and PANI single nanowires. (b) Converted resistance distribution for Pd, PPy and PANI single nanowires. Each data is collected from more than 20 nanowires and the error bar represents the standard deviation from these nanowires.
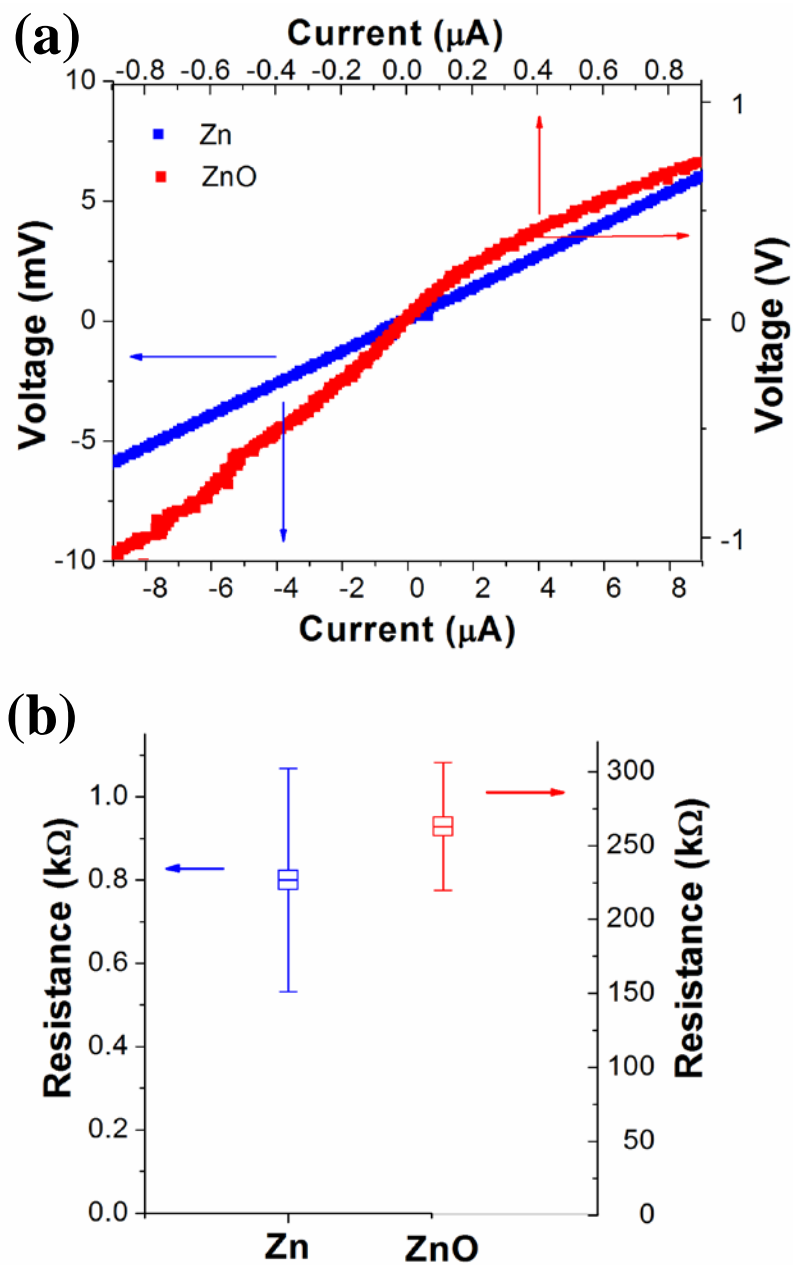
Figure 4.5.3 Electrical measurements for ZnO nanowire before and after hydrothermal process. (a) A representative I-V sweeping measurement for ZnO single nanowire before and after hydrothermal process. (b) Converted resistance distribution for ZnO single nanowires before and after hydrothermal process. The data before hydrothermal process is collected from 12 nanowires and the data after hydrothermal process is collected from 4 nanowires. The error bar represents the standard deviation from these nanowires.

The I-V measurement for ZnO nanowire before and after hydrothermal process is shown in Figure 4.5.3. It can be seen from Figure 4.5.3 (a) that the nanowire shows a linear I-V curve before hydrothermal process, in accordance with the fact that Zn nanowire is fabricated and a good ohmic contact is formed between the nanowire and the Au electrodes. After the hydrothermal process, the nanowire becomes oxidized and the ohmic contact disappears, as shown in Figure 4.5.3 (a). The I-V curve for ZnO nanowire shows clear Schottky effect and the contact between the ZnO nanowire and the Au electrodes is no longer ohmic. The resistance distribution plot shown in Figure 4.5.3 (b) can also demonstrate the change. Before oxidation, the Zn nanowire shows an average resistance of 820 Ω, and the resistance falls into the range of around 500 Ω to 1.1 kΩ. This is very similar to the metallic Pd nanowire and highly conductive PPy and PANI nanowire, and proves that Zn nanowire before hydrothermal process has a metallic behavior. After oxidation, the resistance becomes much higher with an average value of 260 kΩ. This is shows that the metallic conduction of Zn nanowire is replaced by the semiconducting conduction of ZnO nanowire.

In all, the electrical measurements for each of the four nanowires show that:

(1) The Pd, PPy and PANI single nanowires have good ohmic contacts with the Au electrodes;

(2) The Zn/ZnO nanowire shows ohmic contact with Au electrode before oxidation and schottky contact after oxidation via hydrothermal process;

(3) The resistance distribution of more than 20 nanowires shows that the resistance of different nanowires are very stable, providing a good foundation for their usage in sensors.

In addition to the electrical measurements, material characterizations of each of the four nanowires are conducted to study the composition and structure of these single nanowires. Energy Dispersive X-ray Diffraction Spectroscopy (EDX) and Raman Spectroscopy were

employed to carry out the characterizations. EDX are used to study the composition of Pd and ZnO nanowires. Representative spectrum from the fabricated Pd and ZnO nanowires are shown in Figure 4.5.4 (a) and (b). The EDX spectrum for Pd nanowire illustrated in Figure 4.5.4 (a)
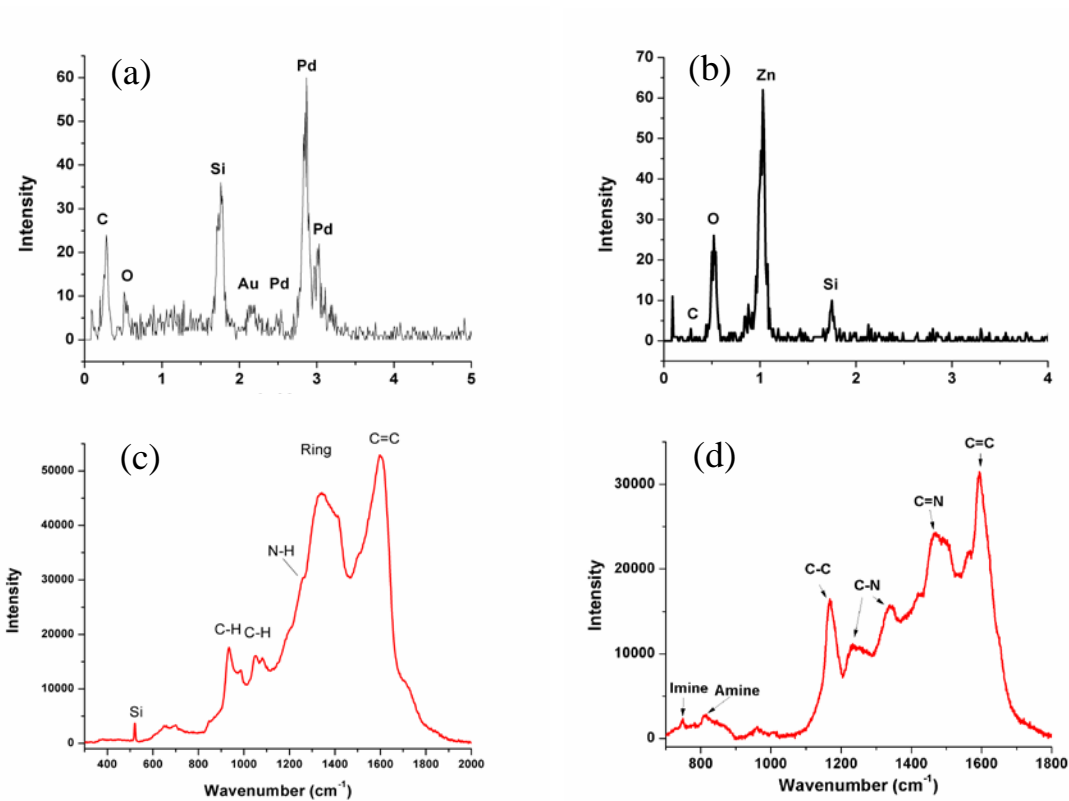
Figure 4.5.4 EDX and Raman spectrums for the single nanowires. (a) An EDX spectrum for Pd single nanowire; (b) An EDX spectrum of ZnO nanowire; (c) A Raman spectrum for PPy single nanowire; (d) A Raman spectrum for PANI single nanowire.

shows a clear Pd peak, demonstrating the successful formation of Pd. The strong peak of Si comes from the Si substrate on which the nanowire sits. Because of the its trivial intensity, the peak of O is possibly picked up from either the thin SiO_2 insulation layer beneath the nanowire or a weak oxidation layer of the Pd surface at ambient environment. The C peak possibly comes from the remained PMMA after acetone cleaning. For ZnO nanostructure, its EDX spectrum illustrated in Figure 4.5.4 (b) shows clear Zn and O peaks, demonstrating the successful formation of ZnO. Si and C peaks are observed due to the same reasons mentioned above for Pd nanowire, but their intensities are much smaller than those of Zn and O peaks. One thing to be mentioned is that although O peak can be picked up from SiO_2 substrate, the intensity of this O peak seen in ZnO spectrum is roughly 2.5 times that of the Si peak. In contrast, the intensity of O peak seen in Pd is only around 30% of that from the Si peak. On the other hand, the intensity ratio of O peak and Zn peak from ZnO nanostructure is around 38%, which is in good accordance with the ratio of 30% to 40% from previous reports on ZnO thin films and nanostructures. Clearly, such O peak intensity mainly results from ZnO nanostructure and this EDX spectrum proves the successful formation of ZnO nanostructure.

For characterization of PPy and PANI, EDX is not adequate because: 1) conducting polymers have very similar elemental composition (C, H, N, etc) and the information provided EDX cannot definitely prove the formation of either PPy or PANI; and 2) the formation of PPy and PANI should be demonstrated via the successful formation of certain characteristic bonds. As a result, Raman spectroscopy (Raman) is utilized to verify the formation of PPy and PANI. As illustrated in Figure 4.5.4 (c), the noticeable Raman peaks of PPy single nanowire are 521 cm^{-1} (Si), 938 cm^{-1}, 988 cm^{-1}, 1048 cm^{-1}, 1082 cm^{-1}, 1250 cm^{-1}, 1330 cm^{-1}, 1410 cm^{-1}, 1598 cm^{-1}, which match the characteristic peaks of PPy in literature at Si (521), C-H out of plane

deformation (939), ring deformation (984), C-H in plane deformation (1050/1080), N-H in plane deformation (1260), ring stretching (1326/1407), and C=C backbone (1600) modes. The existence of ring deformation, ring stretching and N-H deformation peaks convincingly prove the formation of PPy. As shown in Figure 4.5.4 (d), the Raman peaks of PANI single nanowire are 750 cm^{-1}, 820 cm^{-1}, 1168 cm^{-1}, 1227 cm^{-1}, 1340 cm^{-1}, 1425 cm^{-1}, 1475 cm^{-1}, 1565 cm^{-1}, 1595 cm^{-1}, which also match the characteristic peaks for PANI described in literatures at imine deformation (750), amine (N-H) deformation (823), C-H in plane bending (1165), C-N stretching (1225/1329), C-C stretching (1425), C=N stretching (1470), C-C stretching (1560), and C=C stretching (1595) modes. The existence of C=N stretching peaks and amine deformation peak shows that the PANI nanowire has an oxidized state of most likely Emeraldine and it is neither fully reduced state (where C=N bond does not exist) nor fully oxidized state (where N-H bond does not exist). In all, with the help of EDX and Raman we not only confirmed the elemental compositions of Pd and ZnO nanowires but also demonstrated the existence of the characteristic bonds in PPy and PANI nanowires. These results proved the successful formation of Pd, PPy, PANI and ZnO nanowires using electrochemical deposition.

4.5.4 Sensing signals from individual nanowires

In order to study the sensing performances from each of the four nanowires, we conducted careful experiments on the sensing performances of each nanowire. Four different target gases (hydrogen (H_2), methanol (CH_3OH), carbon monoxide (CO) as well as nitrogen dioxide (NO_2)) are chosen. H_2 and CO are both very common reducing gas and are very important elements in a large variety of applications. H_2 is emerging as a new energy source and the early detection H_2 at low concentrations is very critical for security purposes. CO is a common house toxic gas

which can cause severe damages to human body. However, human noses are not sensitive to CO and a external device is required to monitor the concentration of CO at all times. In addition, H_2 and CO are important gases in fuel cell industry and a successful monitoring of these gases can help determine the performance of the fuel cells. NO_2 is a very common toxic environmental gas and air pollutant usually seen in the waste gases from factories and automobiles. It is important to monitor the concentration of NO_2 in the environment to prevent its damage on human health. Moreover, it is also a gas closely related with explosives such as TNT and DNT that can generate NO_2 via UV light absorption. A successful detection of NO_2 can be utilized for the detection of explosives. Methanol is one of the most common volatile organic compounds (VOCs). VOCs are usually similar in both chemical and physical properties and they are very important in a large number of applications. The concentration of different VOCs can be used to indicate the food quality, such as wine and dairy products. Recently, an increasing amount of focus has been placed on disease diagnosis based on the concentrations of different VOCs in human breath. A successful detection of VOCs is extremely important for developing portable medical devices that can accurately identify certain cancers with non-invasive diagnosis method. In a word, these target gases are very important in a wide range of applications and the successful detection and identification of them are of great interest. Moreover, these gases represent a number of different chemical groups with distinct properties. Thus an e-nose that is able to detect all of the targets demonstrates a wide sensing range and it has potential uses in multiple areas.

In order to study the detailed concentration related sensing performances from the nanowires, each of the four target gases was tested at different concentrations spanning over two orders of magnitude. Hydrogen is tested under concentrations from 10% to 94 ppm; methanol is tested under concentrations from 14.4% to 1400 ppm; carbon monoxide is tested under

concentrations from 2000 ppm to 182 ppm; and nitrogen dioxide is detected under concentrations from 10 ppm to 625 ppb. Carbon monoxide and nitrogen dioxide concentrations are chosen at very low levels because their toxic levels are very low (sub-ppm for NO_2). One thing to be noticed is that each gas is tested in multiple cycles including consecutive gas injection and gas purging so that complete sensing performances of each sensor are demonstrated. In order to cover the sensing performances from different sensors, the real time signals from each single nanowires, including Pd, PPy, PANI and ZnO, are presented and discussed in detail in the following parts.

Figure 4.5.5 presents the real-time responses from Pd single nanowires to four target gases at different concentrations. In each plot, the x-axis represents time (s) and the y-axis represents the relative sensitivity ($\Delta R/R_0 \times 100\%$). In figure 4.5.5 (a), the Pd single nanowire showed median responses towards CH_3OH from 7.2% to 0.55% and the detection limit is 0.55%. In figure 4.5.5 (b), the Pd single nanowire showed no observable signals when the CO gas were turned on and off with concentrations of 2000 ppm and 667 ppm. In figure 4.5.5 (c), the Pd single nanowire showed clear and large responses toward H_2 at concentrations from 10% to as low as 94 ppm. The detection limit for H_2 is 94 ppm. In figure 4.5.5 (d), the Pd single nanowire showed no observable singles for NO2 at concentrations of 10 ppm and 3.3 ppm. In summary, the real time sensing signals from a Pd single nanowire proves that Pd has high sensitivity to H2 and median sensitivity to CH_3OH, while showing no responses to CO and NO_2. This is in accordance with the fact that Pd is very selective for H_2 detection and not sensitive to other target gases.

Figure 4.5.6 presents the real-time responses from PPy single nanowire to the four target gases at different concentrations. In figure 4.5.6 (a), PPy showed large responses to CH3OH at
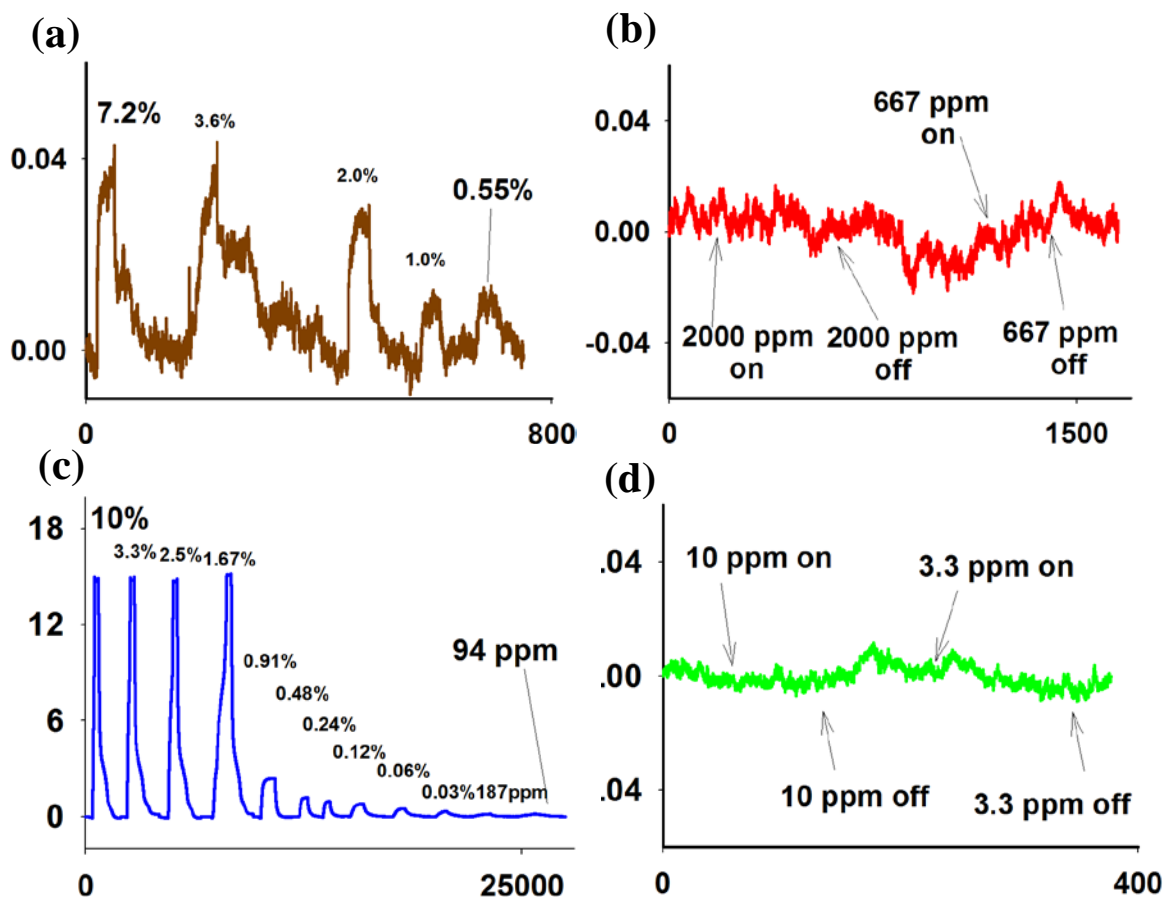
Figure 4.5.5 Real time sensing signals from Pd single nanowire for the detection of (a) CH_3OH, (b) CO, (c) H_2 and (d) NO_2. The x-axis represents time (s), and the y-axis represents relative sensitivity ($\Delta R/R0 \times 100\%$). The sensing concentrations for CH_3OH are 7.2%, 3.6%, 2.0%, 1.0% and 0.55%; the sensing concentrations for CO are 2000 ppm and 667 ppm; the sensing concentrations for H_2 are 10%, 3.3%, 2.5%, 1.67%, 0.91%, 0.48%, 0.24%, 0.12%, 0.06%, 0.03%, 187 ppm and 94 ppm; the sensing concentrations for NO_2 are 10 ppm and 3.3 ppm.

82

concentrations from 7.2% to 0.55%, and the detection limit was 0.55%. Figure 4.5.6 (b) shows that PPy has a small sensitivity for CO at concentrations from 2000 ppm to 182 ppm. In figure 4.5.6 (c), PPy also showed a median sensitivity for H_2 at concentrations from 10% to 0.48%. However, PPy showed a relatively large response for NO_2 at concentrations from 10 ppm to 625 ppb, as illustrated in figure 4.5.6 (d). The detection limit is 625 ppb. It is clearly seen in figure 4.5.6 that PPy showed larger sensitivities in CH_3OH and NO_2 and median sensitivities to CO and H_2. This is in good accordance with the fact that conducting polymers are good sensors for VOCs and reductive/oxidative gases.

Similar to PPy, PANI single nanowire also showed responses to four target gases, as shown in figure 4.5.7. PANI single nanowire also showed very large responses to CH_3OH at concentrations from 14.4% to 1400 ppm, as shown in figure 4.5.7 (a). Figure 4.5.7 (b) to (d) show that PANI single nanowire had relatively small responses to CO, H_2 and NO_2. It is clearly shown that, PANI and PPy both showed considerable responses to all four target gases, which is probably due to the fact that PPy and PANI are both conducting polymers and they have similar chemical properties. However, they also showed differences in their sensing performances toward these four gases. PPy showed a higher sensitivity to CO and NO_2 while PANI showed higher sensitivity to CH_3OH.

Figure 4.5.8 presents the real-time sensing responses from ZnO for all four target gases. As illustrated in figure 4.5.8 (a), ZnO showed a very large response toward CH3OH at concentrations from 14.4% to 0.55%. ZnO single nanowire also showed very high sensing responses to the rest three target gases, as shown in figure 4.5.8 (b) to (d). Comparing with the other sensor materials, ZnO nanowire showed much higher sensing response for all four target gases: the relative sensitivity from ZnO were two to three orders of magnitude higher than the
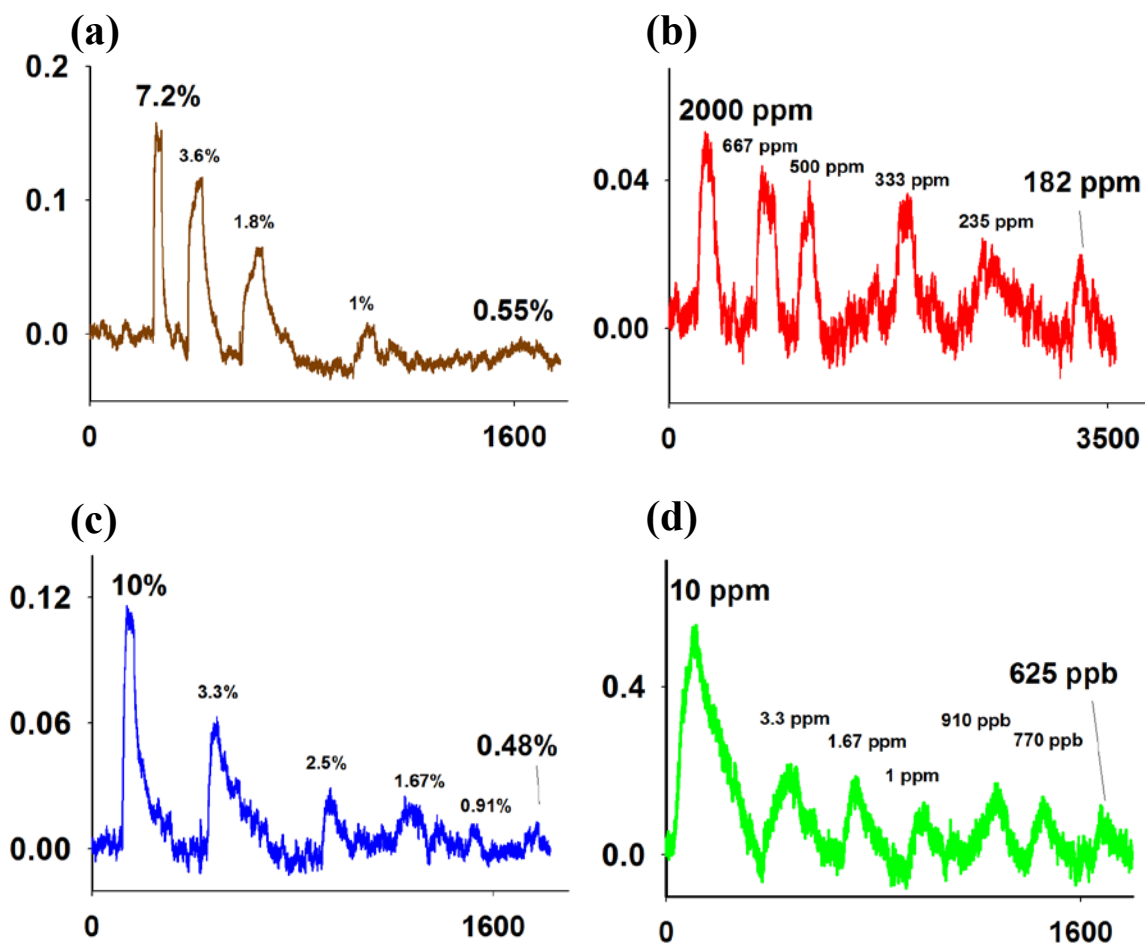
Figure 4.5.6 Real time sensing signals from PPy single nanowire for the detection of (a) CH_3OH, (b) CO, (c) H_2 and (d) NO_2. The x-axis represents time (s), and the y-axis represents relative sensitivity ($\Delta R/R0 \times 100\%$). The sensing concentrations for CH_3OH are 7.2%, 3.6%, 2.0%, 1.0% and 0.55%; the sensing concentrations for CO are 2000 ppm, 667 ppm, 500 ppm, 333 ppm, 235 ppm and 182 ppm; the sensing concentrations for H_2 are 10%, 3.3%, 2.5%, 1.67%, 0.91%, and 0.48%; the sensing concentrations for NO_2 are 10 ppm, 3.3 ppm, 1.67 ppm, 1 ppm, 910 ppb, 770 ppb, and 625 ppb.
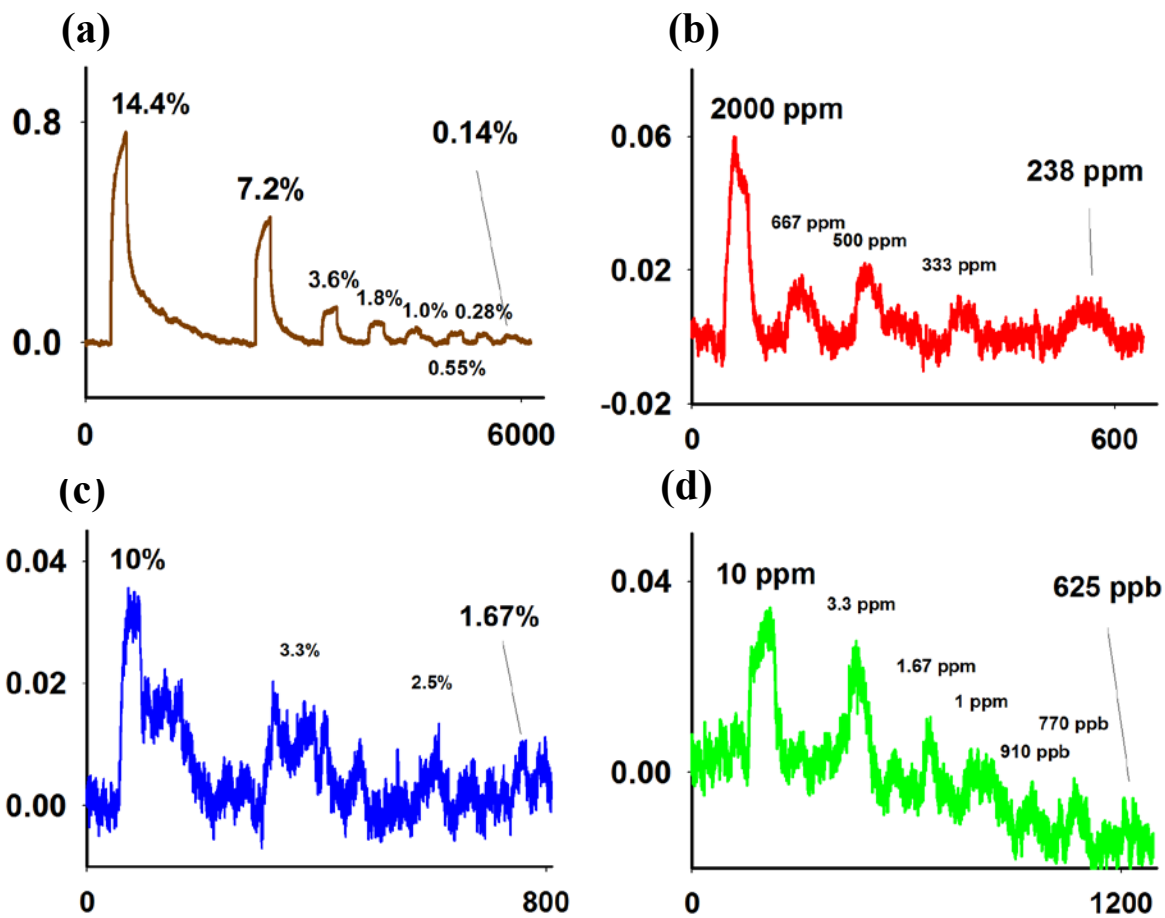
Figure 4.5.7 Real time sensing signals from PANI single nanowire for the detection of (a) CH_3OH, (b) CO, (c) H_2 and (d) NO_2. The x-axis represents time (s), and the y-axis represents relative sensitivity ($\Delta R/R0 \times 100\%$). The sensing concentrations for CH_3OH are 14.4%, 7.2%, 3.6%, 2.0%, 1.0% , 0.55%, 0.28% and 1400 ppm; the sensing concentrations for CO are 2000 ppm, 667 ppm, 500 ppm, 333 ppm, 235 ppm; the sensing concentrations for H_2 are 10%, 3.3%, 2.5%, and 1.67%; the sensing concentrations for NO_2 are 10 ppm, 3.3 ppm, 1.67 ppm, 1 ppm, 910 ppb, 770 ppb, and 625 ppb.
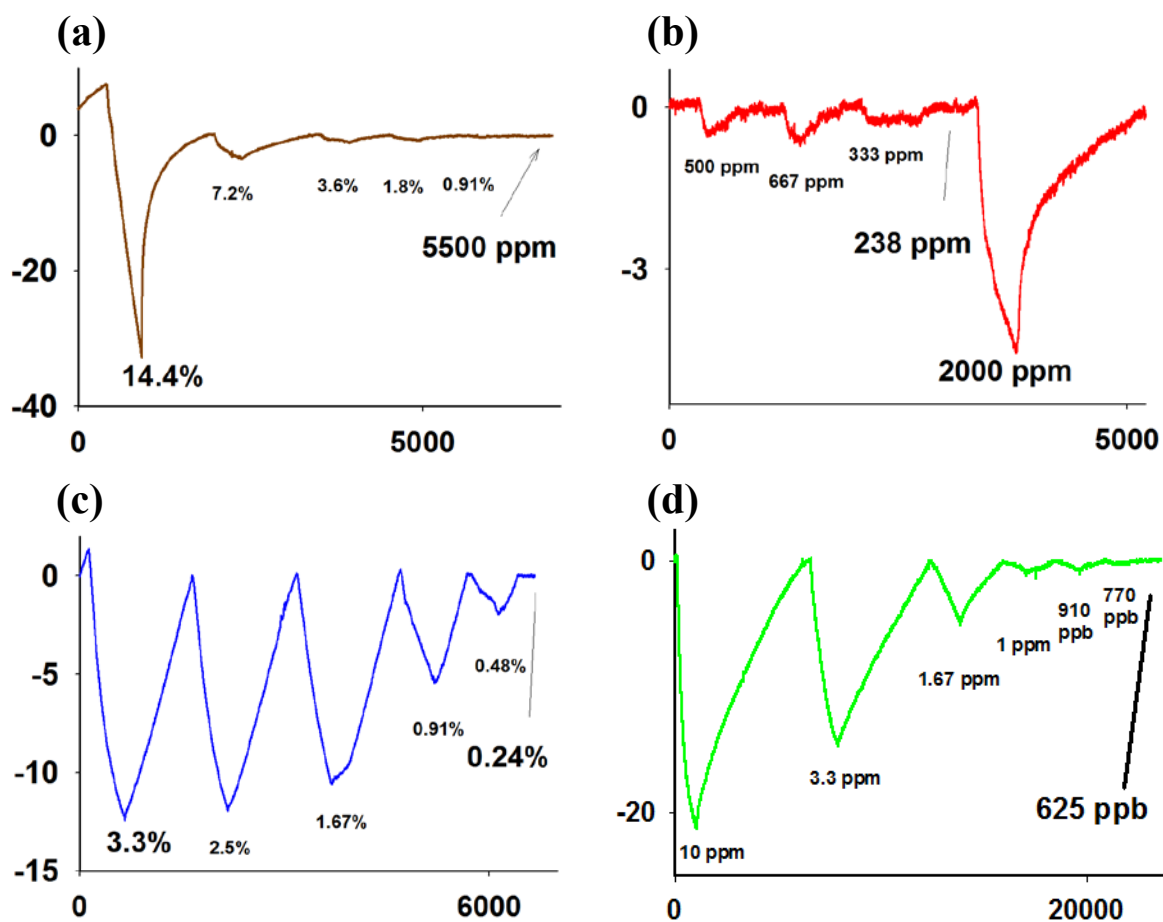
Figure 4.5.8 Real time sensing signals from ZnO single nanowire for the detection of (a) CH$_3$OH, (b) CO, (c) H$_2$ and (d) NO$_2$. The x-axis represents time (s), and the y-axis represents relative sensitivity (ΔR/R0$\times$100%). The sensing concentrations for CH$_3$OH are 14.4%, 7.2%, 3.6%, 2.0%, 1.0%, 0.55%; the sensing concentrations for CO are 500 ppm, 667 ppm, 333 ppm, 238 ppm and 2000 ppm; the sensing concentrations for H$_2$ are 3.3%, 2.5%, 1.67%, 0.91%, 0.48% and 0.24%; the sensing concentrations for NO$_2$ are 3.3 ppm, 1.67 ppm, 1 ppm, 910 ppb, 770 ppb, and 625 ppb.

86

relative sensitivities from the other materials at the same concentrations. On the other hand, ZnO had a much longer response time during the gas detection (almost 10 times longer than other materials in NO_2 detections). As a metal oxide, ZnO is widely reported because of its great sensing responses to a wide range of target gases. The morphology of ZnO nanostructures could be the reason of the much longer response time. ZnO nanostructure has a much larger radial dimension than Pd, PPy and PANI single nanowires, it would take much longer for gas molecules to penetrate through the bulk of ZnO nanosensor and generate saturated sensing signals during gas detection. Similarly, the gas molecules need much longer time to diffuse out of the ZnO nanostructure during the purging cycle to refresh the ZnO nanosensor. Both of these two processes account for the much longer response time for the ZnO nanosensor.

In summary, the sensing signals from the four nanowires were discussed in detail. For each target gas, the sensing performances were evaluated through multiple gas injection and gas purging cycles with different gas concentrations. The sensing performances collected in this way not only showed the sensing responses for different concentrations, building up relationships between gas concentrations and relative sensitivities, but also gave insights for the sensor's reproducibility, stability and response time. Moreover, each sensing signals are collected from one set of sensors, that is, the sensing signals from one nanowire material for four different target gases at different concentrations were collected from a same single nanowire made of that material. Thus the sensing performances were the real-time sensing performances from a real sensor array, taking the aging of the nanowire material and possible interactions between different target gases into account. The sensing performances collected in this way can be used to represent the real application situation to the largest extent.

From these sensing signals, we can make the following conclusions: a) the relative sensitivities from the sensors are directly related to the target concentrations. These signals thus provide a means of building the relationship between gas concentration and electrical signals (relative sensitivity in this case); b) this sensor array is able to detect and sense the four target gases even at very low concentrations, although different materials showed different detection limits. This lays a solid foundation for an e-nose that has a wide range of sensing targets with low detection limits; c) the sensing behaviors from different sensor materials are different, due to the distinct chemical properties possessed by these materials. This provides the ability for the e-nose to discriminate different target gases at different concentrations.

As mentioned above, the sensing signals from one set of sensor array are important to build up the relationships between target gas concentrations and relative sensitivities. It is equally important to look into the repeatability of the signals and the reproducibility of the devices. In order to illustrate the repeatability of the signals, two sensing signals from Pd single nanowire and PPy single nanowire are presented in figure 4.5.9.

In figure 4.5.9 (a), a real-time sensing response from a single Pd nanowire for consecutive detection of H_2 with concentrations of 3.3%, 2.0% and 10% is shown. This Pd sensor had a positive sensing mechanism with a decreased resistance when exposed to hydrogen. In order to study the repeatability of the sensing signal, each concentration was repeated three times before the introduction of new concentration gases. It is clearly shown that the sensor response was very consistent for a certain concentration. This proves that the gas sensor has a very good repeatability when gases with different concentrations are introduced. However, this result does not show whether changing one target gas to another could affect the repeatability.
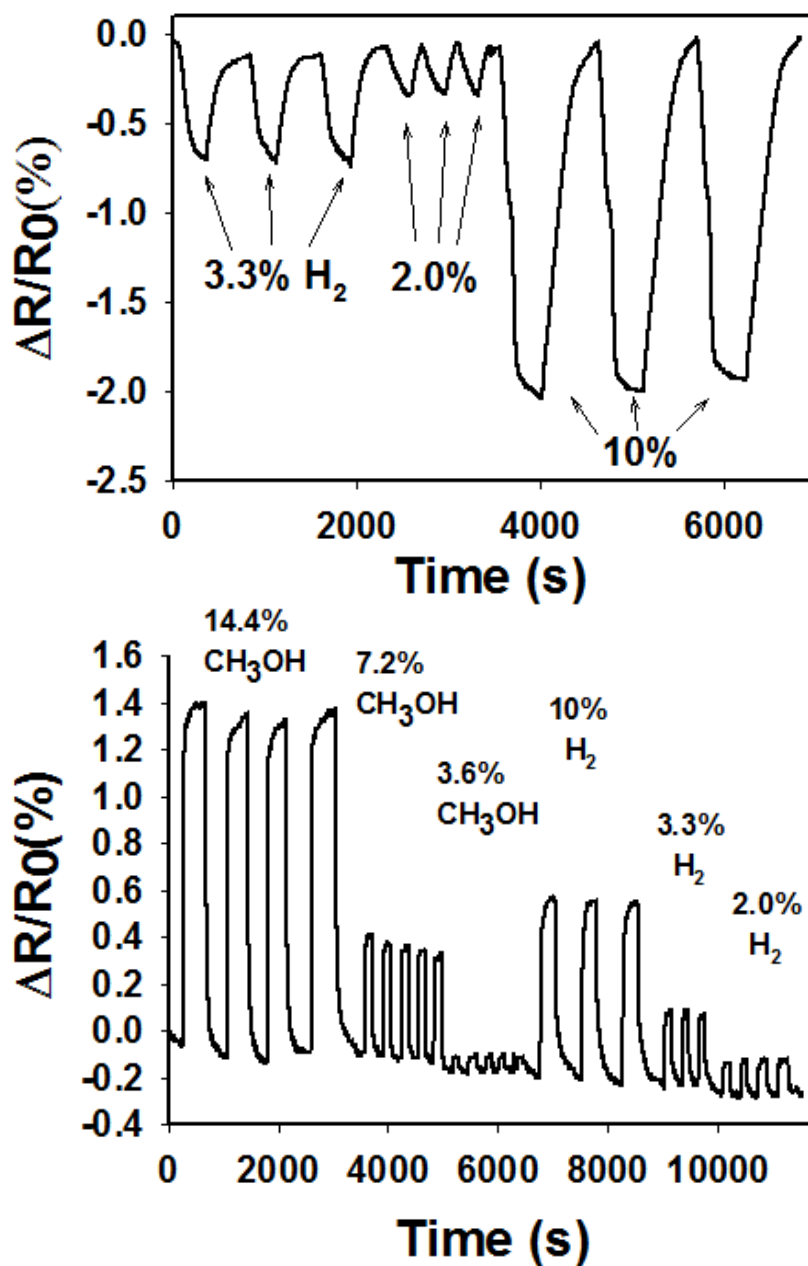
Figure 4.5.9 Repeatability tests for Pd and PPy single nanowire sensors. (a) Real time sensing signals from a Pd single nanowire for the detection of H_2 at concentrations of 3.3%, 2.0% and 10%. Each concentration was repeated for three cycles to demonstrate the repeatability of the sensor. (b) Real time sensing signals from a PPy single nanowire for the detection of CH_3OH and H_2 at concentrations of 14.4% (CH_3OH), 7.2% (CH_3OH), 3.6% (CH_3OH), 10% (H_2), 3.3% (H_2) and 2.0% (H_2). Each concentration was repeated three to five cycles to demonstrate the repeatability of the sensor.
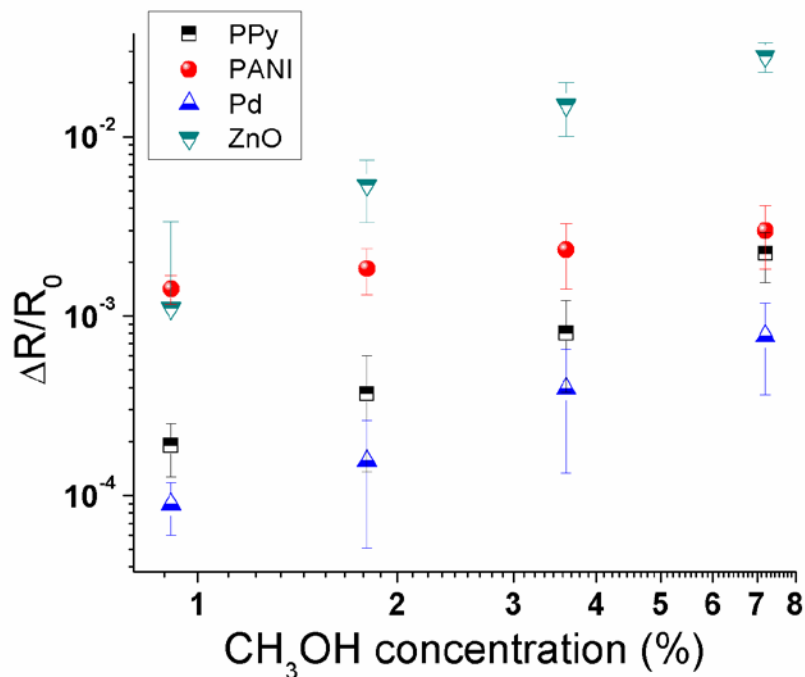
Figure 4.5.10 Reproducibility tests for Pd, PANI, PPy and ZnO single nanowire sensors from a total of 12 devices. The relative sensitivities from all four gas sensors over CH3OH at four different concentrations (7.2%, 3.6%, 1.8% and 0.91%) are collected and plotted in a log format. Three devices for each kind of sensor were tested to demonstrate the reproducibility between different devices. The points represent the mean value of relative sensitivities between three different devices and the error bars represent the standard deviations.

In order to study the effect of switching target gases on the repeatability of the gas sensor, an experiment was conducted in which a gas sensor was exposed to two different target gases and each gas had different concentrations. The repeatability was studies by repeating each gas concentration for 3 to 5 times consecutively. The real-time sensing response is shown in figure 4.5.9 (b). In this sensing signal, a PPy single nanowire was used as the gas sensor and the two target gases were methanol and hydrogen. We can clearly see in the signal that the repeatability for methanol before changing the target gas was very good, and the response amplitude was very consistent for up to 5 cycles for the same concentrations. After switching the target gas from

methanol to hydrogen, the gas sensor still showed very consistent sensing response to different hydrogen concentrations in 3 sensing cycles at each concentration. This result demonstrates that the gas sensor was able to keep its repeatability after switching the target gases. In summary, the gas sensors presented very good repeatability in the repeatability tests, providing a reliable foundation for their usage in real applications.

In addition to the tests for repeatability between different sensing cycles during the gas sensing, experiments were also conducted to study the reproducibility between different gas sensors. As shown in figure 4.5.10, a total of 12 devices from four different sensors (Pd, PPy, PANI and ZnO) were tested for their responses over methanol at four different concentrations. The relative sensitivities from these devices were extracted from the real time sensing signals and plotted in a logarithmic format against the gas concentration statistically, giving information on the reproducibility of the sensors. On the one hand, difference in sensing responses exists between one device and another. This is resulted from the deviation of nanowire structures and dimensions during the fabrication process. The difference in sensor device integration could also affect the sensor performances. On the other hand, the standard deviations in different devices from one sensor material is small compared with the difference between sensor devices made from different materials. The relative sensitivities from different sensor materials are well separated from each other. These results show that although deviation exists between individual devices from the same sensor material, the reproducibility of the sensors is good enough to separate sensing performances from different sensor materials, providing a reliable performance from individual sensor devices.

In summary, both the repeatability and the reproducibility of the devices were tested. The demonstrated great consistency in repeatability from Pd and PPy nanowire sensors and the

91

presented reproducibility among different individual sensors made from Pd, PANI, PPy and ZnO not only prove the reliability of the sensor performances, but also lay down a solid foundation for the devices to be used in real e-nose applications.

4.5.5 Gas sensing mechanisms from each nanowire element

As mentioned in Chapter 2, different nanowire element has its own unique chemical/physical properties. In order to have an in-depth understanding of the sensing signals, it is very beneficial to gain some insights on the sensing mechanisms from each nanowire element. The proposed sensing mechanisms from different sensor elements will be discussed in the following sections:

1) Pd single nanowire

The sensing mechanism of Pd has been well discussed in earlier sections. As mentioned in Chapter 2.1, the sensing of Pd single nanowire mainly relies on two effects: a. the resistivity change (increase 180%) when Pd switches from α phase ($PdH_{0.1}$) to β phase ($PdH_{0.7}$); and b. the volume expansion ($\sim 10\%$) due to the lattice expansion when Pd switches from α phase to β phase. Effect a will result in a total increase of nanowire resistance when exposed to hydrogen, while effect b will decrease the nanowire resistance by increasing the contact area between adjacent nanowire grains. As discussed in Chapter 4.3, both of these effect could happen in Pd nanowire sensing and the final sensing signal depends on the actual nanowire structure.

The sensing of Pd over CH_3OH is mainly due to the catalytic effect of Pd on the decomposition of CH_3OH, as shown in equation 2.1. This decomposition of CH_3OH generates a small amount of H_2, resulting in a sensing signal in Pd similar to H_2. However, this sensing response is much smaller than that from direct H_2 sensing. As for the sensing of NO_2 and CO, Pd has almost no response towards them even at very high concentrations. Although Pd can act as the catalyst for

the NO_2 and CO in reactions shown in equation 2.2 and equation 2.3, Pd is not sensitive to either the original reactants (NO_2 and CO) or the resulting products (NO, O, and CO_2). As a result, Pd has no specific reactions with NO_2 and CO that could generate electrical signals, thus no response can be found in NO_2 and CO sensing.

2) PPy and PANI single nanowire

As described in Chapter 2.2.3, the sensing mechanisms for PPy and PANI nanowires are closely related to the protonation (the addition of H^+) and deprotonation (the removal of H^+) processes when strong acidic gases or basic gases exist. In this case, none of the target gases is strong acidic or basic. Thus the sensing mechanisms for the target gases are more relevant to the electron donation and extraction (or reduction/oxidation) processes. Because both PANI and PPy are considered to be p-type after electrochemical deposition, reducing gases such as H_2 and CO can act as electron donor and reduce the charge carrier concentration in the conducting polymer backbone and introduce an increased resistance. Take hydrogen sensing via PPy single nanowire for example. Hydrogen is a strong electron donor and is capable of reducing PPy backbone to a less oxidized state according to the following reaction:

$$(4.5.1)$$
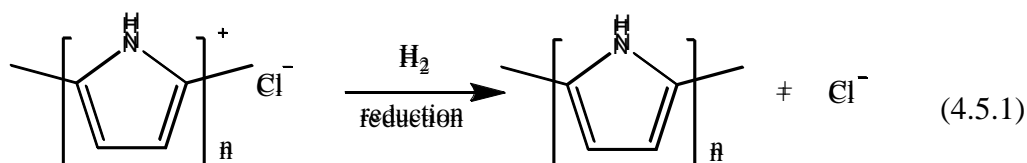
As indicated by this reaction, the entrapped charge carrier density (the hole generated by H^+) is reduced when H_2 is present. This results in a reduction in conductance or an increase of resistance in PPy. The sensing of CO is very similar to the sensing of H_2, and we see the resistance increases in both PPy and PANI single nanowire when H_2 or CO is introduced.

For methanol, on one hand it is a weak reducing gas or a weak electron donor that could initiate a reaction (4.5.1) and reduce the conductance of PPy. On the other hand, the adsorption of CH_3OH into the polymer matrix tends to introduce heterogeneous electron hopping conduction between PPy and PANI chains, which would further decrease the conductance of the whole structure. Since CH_3OH is only weak reducing gas and its molecule size is much larger than both H_2 and CO, the effect of CH_3OH on inter-chain hopping is believed to be the main reason for the decrease of resistance in PPy and PANI, as described in [59].

The case for NO_2 is a little more complicated. Nitrogen dioxide is a well known oxidizing gas which, upon exposure in a reducing environment with adequate catalyst, can be easily reduced to NO or even N_2O and O_2. The strong oxidation of NO_2 could extract electrons from PPy and PANI structure and causes hole accumulation in the polymer matrix, which effectively reduces the resistance of the polymer given that both PPy and PANI show p-type conduction. From the view of electron extraction a resistance reduction is expected in both PPy and PANI when NO_2 is introduced. The decreased resistance signal has been reported by various groups [60]. However, in our tests we saw consistent resistance increase signals in both PPy and PANI nanowires when NO_2 was introduced. We attribute this phenomenon to an over oxidation occurred in PPy and PANI nanowire. It is well recognized that an oxidation of PPy caused by O_2 could change its structure and result in the formation of an amide (C=O) derivative of PPy. Appearance of C—O and C=O groups is also possible when PPy is exposed in O_2 for more than an hour [36]. The fact that NO_2 is a stronger oxidizing agent than O_2 together with that O_2 could be generated during NO_2 reduction indicates an inevitable over oxidation during the NO_2 exposure. The conductance change of PPy upon exposure to NO_2 is thus a combined effect of polymer oxidation which results in a conductance increase and a structural degradation caused

by over oxidation which could results in a severe conductance decrease. This degradation effect by NO_2 can be best illustrated by figure 4.5.11, in which a PPy nanowire showed degraded sensing signals when it was exposed to multiple cycles of NO_2. We did not see such severe sensing degradation in the signals shown in figure 4.5.6 (d) and figure 4.5.7 (d), mostly because the NO_2 concentration was much lower.
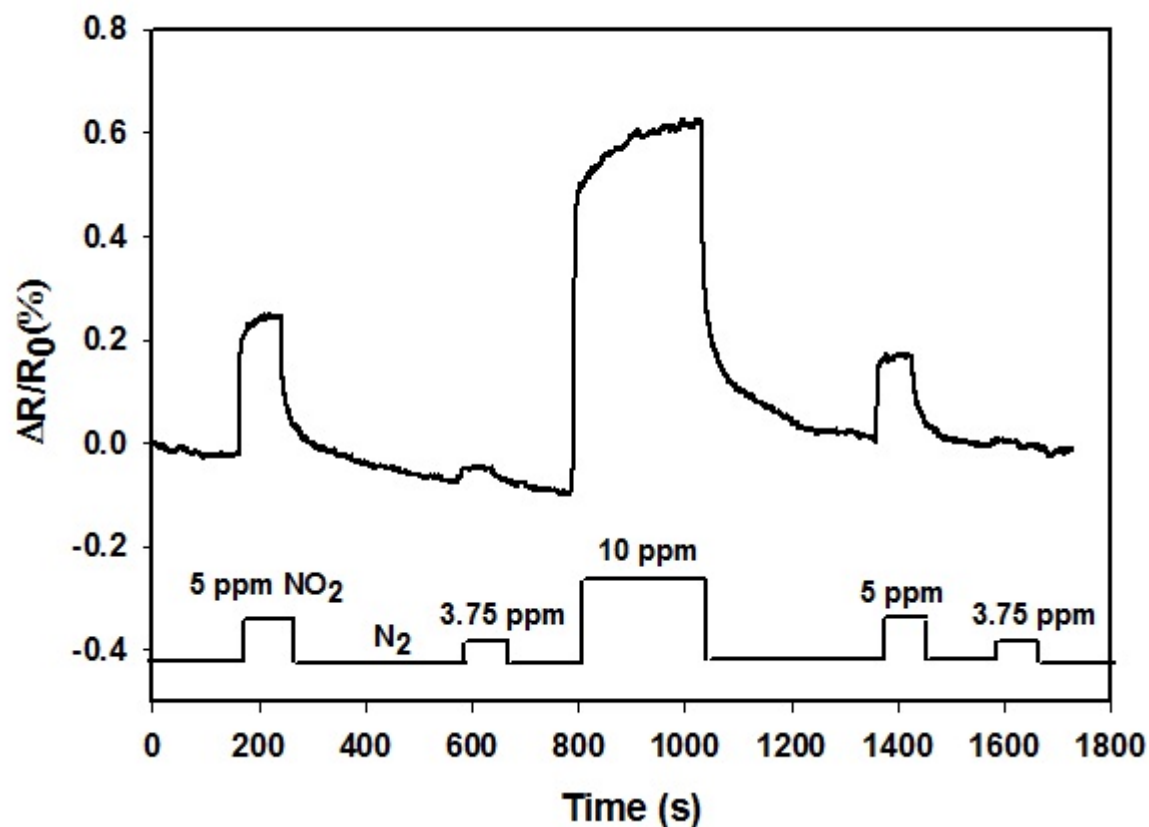
Figure 4.5.11 A real time sensing signal from a PPy single nanowire when exposed to NO_2 at concentrations of 5 ppm, 3.75 ppm, 10 ppm, 5 ppm and 3.75 ppm. The degradation in sensing response is clearly seen by comparing the responses at 5 ppm and 3.75 ppm before and after 10 ppm NO_2 injection.

3) ZnO single nanowire

As described in Chapter 2.3.1, the sensing mechanism of ZnO nanowire is closely related to the surface charge carrier density change (charge accumulation and depletion). Clearly stated and demonstrated in Chapter 2.3.1, electron donating gases, such as H_2, CH_3OH and CO are able to bind with the free oxygen agents in the surface of ZnO nanowire, and free electrons are released in this process. On the other hand, strong oxidizing gas, such as NO_2, is able to bind with oxygen vacancies and extract electrons from the surface of ZnO nanowire. Since ZnO nanowire is considered as n-type semiconductor, the majority charge carrier is electrons. Thus H_2, CH_3OH and CO are able to increase the charge carrier concentration on the ZnO surface and decrease the resistance of the nanowire. As expected, the sensing signals from 4.5.8 (a) to (c) present resistance decrease when ZnO nanowire is exposed to H_2, CH_3OH and CO. However, the sensing signal for NO_2 showed a resistance decrease instead of a resistance increase, which does not agree with the expected sensing mechanism.

Although this discrepancy is against the commonly accepted space-charge model for n-type ZnO, similar abnormal sensing behavior has been reported elsewhere in hydrothermally fabricated ZnO nanotube structures, as described in [61]. This phenomenon could be related to an N-P transition when ZnO is exposed to NO_2. Thus a possible explanation can be provided: The conductivity of ZnO depends on the concentrations of both electrons and holes. Normally as-synthesized ZnO is considered as a n-type semiconductor in which electron concentration is higher than hole concentration. Due to the exposure to NO_2, oxygen is absorbed on ZnO surface and the following reaction could happen:

$$[V_o^{2+}] + 1/2\ O_2 = O_o + 2h^+$$

96

Pd Nanowire for Hydrogen Sensing

Pd nanowire

hydrogen

Phase Change: Pd to PdH$_{0.7}$
R increase

Volume Expansion
R decrease

Conducting Polymer Nanowire

Chemical

Physical

Electron extraction   **Electron donation**

R decrease   R increase

X^- | $-e^-$

X^-

R decrease   R increase

$\Downarrow$ $+H^+$

Increased hopping length due to VOC absorption

R increase

Electron acceptors:
O2, NO2, I2, etc.

Electron donors:
NH3, HCl, H2, etc.

Typical for VOCs

Carrier Accumulation

ZnO Nanowire

Carrier Depletion

N type

R decrease

R increase

Electron donors:
NH3, HCl, H2, etc.

Electron acceptors:
O2, NO2, I2, etc.

Figure 4.5.12 Illustrations of sensing mechanisms for Pd, PPy, PANI, and ZnO nanowires.

97

where V_o^{2+} represents an oxygen vacancy site and O_o represents an oxygen atom in oxygen site, as described in both [61] and [62]. The effect of this process could be either depleting the charge carrier (if electron concentration is higher than holes, such as in normal cases) on ZnO surface or inverting the charge carrier type and cause an increase of total carrier density. If the latter case happens, a decreased instead of increased resistance will be observed when ZnO is exposed to NO_2. However, more research is still needed to prove this mechanism and investigate the onset conditions of N-P transition. In summary, the sensing behavior found in our sensing results can be explained by a possible N-P transition happened in our ZnO nanostructure.

To sum up, an illustration describing the gas sensing mechanisms for all four nanowires toward the target gases is provided in figure 4.5.12.

4.5.6   PCA analysis and smell prints

The concentration-dependent responses shown in figure 4.5.5 to 4.5.8 not only provide insights into the sensing mechanisms for different sensor materials, but they also set up a relationship between signals and target concentrations, forming a basis for concentration estimation. To clearly express the concentration-signal relationship and to provide direct comparisons among nanowires, we plot the RSs against target concentrations in a logarithmic form in figure 4.5.13. Each plot corresponds to one target gas, and the RSs of the four nanowires are compared. In figure 4.5.13 (a), for CH_3OH, the ZnO nanowire shows the highest sensitivity, and the Pd nanowire shows the lowest sensitivity. The PANI nanowire shows a slightly higher sensitivity than the PPy nanowire. In figure 4.5.13 (b), for CO, the ZnO nanowire shows the highest sensitivity, and the PPy nanowire shows a slightly higher sensitivity than the PANI nanowire. The Pd nanowire has almost no sensitivity to CO. In figure 4.5.13 (c), for NO_2, the ZnO
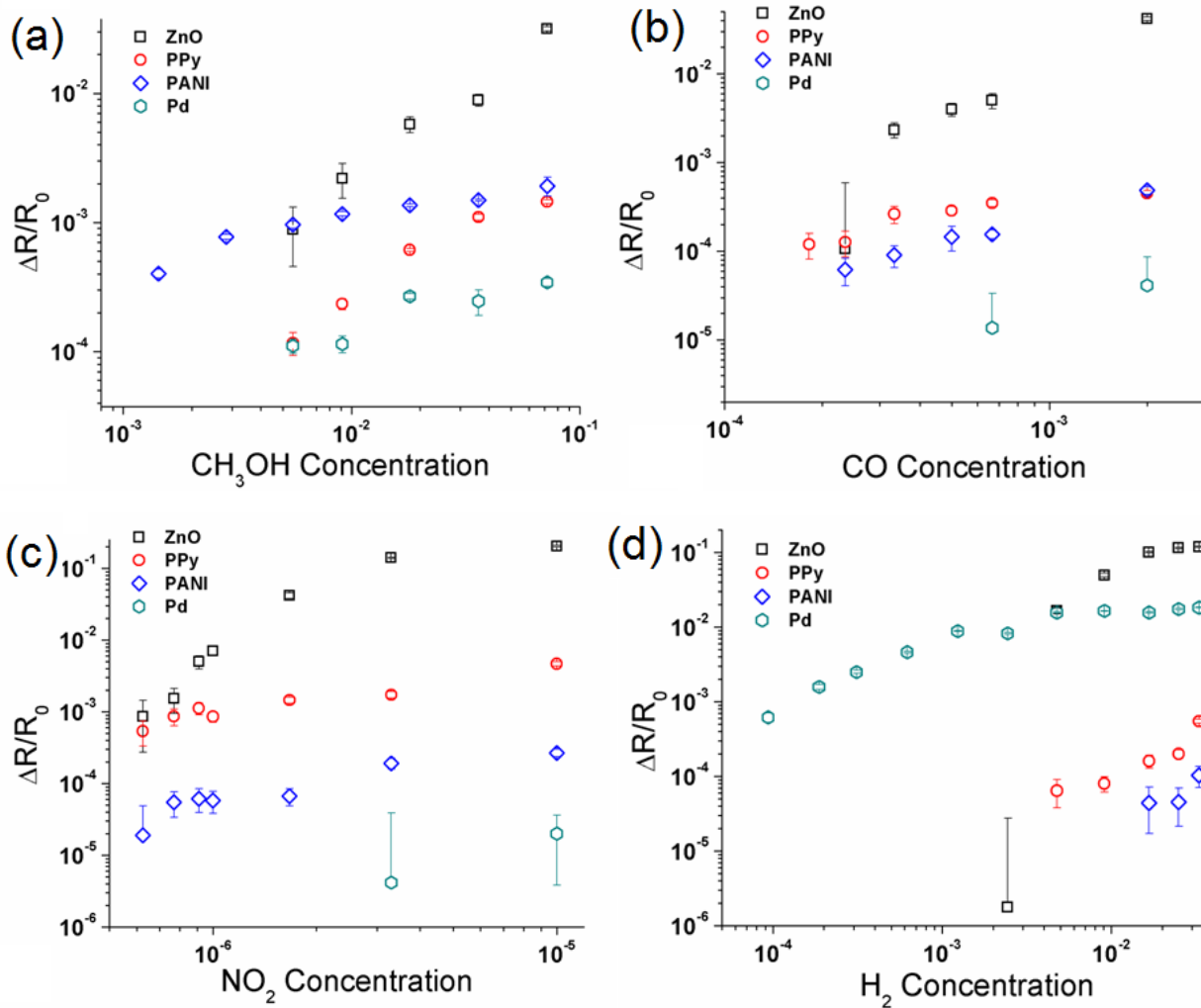
Figure 4.5.13 Relationships between gas concentrations and relative sensitivities. Summarized data for (a) CH_3OH, (b) CO, (c) NO_2, and (d) H_2 with regard to different nanowire materials presented in four plots. In each plot, the x axis is gas concentration in logarithmic form, and the y axis represents RS in logarithmic form (lg(RS)). Due to the minus sign of the RSs from ZnO, ZnO's relative sensitivities are plotted using absolute values. The error bars represent the standard deviation due to the noise level in each gas injection.

nanowire has the highest sensitivity, and PPy has a higher sensitivity than the PANI nanowire. The Pd nanowire has almost no sensitivity to NO_2. In Figure 4.5.13 (d), in the case of H_2, the Pd and ZnO nanowires show similar sensitivity at high H_2 concentration. But the Pd nanowire remains highly sensitive to H_2 even at a very low H_2 concentration, while the sensitivity of the ZnO nanowire decreases sharply when the H_2 concentration drops. Neither the PPy nor PANI nanowire shows a high sensitivity to H_2. This again proves that the Pd nanowire is the most efficient in H_2 detection. By comparing the four plots, we can conclude the following: (i) This nanowire array is able to detect all four targets with the lowest detectable concentrations of CH_3OH, CO, H_2, and NO_2 at 1400 ppm, 182 ppm, 94 ppm, and 625 ppb, respectively; (ii) The sensing patterns of the different nanowires are completely different; and (iii) The sensing signals are closely related to the target concentration. The disparity in the sensing patterns is utilized for gas identification, and the concentration-dependent sensing response provides the basis for target concentration estimation. It is also noticed that the PPy and PANI nanowires have similar sensing patterns as compared to the ZnO and Pd nanowires. This infers that, although chemically different, nanowires from the same material type possess similar sensing patterns, which suggests that adding different material types to the nanowire array could increase selectivity.

Although figure 4.5.13 gives a clear indication that based on these sensing data all four different target gases can be differentiated, it is hard to do so just by looking at the data plots because there are four dimensions of data points coming from four different nanowire materials. As described in Chapter 2.4.3, PCA is a very popular and effective way to compress high dimensional data sets and to display the original data sets using two-dimensional (2D) or three-dimensional (3D) plots without losing much information. In this work, the saturated RS values of each nanowire when exposed to a certain target under certain concentration are extracted, and the

four nanowires constitute four data sets with each data point denoting the saturated RS for a target at a concentration. PCA is then used to reduce the four-dimensional data to a 2D or 3D space whose bases are the first two or three principal components with the largest variances. This new data matrix can be plotted in a 2D or 3D format for easy visualization, with each data point representing a certain gas under a certain concentration, and its coordinates are the scores with regard to each Principal component (PC).

Figure 4.5.14 (a) and figure 4.5.14 (b) illustrate the 2D and 3D PCA plots from this four-nanowire sensor array. The variances possessed by the principal components are 45.2% (PC1), 32.3% (PC2), 20.8% (PC3), and 1.70% (PC4). In figure 4.5.14 (a), data points from NO_2, CO, H_2, and CH_3OH distribute separately and stretching to different directions on the plot. One thing needs clarification is the meaning of each data points on this plot. As indicated in the figure captions, different color points represent different gas types. Different points with same color represent different concentrations of the same gas type. For example, there are four different colors on this plot representing four different target gases. There are seven green points on this plot representing seven different CH_3OH concentrations of 7.2%, 3.6%, 2.0%, 1.0%, 0.55%, 0.28% and 0.14% (bottom up). As a result, the clustering of data points of the same color is desirable because it means that data points representing the same target gases tend to occupy specific areas on this PCA plot. These specific areas are usually called the "smell prints", just like the "fingerprints" that can be used to identify individual people. Although the separation of data points on Figure 4.5.14 (a) is clear at higher target concentrations, the lower concentration data points are very crowded, especially for CO and NO_2 at lower concentrations. This problem can be solved by adding another dimension to this 2D plot. Figure 4.5.14 (b) shows a clearer view by adding PC3 to build a 3D plot. The total variance explained in this 3D plot is increased
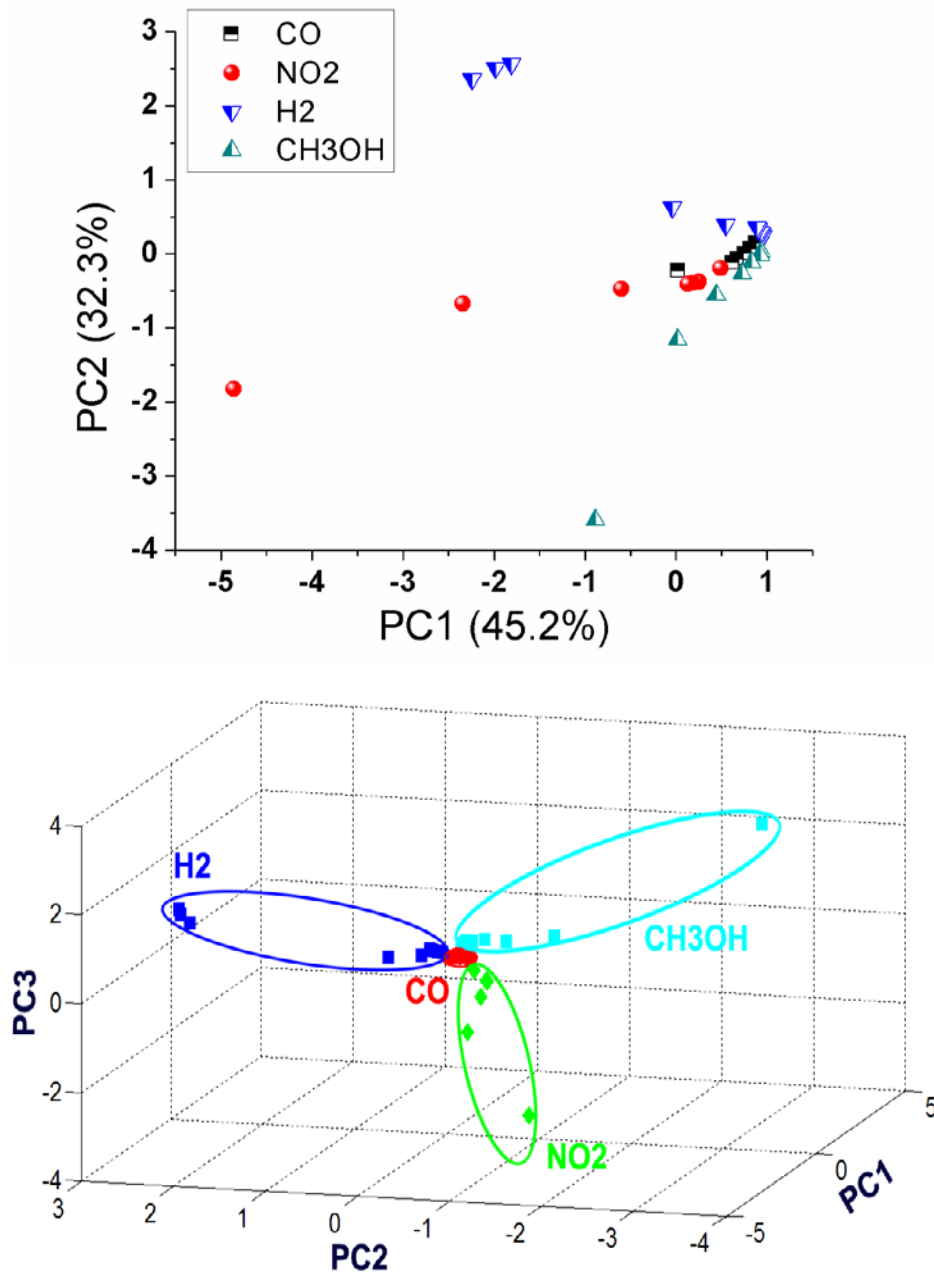
Figure 4.5.14 Data clustering plots via PCA for the four-nanowire sensor array. (a) 2D PCA plot formed using the first two PCs (PC1, PC2) shows clear clustering for data points from each of the four gas targets at high concentrations although data points at lower concentrations appear to be closely located. (b): 3D PCA map using the first three PCs (PC1, PC2, PC3) shows a 3D view of the data points for all four target gases at different concentrations.

to 98.3%, thus almost all of the information is demonstrated. In this plot, NO_2 and CO data points are clearly separated, and thus the smell prints of the four gases are distinguishable even at the lowest detected concentration (625 ppb f or NO_2). Overall, by pl otting all the relative sensitivities on a 3D PCA plot via PCA processing, we are able to successfully specify the individual smell prints for NO_2, CO, H_2, and CH_3OH down to a ppb concentration level based on the sensor array consisting of the ZnO, PPy, PANI, and Pd nanowires. This again demonstrates that: i) our sensor arrays using four different nanowire materials have the potential to discriminate all four target gases based on the different sensing patterns due to the differences in chemical properties; and ii) the smell prints for different sensing targets can be successful obtained, providing a basis for the actual gas identification.

4.5.7   Blind test and concentration estimation

Although the previous section demonstrated that smell prints for the target gases can be successfully built up, further research is necessary to investigate the reliability of this e-nose in actual gas identification and explore the possibility of target concentration estimation. A blind experiment is thus conducted where target gases are injected into the sensing chamber without previous knowledge of its composition or concentration. An estimation of the gas type and concentration is then made based on the real-time electrical signals from the nanowire array. Although this step is often overlooked by other research groups in their previous studies, it is crucial for the following reasons. (i) It eliminates the bias of the observer due to prior knowledge of the expected result, improving the credibility of the observed results. (ii) It mimics the real operation condition and verifies the performance of the device by repeating the experiment and reassuring its reliability. Figure 4.5.15 (a) presents a blind experiment sensing data that consists
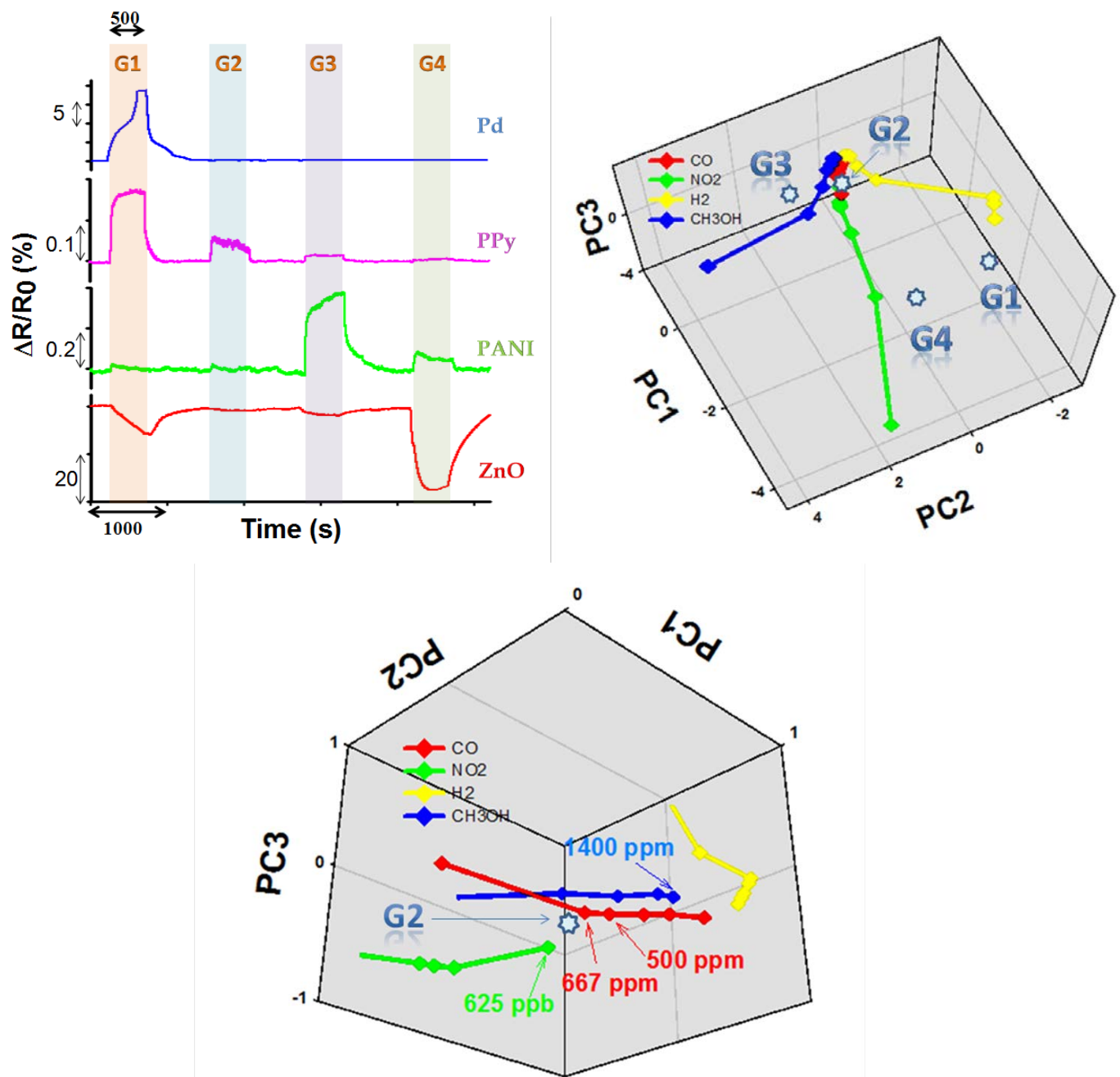
Figure 4.5.15 Blind test results for four gas injections. (a) The real time sensing responses from the nanowire array for four consecutive gas injections. (b) 3D PCA plot for estimation of the four gas injections. (c): zoomed-in3D PCA plot for a clearer view of Gas 2.

of real-time signals from four consecutive unknown gas injections. Each of the injected gas is one of the four target gases with arbitrary concentration. Pure nitrogen was used to purge the injected gas for 500 seconds before the injection of next gas. The saturated RS values from the four nanowires for each gas injection are processed by the PCA procedure mentioned above. After PCA, each gas injection corresponds to a new data point on the original PCA plot with smell prints, as shown in figure 4.5.15 (b). Although the data points for low concentration gases are crowded, they are clearly separated in a zoomed view as illustrated in figure 4.5.15 (c). Based on the relative position between the injection data point and the smell prints, the composition and concentration of each injected gas can be estimated. Gas 4, for example, has a corresponding data point closest to the point for 3.3 ppm NO_2, so the best estimate for gas 4 is NO_2 with a concentration of 3.3 ppm. Gas 2 position is closest to smell print point for 667 ppm CO (as shown in figure 4.5.15 (c), so the best estimation for gas 2 is 667 ppm CO. It is worth mentioning that the accuracy of the concentration estimation depends on the resolution of the concentration in the original smell prints. That is, by adding more calibration data points with intermediate concentrations into the smell prints, concentration estimation with better accuracy can be achieved. Similarly, the estimated compositions and concentrations for gases 1, and 3 are 7.2% H_2 and 3.6% CH_3OH, respectively. Table 3 compares the actual and estimated gas compositions and concentrations to verify the estimation accuracy.

Table 3 Comparisons between the actual and estimated gas compositions and concentrations

	Gas 1	Gas 2	Gas 3	Gas 4
Real composition (concentration)	H2 (2%)	CO (400 ppm)	CH3OH (5.4%)	NO2 (5 ppm)
Estimated composition (concentration)	H2 ($\approx$7.2%)	CO ($\approx$667 ppm)	CH3OH ($\approx$3.6%)	NO2 ($\approx$3.3 ppm)

As demonstrated, the compositions of all four injected gases are correctly estimated, demonstrating the identification ability of this nanowire array. The estimated concentrations are close to the actual values, although their accuracy can be further improved by increasing the number of calibration data points in the smell prints. Verified by the blind experiments, this e-nose not only successfully identified the four target gases but also provided rough estimations for the target concentrations.

4.6   CONCLUSIONS

We successfully fabricated a sensor array consisting of four different single nanowires, Pd, PPy, PANI, and ZnO, site-specifically using electrochemical deposition. The structure of these single nanowires was characterized using SEM, and the properties were confirmed using EDX and Raman spectroscopy. The 1 cm × 1 cm chip with the four-nanowire array on top was integrated into a sensing system, and four different target gases, including H_2, CH_3OH, CO, and NO_2, were selected for identification. With the help of PCA, the smell prints for all four target gases were successfully built up without overlap even at extremely low concentration levels (625 ppb). In addition, a blind experiment verified the identification ability of the nanowire array e-nose and provided rough estimations of target concentrations, although further development is needed to improve the accuracy. It is necessary to emphasize that we can potentially synthesize up to 16 different single nanowires site-specifically on the chip, significantly improving the target range and the identification ability of this e-nose device. To sum up, this work not only presented the fabrication of a single-nanowire array for a highly selective e-nose application, but it also

introduced a way for target concentration estimation through blind experiments, opening up the possibility of developing a widely applicable e-nose system that identifies both the composition and the concentration of the target gases.

5.0   SUMMARY AND ACHIEVEMENTS

5.1   ACHIEVEMENTS

In all, this work has presented the following achievements:

(1) Successful fabrication of Palladium (Pd), Polypyrrole (PPy), and Polyaniline (PANI) single nanowire with diameters less than 100 nm and lengths up to 7 μm across pre-patterned Au electrodes. The zinc oxide (ZnO) nanostructure has also been successfully fabricated via a 2-step processes with electrochemical deposition and hydrothermal process.

(2) A highly sensitive hydrogen gas sensor operating in room temperature based on a single Pd nanowire has been fabricated. The sensor has a lowest detection limit of 2-5 ppm and a response time of around 10s. A detailed study on Pd nanowire structure and its growth conditions demonstrates that Pd single nanowire structure can be controlled by selecting proper growth parameters. Moreover, hydrogen sensing mechanisms from Pd single nanowire have indicated a close relationships with the Pd nanowire structures.

(3) A new method involving gate electric field assisted electrodeposition has been discovered. Using this method, both Pd and PPy nanowire with sub-50 nm diameters can be successfully synthesized.

(4) A sensor array including Pd, PPy, PANI and ZnO single nanowires was fabricated on a same 1 cm × 1cm chip. Using this sensor array, hydrogen, methanol, carbon monoxide and nitrogen dioxide gases can be detected. Hydrogen can be detected at concentrations ranging from 10% to 94 ppm, methanol can be detected at concentrations from 7.2% to 0.14%, carbon monoxide can be detected at concentrations from 2000 ppm to 182 ppm, and nitrogen dioxide can be detected at concentrations from 10 ppm to 625 ppb.

(5) With the help of Principal Component Analysis, smell prints for all four target gases can be created. A blind test further proves the effectiveness of the e-nose in identifying four unknown gas injections. More importantly, based on the relationship between the gas concentrations and sensor responses, a rough estimation of target gas concentrations can be made, although further research is required to improve the estimation accuracy.

5.2 LIST OF PUBLICATIONS

[1] - Yushi Hu, David Perello, Usman Mushtaq, and Minhee Yun, Single Palladium Nanowire Via Electrophoresis Deposition Used as Ultra Sensitive Hydrogen Sensor, IEEE Transactions on Nanotechnology, 7(6), 693-699, 2008

[2] - Yushi Hu, Albert C. To, and Minhee Yun, Controlled growth of single metallic and conducting polymer nanowires via gate-assisted electrochemical deposition, Nanotechnology, 20, 285605, 2009

[3] - Yushi Hu, Jiyong Huang, Innam Lee, Xiliang Luo, Xinyan Tracy Cui, and Minhee Yun, Single Metal and Conducting Polymer Nanowires Used as Chemical/Biomolecular Sensors, Proceedings of 10th IEEE International Conference on Nanotechnology Joint Symposium with Nano Korea 2010, pp 708-711, 2010

[4] - Yushi Hu, and Minhee Yun, A highly selective electronic nose based on a single-nanowire array for chemical identification, Nanotechnology, under revision;

[5] – Jiyong Huang, Xiliang Luo, Yushi Hu, Xinyan Tracy Cui, and Minhee Yun, Rapid Real-time Electrical Detection of Protein Using Single Conducting Polymer Nanowire-Based Microfluidic Aptasensor, Biosensors and Bioelectronics, under revision;

BIBLIOGRAPHY

[1]   Lu, W.; Lieber, C. M., *Nanoelectronics from the bottom up*. Nat. Mater. (**2007**) *6* (11), 841-850.

[2]   Rodrigues, V.; Fuhrer, T.; Ugarte, D., *Signature of Atomic Structure in the Quantum Conductance of Gold Nanowires*. Phys. Rev. Lett. (**2000**) *85* (19), 4124.

[3]   Sachdev, S.; Werner, P.; Troyer, M., *Universal Conductance of Nanowires near the Superconductor-Metal Quantum Transition*. Phys. Rev. Lett. (**2004**) *92* (23), 237003.

[4]   Yun, M.; Myung, N. V.; Vasquez, R. P.; Lee, C.; Menke, E.; Penner, R. M., *Electrochemically Grown Wires for Individually Addressable Sensor Arrays*. Nano Lett. (**2004**) *4* (3), 419-422.

[5]   Hu, Y.; Perello, D.; Mushtaq, U.; Yun, M., *A Single Palladium Nanowire Via Electrophoresis Deposition Used as a Ultrasensitive Hydrogen Sensor*. IEEE Trans. Nanotechnol. (**2008**) *7* (6), 693-699.

[6]   Aravamudhan, S.; Kumar, A.; Mohapatra, S.; Bhansali, S., *Sensitive estimation of total cholesterol in blood using Au nanowires based micro-fluidic platform*. Biosensors and Bioelectronics (**2007**) *22* (9-10), 2289-2294.

[7]   Bourg, M. E.; van der Veer, W. E.; Grüell, A. G.; Penner, R. M., *Electrodeposited Submicron Thermocouples with Microsecond Response Times*. Nano Lett. (**2007**) *7* (10), 3208-3213.

[8]   Hayashi, M.; Thomas, L.; Moriya, R.; Rettner, C.; Parkin, S. S. P., *Current-Controlled Magnetic Domain-Wall Nanowire Shift Register*. Science (**2008**) *320* (5873), 209-211.

[9]   Malhotra, B. D.; Chaubey, A.; Singh, S. P., *Prospects of conducting polymers in biosensors*. Anal. Chim. Acta (**2006**) *578* (1), 59-74.

[10]   Giuliano, K. A.; Taylor, D. L., *Fluorescent-protein biosensors: New tools for drug discovery*. Trends Biotechnol. (**1998**) *16* (3), 135-140.

[11]   Wanekaya, A. K.; Chen, W.; Myung, N. V.; Mulchandani, A., *Nanowire-Based Electrochemical Biosensors*. Electroanalysis (**2006**) *18* (6), 533-550.

[12]   Ko, S. H.; Park, I.; Pan, H.; Grigoropoulos, C. P.; Pisano, A. P.; Luscombe, C. K.; Fréchet, J. M. J., *Direct Nanoimprinting of Metal Nanoparticles for Nanoscale Electronics Fabrication*. Nano Lett. (**2007**) *7* (7), 1869-1877.

[13]   Dong, B.; Lu, N.; Zelsmann, M.; Kehagias, N.; Fuchs, H.; Sotomayor Torres, C. M.; Chi, L. F., *Fabrication of High-Density, Large-Area Conducting-Polymer Nanostructures*. Adv. Funct. Mater. (**2006**) *16* (15), 1937-1942.

[14]   Basnar, B.; Weizmann, Y.; Cheglakov, Z.; Willner, I., *Synthesis of Nanowires Using Dip-Pen Nanolithography and Biocatalytic Inks*. Adv. Mater. (**2006**) *18* (6), 713-718.

[15]   Noy, A.; Miller, A. E.; Klare, J. E.; Weeks, B. L.; Woods, B. W.; DeYoreo, J. J., *Fabrication of Luminescent Nanostructures and Polymer Nanowires Using Dip-Pen Nanolithography*. Nano Lett. (**2001**) *2* (2), 109-112.

[16]   Vazquez-Mena, O.; Villanueva, G.; Savu, V.; Sidler, K.; van den Boogaart, M. A. F.; Brugger, J., *Metallic Nanowires by Full Wafer Stencil Lithography*. Nano Lett. (**2008**) *8* (11), 3675-3682.

[17]   Nielsch, K.; Müller, F.; Li, A. P.; Gösele, U., *Uniform Nickel Deposition into Ordered Alumina Pores by Pulsed Electrodeposition*. Adv. Mater. (**2000**) *12* (8), 582-586.

[18]   Mallet, J.; Molinari, M.; Martineau, F.; Delavoie, F.; Fricoteaux, P.; Troyon, M., *Growth of Silicon Nanowires of Controlled Diameters by Electrodeposition in Ionic Liquid at Room Temperature*. Nano Lett. (**2008**) *8* (10), 3468-3474.

[19]   Weintraub, B.; Deng, Y.; Wang, Z. L., *Position-Controlled Seedless Growth of ZnO Nanorod Arrays on a Polymer Substrate via Wet Chemical Synthesis*. The Journal of Physical Chemistry C (**2007**) *111* (28), 10162-10165.

[20]   Walter, E. C.; Murray, B. J.; Favier, F.; Kaltenpoth, G.; Grunze, M.; Penner, R. M., *Noble and Coinage Metal Nanowires by Electrochemical Step Edge Decoration*. J. Phys. Chem. B (**2002**) *106* (44), 11407-11411.

[21]   Yoo, W. C.; Lee, J. K., *Field-Dependent Growth Patterns of Metals Electroplated in Nanoporous Alumina Membranes*. Adv. Mater. (**2004**) *16* (13), 1097-1101.

[22]   Shi, Z.; et al., *Self-assembled palladium nanowires by electroless deposition*. Nanotechnology (**2006**) *17* (9), 2161.

[23]   Favier, F.; Walter, E. C.; Zach, M. P.; Benter, T.; Penner, R. M., *Hydrogen Sensors and Switches from Electrodeposited Palladium Mesowire Arrays*. Science (**2001**) *293* (5538), 2227-2231.

[24]   Kim, K. T.; Sim, J.; Cho, S. M., *Hydrogen gas sensor using Pd nanowires electro-deposited into anodized alumina template*. Sensors Journal, IEEE (**2006**) *6* (3), 509-513.

[25] Kolmakov, A.; Zhang, Y.; Cheng, G.; Moskovits, M., *Detection of CO and O2 Using Tin Oxide Nanowire Sensors*. Adv. Mater. (**2003**) *15* (12), 997-1000.

[26] Hangarter, C. M.; Bangar, M.; Mulchandani, A.; Myung, N. V., *Conducting polymer nanowires for chemiresistive and FET-based bio/chemical sensors*. J. Mater. Chem. (**2010**) *20* (16), 3131-3140.

[27] Mandelis, A.; Garcia, J. A., *Pd/PVDF thin film hydrogen sensor based on laser-amplitude-modulated optical-transmittance: dependence on H2 concentration and device physics*. Sens. Actuators, B (**1998**) *49* (3), 258-267.

[28] Flanagan, T. B.; Oates, W. A., *The Palladium-Hydrogen System*. Annual Review of Materials Science (**1991**) *21* (1), 269-304.

[29] Eichenauer, W., *F. A. Lewis: The Palladium Hydrogen System. Academic Press, London and New York 1967. 178 Seiten, 87 Abbildungen. Preis: 45 s*. Berichte der Bunsengesellschaft für physikalische Chemie (**1967**) *71* (9-10), 1160-1161.

[30] Barton, J. C.; Lewis, F. A.; Woodward, M. I., *Hysteresis of the Relationships between Electrical Resistance and the Hydrogen Content of Palladium*. Trans. Faraday Soc. (**1963**) *59*, 1201.

[31] Borchert, H.; Jürgens, B.; Nowitzki, T.; Behrend, P.; Borchert, Y.; Zielasek, V.; Giorgio, S.; Henry, C. R.; Bäumer, M., *Decomposition of methanol by Pd, Co, and bimetallic Co-Pd catalysts: A combined study of well-defined systems under ambient and UHV conditions*. J. Catal. (**2008**) *256* (1), 24-36.

[32] Landry, S. M.; Dalla Betta, R. A.; Lu, J. P.; Boudart, M., *Catalytic oxidation of carbon monoxide on palladium. 1. Effect of pressure*. The Journal of Physical Chemistry (**1990**) *94* (3), 1203-1206.

[33] Ateh, D. D.; Navsaria, H. A.; Vadgama, P., *Polypyrrole-based conducting polymers and interactions with biological tissues*. Journal of The Royal Society Interface (**2006**) *3* (11), 741-752.

[34] Hussain, A.; Kumar, A., *Electrochemical synthesis and characterization of chloride doped polyaniline*. Bull. Mater. Sci. (**2003**) *26* (3), 329-334.

[35] Feast, W. J.; Tsibouklis, J.; Pouwer, K. L.; Groenendaal, L.; Meijer, E. W., *Synthesis, processing and material properties of conjugated polymers*. Polymer (**1996**) *37* (22), 5017-5047.

[36] Maksymiuk, K., *Chemical reactivity of polypyrrole and its relevance to polypyrrole based electrochemical sensors*. Electroanalysis (N. Y.) (**2006**) *18* (16), 1537-1551.

[37] Zhang, B. P.; Binh, N. T.; Segawa, Y.; Wakatsuki, K.; Usami, N., *Optical properties of ZnO rods formed by metalorganic chemical vapor deposition*. Appl. Phys. Lett. (**2003**) *83* (8), 1635.

[38] Wu, J.-J.; Liu, S.-C., *ChemInform Abstract: Low-Temperature Growth of Well-Aligned ZnO Nanorods by Chemical Vapor Deposition*. ChemInform (**2002**) *33* (15), no-no.

[39] Vayssieres, L., *Growth of Arrayed Nanorods and Nanowires of ZnO from Aqueous Solutions*. Adv. Mater. (**2003**) *15* (5), 464-466.

[40] Zheng, M. J.; Zhang, L. D.; Li, G. H.; Shen, W. Z., *Fabrication and optical properties of large-scale uniform zinc oxide nanowire arrays by one-step electrochemical deposition technique*. Chem. Phys. Lett. (**2002**) *363* (1-2), 123-128.

[41] Liu, B.; Zeng, H. C., *Hydrothermal Synthesis of ZnO Nanorods in the Diameter Regime of 50 nm*. J. Am. Chem. Soc. (**2003**) *125* (15), 4430-4431.

[42] Qin, Y.; Yang, R.; Wang, Z. L., *Growth of Horizonatal ZnO Nanowire Arrays on Any Substrate*. The Journal of Physical Chemistry C (**2008**) *112* (48), 18734-18736.

[43] Xu, S.; Ding, Y.; Wei, Y.; Fang, H.; Shen, Y.; Sood, A. K.; Polla, D. L.; Wang, Z. L., *Patterned Growth of Horizontal ZnO Nanowire Arrays*. J. Am. Chem. Soc. (**2009**) *131* (19), 6670-6671.

[44] Wang, J. X.; et al., *Hydrothermally grown oriented ZnO nanorod arrays for gas sensing applications*. Nanotechnology (**2006**) *17* (19), 4995.

[45] Gardner, J. W.; Bartlett, P. N., *A brief history of electronic noses*. Sens. Actuators, B (**1994**) *18* (1-3), 210-211.

[46] Hu, Y.; To, A. C.; Yun, M., *The controlled growth of single metallic and conducting polymer nanowires via gate-assisted electrochemical deposition* Nanotechnology (**2009**) *20* (28), 285605.

[47] Im, Y.; Lee, C.; Vasquez, R. P.; Bangar, M. A.; Myung, N. V.; Menke, E. J.; Penner, R. M.; Yun, M., *Investigation of a Single Pd Nanowire for Use as a Hydrogen Sensor*. Small (**2006**) *2* (3), 356-358.

[48] Walter, E. C.; Zach, M. P.; Favier, F.; Murray, B. J.; Inazu, K.; Hemminger, J. C.; Penner, R. M., *Metal Nanowire Arrays by Electrodeposition*. ChemPhysChem (**2003**) *4* (2), 131-138.

[49] Witten, T. A.; Sander, L. M., *Diffusion-limited aggregation*. Physical Review B (**1983**) *27* (9), 5686.

[50] Yang, F.; Taggart, D. K.; Penner, R. M., *Fast, Sensitive Hydrogen Gas Detection Using Single Palladium Nanowires That Resist Fracture*. Nano Lett. (**2009**) *9* (5), 2177-2182.

[51] Peng, G.; Tisch, U.; Adams, O.; Hakim, M.; Shehada, N.; Broza, Y. Y.; Billan, S.; Abdah-Bortnyak, R.; Kuten, A.; Haick, H., *Diagnosing lung cancer in exhaled breath using gold nanoparticles*. Nat Nano (**2009**) *4* (10), 669-673.

[52] Ampuero, S.; Bosset, J. O., *The electronic nose applied to dairy products: a review*. Sens. Actuators, B (**2003**) *94* (1), 1-12.

[53] Li, M.; Myers, E. B.; Tang, H. X.; Aldridge, S. J.; McCaig, H. C.; Whiting, J. J.; Simonson, R. J.; Lewis, N. S.; Roukes, M. L., *Nanoelectromechanical Resonator Arrays for Ultrafast, Gas-Phase Chromatographic Chemical Analysis*. Nano Lett. (**2010**) *10* (10), 3899-3903.

[54] Ryan, M. A.; Homer, M. L.; Zhou, H. M.; Manfreda, K.; A.; Kisor, A.; Shevade, A.; Yen, S. P. S., *Expanding the analyte set of the JPL electronic nose to include inorganic species*. J. Aerosp. SAE Trans. (**2005**) (2005-01-2880), 225.

[55] Chen, P.-C.; Ishikawa, F. N.; Chang, H.-K.; Ryu, K.; Zhou, C., *A nanoelectronic nose: a hybrid nanowire/carbon nanotube sensor array with integrated micromachined hotplates for sensitive gas discrimination*. Nanotechnology (**2009**) *20* (12), 125503.

[56] Sysoev, V. V.; Goschnick, J.; Schneider, T.; Strelcov, E.; Kolmakov, A., *A Gradient Microarray Electronic Nose Based on Percolating SnO2 Nanowire Sensing Elements*. Nano Lett. (**2007**) *7* (10), 3182-3188.

[57] Peng, G.; Hakim, M.; Broza, Y. Y.; Billan, S.; Abdah-Bortnyak, R.; Kuten, A.; Tisch, U.; Haick, H., *Detection of lung, breast, colorectal, and prostate cancers from exhaled breath using a single array of nanosensors*. Br. J. Cancer (**2010**) *103* (4), 542-551.

[58] Freund, M. S.; Lewis, N. S., *A chemically diverse conducting polymer-based "electronic nose"*. Proc. Natl. Acad. Sci. U. S. A. (**1995**) *92* (7), 2652-2656.

[59] Chen, Y.; Luo, Y., *Precisely Defined Heterogeneous Conducting Polymer Nanowire Arrays – Fabrication and Chemical Sensing Applications*. Adv. Mater. (**2009**) *21* (20), 2040-2044.

[60] Paul, S.; Joseph, M., *Polypyrrole functionalized with FePcTSA for NO2 sensor application*. Sens. Actuators, B (**2009**) *140* (2), 439-444.

[61] Wang, J. X.; Sun, X. W.; Yang, Y.; Wu, C. M. L., *N–P transition sensing behaviors of ZnO nanotubes exposed to NO 2 gas*. Nanotechnology (**2009**) *20* (46), 465501.

[62] Prasad, A. K.; Kubinski, D. J.; Gouma, P. I., *Comparison of sol-gel and ion beam deposited MoO3 thin film gas sensors for selective ammonia detection*. Sens. Actuators, B (**2003**) *93* (1-3), 25-30.